Landau-Zener Transitions and a Feshbach Resonance in Spinor Bose Einstein Condensates

Michael Lurie Goldman

Advisor: Professor David Hall
May 8, 2008

Submitted to the
Department of Physics of Amherst College
in partial fulfilment of the
requirements for the degree of
Bachelors of Arts with honors

Abstract

The recent construction of a cross-beam optical dipole trap has opened to our laboratory the possibility of conducting experiments involving Bose-Einstein condensates of ^{87}Rb atoms in any of the quantum states of the ground state $F = 1$ hyperfine manifold. At Amherst, the final phase of Bose-Einstein condensation is conducted in magnetic confinement, resulting in BECs composed entirely of atoms in a magnetically trappable state. Using a Landau-Zener transition, atoms can be transferred from this one state into any of three states in the $F = 1$ hyperfine manifold.

Through a detailed characterization of the Landau-Zener process, we can choose to create a BEC in a balanced superposition of all three states or to transfer the entire population of atoms from the magnetically trappable state to a magnetically untrappable one. Exercising the first option results in the formation of a spinor condensate, a multiple-component condensate with the orientation of the atomic spins as a degree of freedom. This has allowed us to observe a spinor atom laser. We have also studied the spatial separation of the condensates with the goal of diagnosing the presence of stray magnetic field gradients that may adversely affect the performance of our apparatus.

Exercising the second option enables us to explore various Feshbach resonances, none of which are accessible from the magnetically trapped state. We have extensively explored an interspecies Feshbach resonance at 9.1 G between the $|1, +1\rangle$ and $|2, -1\rangle$ states. We have measured condensate loss rates due to the Feshbach resonance and observed how the dynamical evolution of the binary system depends on variations in the interspecies scattering length. We expect that these experiments constitute the first step in a continuing investigation into Feshbach resonance, and so we discuss what future directions these preliminary findings suggest.

Acknowledgments

First, I would like to thank Professor Hall for his seemingly endless patience, devotion to teaching, and inspiration. I am at Amherst today in large part because of a tour of this lab that I took as a prospective student. That a professor would take the time to show one anonymous high school student how to perform his experiment seemed to me then to indicate that this place was special, and seems to me now to embody what has been the finest part of receiving an Amherst education.

My lab partner and co-thesis writer, Elizabeth Petrik, has been no less influential throughout my four years as a physics major. From the first labs of Physics 23 to the last frenzied nights of thesis writing, she has shown incredible patience and a deep love of her work. Her diligent efforts in the lab and instruction in the ways of the machine have made this thesis possible, but her friendship, both in and out of the lab, have made the more profound impact.

I am also grateful to Daniel Guest ’07E, Jason Merrill ’06, and all of the other former Hall students in whose footsteps Elizabeth and I humbly follow. It is a tribute to their efforts that I can now take for granted many of the tasks on which they spent untold hours.

I would like to thank PostDoc Kevin Mertes, for helping me grow my fledgling knowledge of programming, Dan Krause, for sharing his love of machining, and Bob Cann, for manufacturing creative fixes for the lab.

I am grateful to the third floor of King for providing companionship when I needed to work and endless diversions when I needed not to. I am especially in the debt of Katherine Chen, who has been an everlasting source of friendship, support, and occasional craziness.

I could not possibly list all the ways in which Shandra has been wonderful throughout this process, even from an ocean away.

Of course, I owe the greatest debt of all to my parents, John and Elizabeth Goldman, for their unconditional love and unfailing support in all my endeavors.

Contents

List of Figures

Chapter 1

Introduction

The field of Bose-Einstein condensation in dilute gases has been extremely active since its experimental inception in 1995. It has received such intense attention in large part because Bose-Einstein condensates exhibit quantum phenomena on a relatively macroscopic scale. In this state of matter, a collection of bosonic particles can condense into a common ground state and become a cohesive quantum-mechanical entity. Millions of atoms can be described collectively by the same condensate wave function. This has led to observations of a wide range of quantum phenomena, including vortices [1], tunneling [2], and interference between massive particles [3].

Over the course of 2006, the construction of a crossed-beam optical dipole trap opened to this lab a new realm of experimentation within this growing field. Whereas before, we were limited to holding atoms in only three magnetic sublevels in the magnetic trap, we can now hold all eight magnetic sublevels of the ground state in the optical trap. In his thesis [4], Daniel Guest conducted preliminary experiments on several topics that the optical trap has made available. In this thesis, we expand upon his efforts in two particular areas: spinor condensates and a Feshbach resonance.

We extensively study and refine the Landau-Zener process, by which we can precisely populate all three magnetic sublevels of the $F = 1$ hyperfine manifold. We find in Section 2.2.1 that sweeping the magnetic field reliably transfers the entire condensate to the $|1, +1\rangle$ state in the slow-sweep limit but is unreliable at intermediate sweep rates and cannot produce a precise population distribution among the three sublevels. Sweeping the RF radiation frequency, in contrast, produces precise and reproducible population distributions using any sweep rate that is allowed by our technical limitations, as described in Section 2.2.2.

We implement the frequency sweep method and use it to create spinor condensates, which have the atomic spin as a degree of freedom. This new degree of freedom has enabled us to conduct a wide range of experiments. We describe a spinor atom laser in Section 2.5 and we believe that we are the first group to observe vortices in a spinor condensate [5]. Spinor condensates also allow us to make a preliminary diagnosis in Section 2.4 of stray magnetic field gradients in the apparatus. We allow these stray gradients to exert a Stern-Gerlach forces on the spinor condensate, which affect each component differently and lead to asymmetric spatial separation. Understanding and correcting for these stray gradients will be crucial for the future observation of topological structures in spinor condensates.

We can also use the field sweep method along with a two-photon pulse to populate the $|1,+1\rangle$ and $|2,-1\rangle$ sublevels equally. In a magnetic field of 9.1 G, a binary condensate composed of atoms in these two states experiences an interspecies Feshbach resonance. This phenomenon occurs when the energy of two unbound atoms becomes degenerate with the energy of a molecular state. The two-atom system then tunnels between the unbound continuum state and the quasi-bound molecular state.

While the atoms are in the quasi-bound state, they can either be lost two- or three-body loss mechanisms, as described in Section 3.2.2. In Section 3.5, we make a careful measurement of these Feshbach losses in order to characterize the resonance. A Feshbach resonance also produces a dramatic change in the scattering length, the parameter that characterizes the interatomic interaction strength within the condensate. As a result, we can tune the binary condensate from being miscible to immiscible simply by varying the magnetic field around the Feshbach resonance. In Section 3.6, we take advantage of this capability to observe how the non-equilibrium dynamics of an evolving binary condensate depend on the scattering length. In order to fully discuss these current investigations, we must first lay out a brief history and theory of Bose-Einstein condensates and explain how they are produced here at Amherst.

1.1 History

The first contribution to the theory of Bose-Einstein condensation was made in 1924 by Satyendra Nath Bose. In that year, he published a short paper reconciling a logical flaw in the history of quantum physics, the fact that Planck's formula for black body radiation, the "starting point of the quantum theory," had not yet been derived without recourse to classical electrodynamics [6]. Bose successfully accomplished this through the application of statistical analysis to electromagnetic radiation. This approach was revolutionary, so much so that the paper was initially declined for publication, in that it demanded that all photons of the same energy be indistinguishable.

Bose sent a copy of the paper to Albert Einstein, who agreed with the analysis and arranged to have the paper published before extending the theory with three papers of his own [7]. In these papers, he extended this statistical analysis, which Bose had applied to massless photons, to describe massive particles in gaseous form. These particles, which have an integer spin, are known as bosons. At very low energies, they can be analyzed using the method Einstein developed in these papers, known as Bose-Einstein statistics, which allows for multiple indistinguishable particles occupying the same quantum state. This also implies that a bosonic gas can "condense" into the lowest-energy quantum state when cooled below a critical temperature. In contrast, particles with a half-integer spin are known as fermions, in honor of Enrico Fermi. These particles can be analyzed using a method developed by Fermi and Paul Dirac during this same time period, known as Fermi-Dirac statistics, which stipulates that each particle must occupy a distinct quantum state.

Though superconductors, which can be described as Bose-Einstein condensates of Cooper pairs [8], were discovered in 1911 and superfluidity in ^{4}He, which is analogous to Bose-Einstein condensation [9], was discovered in 1937, Bose-Einstein condensation in a dilute gas, as was Einstein's original concept, was not demonstrated until much later. Following the development of optical cooling in 1985 [10], magneto-optical trapping in 1987 [11], and evaporative cooling from a magnetic trap in 1994 [12], three independent groups were able to achieve Bose-Einstein condensation in 1995. On the morning of July 5, a group at the Joint Institute for Laboratory Astrophysics led by Carl Wieman and Eric Cornell first achieved Bose-Einstein condensation in a dilute gas by cooling a cloud of ^{87}Rb atoms to 170 nK at a density of 10^{12} cm^{-3} [13]. Following closely in July, a group at Rice University led by Randall Hulet obtained evidence of condensation in spin-polarized ^{7}Li [14]. Finally, a group at the Massachusetts Institute of Technology led Wolfgang Ketterle was able to condense 5×10^5 ^{23}Na atoms by cooling them to approximately 120nK at densities greater than 10^{14} cm^{-3} [15]. These groundbreaking and nearly contemporaneous achievements marked the birth of an extremely active branch of atomic physics and earned Wieman, Cornell, and Ketterle the 2001 Nobel Prize in Physics.

1.2 Theory

1.2.1 A Statistical Interpretation

Bose-Einstein condensation is the consolidation of a population of particles into a single quantum state, a phenomenon predicted by Bose-Einstein quantum-statistical mechanics. The applicability of this analysis is based on the indistinguishability of particles. It can be demonstrated easily that multiple bosons can exist in the same quantum state and multiple fermions cannot, imposing the condition that particles be bosonic in order to be Bose-Einstein condensed.

Consider a system composed of two particles and described by the wave function $\Psi(\mathbf{r}_1, \mathbf{r}_2)$. The exchange operator $\hat{P}_{12}$ acting on the wave function has the effect of switching the particles and has an eigenvalue c:

$$\hat{P}_{12}\Psi(\mathbf{r}_1, \mathbf{r}_2) = \Psi(\mathbf{r}_2, \mathbf{r}_1) = c\Psi(\mathbf{r}_1, \mathbf{r}_2). \tag{1.1}$$

Applying the exchange operator twice results in the system returning to its original state, and so

$$\hat{P}_{12}^2\Psi(\mathbf{r}_1, \mathbf{r}_2) = \Psi(\mathbf{r}_1, \mathbf{r}_2) = c^2\Psi(\mathbf{r}_1, \mathbf{r}_2). \tag{1.2}$$

From Eq. 1.2, it follows that $c^2 = 1$, $c = \pm 1$, and

$$\hat{P}_{12}\Psi(\mathbf{r}_1, \mathbf{r}_2) = \pm\Psi(\mathbf{r}_1, \mathbf{r}_2). \tag{1.3}$$

By definition, bosons are particles for which the wave function remains constant under the exchange operator and fermions are particles for which the wave function undergoes a sign change.

This condition allows us to construct a wave function for two indistinguishable particles at positions $\mathbf{r}_1$ and $\mathbf{r}_2$ and in internal states a and b:

$$\Psi_\pm(\mathbf{r}_1, \mathbf{r}_2) = A\left[\Psi_a(\mathbf{r}_1)\Psi_b(\mathbf{r}_2) \pm \Psi_b(\mathbf{r}_1)\Psi_a(\mathbf{r}_2)\right], \tag{1.4}$$

where Ψ_+ describes bosons, Ψ_- describes fermions, and A is a normalization constant. If the two particles are both in the same internal state a, then the composite wave function for bosons is simply

$$\Psi_+(\mathbf{r}_1, \mathbf{r}_2) = 2A\Psi_a(\mathbf{r}_1)\Psi_a(\mathbf{r}_2) \tag{1.5}$$

and the composite wave function for fermions must be zero. This result, that no two fermions can occupy the same quantum state, is known as the Pauli Exclusion Principle and forms the basis of the difference between the Bose-Einstein and Fermi-Dirac systems of quantum-statistical mechanics.

The number of bosons expected to occupy a specific state is given by the Bose-Einstein distribution:

$$f_{\mathrm{BE}}(\epsilon_i) = \frac{1}{\mathrm{e}^{(\epsilon_i-\mu)/k_B T} - 1}, \tag{1.6}$$

where ϵ_i is the energy of the ith state, μ is the chemical potential, k_B is the Boltzmann constant, and T is the temperature [16]. The analogous expression for fermions is the Fermi-Dirac distribution

$$f_{\mathrm{FD}}(\epsilon_i) = \frac{1}{\mathrm{e}^{(\epsilon_i - \mu)/k_B T} + 1}, \tag{1.7}$$

which, as can be deduced from the Pauli Exclusion Principle, has an upper bound of 1. Because the Bose-Einstein distribution goes to infinity at $\epsilon_i = \mu$, we can infer that, although only one fermion can occupy any state, an unlimited number bosons can occupy the ground state, a phenomenon known as Bose-Einstein condensation.

1.2.2 A Quantum Mechanical Interpretation

We can also understand the phenomenon of Bose-Einstein condensation in a dilute gas in terms of quantum mechanical overlap of the particles. We will use the particles' deBroglie wavelengths as a measure of the spatial extent of their wave functions. At high temperatures, the deBroglie wavelengths of the particles are small and the dilute gas behaves classically. As the system's energy is reduced, the particles move more slowly and their wavelengths expand. At a critical temperature, the wavelengths of the particles overlap to an extensive degree and Bose-Einstein condensation becomes energetically favorable [16]. Here, we will provide a brief description of this interpretation similar to the one given by Daniel Guest [4]. For a more detailed derivation, we would recommend the work of Benjamin Samelson-Jones [17] or Elizabeth

Petrik [5].

The thermal deBroglie wavelength of a particle is given by

$$\lambda_{\mathrm{T}} = \frac{h}{\sqrt{2\pi m k_B T}}, \tag{1.8}$$

where h is Planck's constant, m is the mass of the particle, k_B is Boltzmann's constant, and T is the temperature of the system. As the system is cooled, the particles slow and the quantum mechanical volume that each particle occupies increases as λ_{T}^3. We can define the phase space density D as a measure of the overlap of the wave functions of adjacent particles:

$$D = n\lambda_{\mathrm{T}}^3, \tag{1.9}$$

where n is the number density of the particles.

As D approaches 1, the wave functions begin to overlap and at $D = 2.612$, Bose-Einstein condensation becomes energetically favorable [16, 17]. These overlapping wave functions are phase-coherent over the extent of the condensate [3], so the entire multi-particle condensate can be described by a single order parameter, or macroscopic wave function. As we will discuss in Section 3.1.2, this coherence allows the state of the condensate to be described by the Gross-Pitaevskii equation, an analog to the Schrödinger equation for a multi-particle system in which the interparticle interactions can be integrated out.

1.3 Properties of ^{87}Rb

To be Bose-Einstein condensed, a particle must either be a boson, having an integer intrinsic spin, or a composite boson, comprising an even number of fermions of half-integer spin. Examples include the elementary bosons - photons, gluons, gravitons, and the $W^{\pm}$ and Z^{0} bosons, to name some [18] - and composite bosons such as certain atoms and Cooper pairs. Superconductivity can be considered a Bose-Einstein condensation of these Cooper pairs, which are pairs of electrons that act like bosons [8]. In our experiment, we condense ^{87}Rb atoms, which have 37 protons, 37 electrons and 50 neutrons. Although the only stable isotope of rubidium is ^{85}Rb, ^{87}Rb can be considered effectively stable since it decays to ^{87}Sr via β^{-} decay with a half-life of $4.97(3) \times 10^{10}$ years [19]. Within the nucleus, all of the neutrons and all but one of the protons are paired, which cancels their contributions to the nuclear spin. The unpaired proton occupies the $2p_{3/2}$ [20] nuclear orbital and thus the total nuclear spin for ^{87}Rb is $I = 3/2$.

Our selected atom, ^{87}Rb also has the advantage of being an alkali metal. The four inner electronic shells are completely filled in a krypton-like electronic configuration, and therefore are extremely stable and contribute no net angular momentum to the atom. The electronic behavior of the atom then is characterized entirely by the single valence electron, resulting in a ground state configuration and series of electronic transitions that are far simpler than those of atoms with more populated valence shells. With this simplicity also comes an increase in laser-cooling efficiency, which explains why by 1997, BECs had only been realized in dilute gases of rubidium, sodium, and lithium, all alkali metals [21].

Simplicity, however, is not a necessity. Since 1997, Bose-Einstein condensation has been observed in, among others, ^{133}Cs atoms [22] and diatomic molecules of ^{6}Li [23] and ^{40}K [24], both of which are fermionic as individual atoms. The last two achievements were accomplished by forming molecules from ultra-cold Fermi gases via Feshbach resonance.

1.3.1 Hyperfine Structure

In its ground state, the single valence electron of ^{87}Rb occupies the $5^2\mathrm{S}_{1/2}$ subshell. The degeneracy of the ground state is broken by two perturbations to the Hamiltonian. The first, hyperfine splitting, is a result of magnetic dipole-dipole coupling between the nucleus and the valence electron. The magnetic dipole created by the intrinsic spin and orbital angular momentum of the electron interacts with the magnetic field created by the magnetic dipole of the nucleus and results in a splitting of energy levels according to the relative alignment of the two dipoles. These energy levels are characterized by the total atomic angular momentum $\mathbf{F} = \mathbf{I} + \mathbf{J}$, where $\mathbf{I}$ is the intrinsic spin of the nucleus and $\mathbf{J} = \mathbf{L} + \mathbf{S}$ is the total electron angular momentum. Because the ground state *s*-orbital is isotropic, the total angular momentum of the atom depends only on the intrinsic spins of the nucleus and the valence electron.

The hyperfine energy splitting of the ground state is given by

$$\Delta E_{\mathrm{HF}} = \frac{A_{\mathrm{HF}}}{2}\Big(F(F+1) - I(I+1) - J(J+1)\Big), \tag{1.10}$$

where A is a constant that has been experimentally determined to be 3.417 GHz [25]. Substituting in $I = 3/2$ and $J = 1/2$, we find

$$\Delta E_{\mathrm{HF}} = A_{\mathrm{HF}}(-1/4 \pm 1), \tag{1.11}$$

for $F = 3/2 \pm 1/2$. This results in the ground state of ^{87}Rb being, to first approximation, a two-level system with the higher-energy $F = 2$ hyperfine manifold separated from the $F = 1$ hyperfine manifold by 6.835 GHz. Since the ground state can, to the first order, be treated as a two-level system, the top operator of all subsequent $\pm$ or $\mp$ dual operators in this chapter will describe the $F = 2$ hyperfine manifold and the bottom will describe the $F = 1$ hyperfine manifold.

Here, a quick note must be made on the conventions for units of energy that are used throughout this thesis. Differences in energy between hyperfine manifolds or Zeeman levels (discussed below) are expressed by the frequency of the resonant radiation for that transition ($\nu = E/h$). Under this convention, hyperfine splitting corresponds to microwave radiation and Zeeman splitting corresponds to radio frequency radiation. Differences in energy between fine structure sublevels, for which the resonant radiation is in the visible portion of the spectrum, are given by the *in vacuo* wavelength of the radiation ($\lambda = hc/E$). Trapping potentials, such as that of the optical trap, are given in microkelvins ($T = E/k_B$).

1.3.2 Zeeman Structure

The second perturbation, Zeeman splitting, is a result of the interaction of the atomic angular momentum with an external magnetic field. The atom has an magnetic moment associated with its total angular momentum, so there is an energy splitting associated with the alignment of this magnetic moment with the external field. The different Zeeman energy levels are characterized by the quantum number m_F, which gives the projection of the atomic angular momentum along the z-axis in units of $\hbar$. Since m_F ranges from $-F$ to $+F$ in integer steps, the $F = 1$ hyperfine manifold is split into three energetically distinct states at non-zero field and the $F = 2$ hyperfine manifold is split into five.

If the Zeeman splitting is small in comparison to the fine-structure splitting, then the Hamiltonian describing the Zeeman energy shift is

$$H_B = \frac{\mu_B}{\hbar}(g_J J_z - g_I I_z)B_z, \tag{1.12}$$

where μ_B is the Bohr magneton, J_z and I_z are the z-components of the nuclear and electron angular momenta, and g_J and g_I are the g-factors associated with those angular momenta. Although solving for the energy shift in the general case must be done numerically, there are two pertinent special cases that can be solved analytically.

First, in the weak field limit, the Zeeman energy shift is linear with respect to the field strength and is given by

$$\Delta E_{\text{Zeeman}} = m_F g_F \mu_B B, \tag{1.13}$$

where g_F is the Landé g-factor. The Landé g-factor for atomic angular momentum is defined as

$$g_F = \frac{F(F+1) - I(I+1) + J(J+1)}{2F(F+1)} g_J - \frac{F(F+1) + I(I+1) - J(J+1)}{2F(F+1)} g_I, \tag{1.14}$$

which reduces to

$$g_F = -g_I \pm \frac{1}{4}(g_J + g_I) \tag{1.15}$$

for the ground state of ^{87}Rb. Conveniently, for the experimentally determined values of g_J and g_I [25], we find $g_F = \pm 1/2$ to better than 0.4%. This works out to a simple expression

$$\nu_{\text{Zeeman}} = \pm m_F \beta B, \tag{1.16}$$

where $\beta = 0.70$ MHz/G, for the Zeeman energy level shift of a given state. As we usually operate with fields smaller than 10 G, this first-order approximation is accurate to better than 0.4% and has the virtue of being far simpler than the precise expression.

For calculating transition frequencies, however, we would like a more precise expression for the Zeeman energy shift. Luckily, the second special case involves states for which $J = 1/2$. In the ground state, then, the Zeeman energy shift is given rigorously by the Breit-Rabi equation,

$$E_{\text{BR}} = \frac{\Delta E_{\text{HF}}}{2(2I+1)} - g_I \mu_B m_F B + (-1)^F \frac{\Delta E_{\text{HF}}}{2} \sqrt{1 + \frac{4}{2I+1} m_F \gamma B + (\gamma B)^2}, \tag{1.17}$$

with

$$\gamma = (g_J + g_I) \frac{\mu_B}{\Delta E_{\text{HF}}}. \tag{1.18}$$

Here, ΔE_{HF} is defined as the energy splitting between the two hyperfine manifolds, or $\Delta E_{\text{HF}}^{(+)} - \Delta E_{\text{HF}}^{(-)} = 2A_{\text{HF}}$ from Eq. 1.11. We can see that the Breit-Rabi equation takes into account both hyperfine and Zeeman splitting, providing a complete account of the energy perturbations of all quantum states within the ground state (or any fine structure sublevel with $J = 1/2$, for that matter).

To demonstrate that the Breit-Rabi equation accounts for both effects, we can observe it in the weak field approximation (i.e. $\gamma B \ll 1$). The Breit-Rabi equation, through some algebra and insertion of proper values, simplifies to

$$E_{\text{BR}} = A_{\text{HF}}(-{}^1\!/_4 \pm 1) + m_F \mu_B B\big(-g_I \pm {}^1\!/_4(g_J + g_I)\big), \tag{1.19}$$

which, considering Eqs. 1.11, 1.13, and 1.15, is precisely the sum of the hyperfine splitting and weak-field Zeeman splitting.

There is a third regime for which the magnitude of the Zeeman energy shift has been analytically solved. When the magnetic field is strong enough to disrupt the spin-orbit coupling that is responsible for the fine structure of the atom, Zeeman splitting is known as the Paschen-Back effect and its energy spacings are also linear in the magnetic field magnitude. Since our experiment does not approach this regime, however, it does not need to be discussed further here. Zeeman splitting across all three field regimes is shown in Fig. 1.1.

In summary, a complete diagram of the ground state structure is shown in Fig. 1.2(a). The ground state consists of two hyperfine manifolds with $F = 1$ and $F = 2$ that are separated by 6.835 GHz. Zeeman splitting divides the two hyperfine manifolds into $2F + 1$ non-degenerate quantum states at non-zero field and is given, to first order, by $\pm m_F \beta B$, with $\beta = 0.70$ MHz/G, for $F = 3/2 \pm 1/2$.

1.3.3 Fine Structure

Even though experimentation in Bose-Einstein condensation is, by definition, concerned primarily with the structure of the ground state, the structure of excited electronic states in ^{87}Rb must also be described. Fine structure arises from spin-orbit coupling, the interaction of the magnetic moment associated with the intrinsic spin of an electron with the magnetic field produced by the orbit of the nucleus, constructed in the reference frame of the electron.

^{87}Rb has a fine-structure doublet in the 5P sublevel, resulting in $5^2\mathrm{P}_{1/2}$

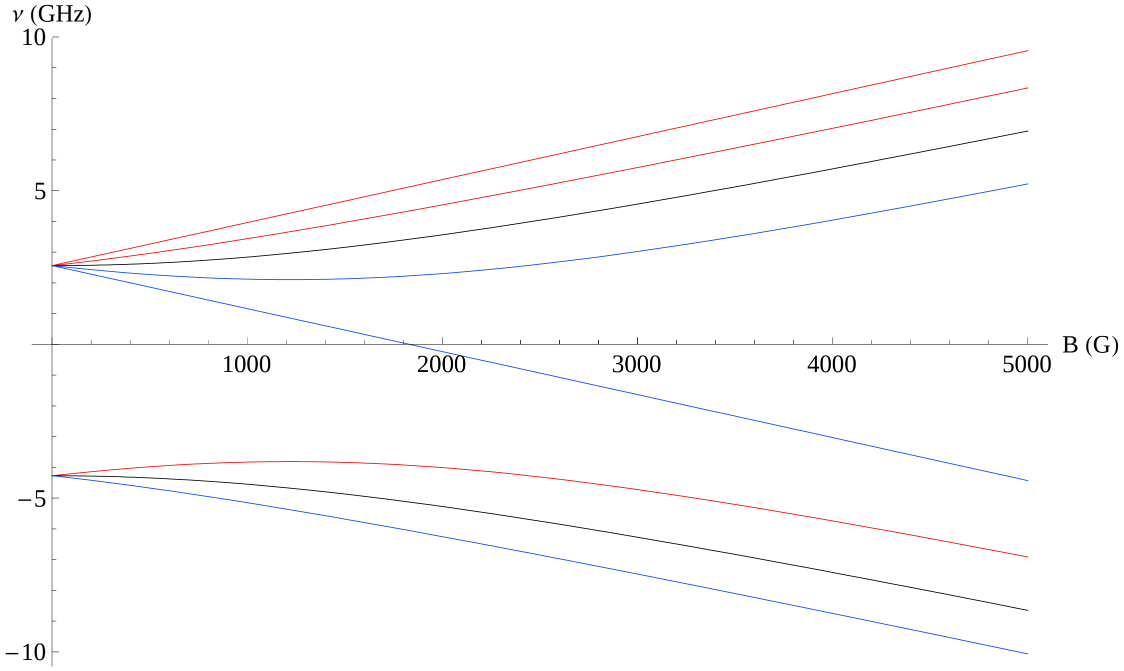

Figure 1.1: Plot of the Breit-Rabi equation over a wide range of magnetic field magnitudes. The hyperfine spacing and linear Zeeman splitting are evident at weak fields, the quadratic Zeeman effect is evident at intermediate fields, and the linear Paschen-Back regime is evident at strong fields. From the highest energy to the lowest, the states are $|2,+2\rangle$ through $|2,-2\rangle$ and $|1,-1\rangle$ through $|1,+1\rangle$.

and $5^2\mathrm{P}_{3/2}$ component sublevels. Essentially, the spin-1/2 system of the valence electron's intrinsic spin ($S = \pm 1/2$) is superimposed on its orbital angular momentum ($L = 1$) to form a two-level system with total electron angular momenta $J = 1/2$ and $J = 3/2$.

The $5^2\mathrm{P}_{1/2}$ sublevel, because it has the same total electron angular momentum as the ground state, exhibits similar hyperfine and Zeeman structures. The number and degeneracies of the hyperfine manifolds are the same but the magnitudes of the hyperfine and Zeeman splittings are reduced. The hyperfine spacing is reduced because the constant A_{HF} from Eqs. 1.10 and 1.11 has been found to be 408.3 MHz for this sublevel, roughly a factor of eight smaller than that of the ground state [25]. The Zeeman spacing is reduced because g_F is reduced to $\pm 1/6$. Just as g_F is composed of g_I and g_J, g_J is itself a Landé g-factor composed of the spin g-factor g_S and the orbital angular momentum g-factor g_L. The definition of g_J is exactly analogous to Eq. 1.14, so different values for I and L decrease the values of both g_J and g_F by a factor of three. Since, for the purposes of this experiment the $5^2\mathrm{P}_{1/2}$ sublevel is only important for optical trapping, which does not involve transitions to specific hyperfine or Zeeman levels but rather a sum over all possibly transitions, its internal structure need not be calculated in further detail.

The $5^2\mathrm{P}_{3/2}$ sublevel, however, has a qualitatively different hyperfine structure than the ground or $5^2\mathrm{P}_{1/2}$ states. Because $J = 3/2$, F ranges from 0 to 3 in integer steps and there are four hyperfine manifolds of degeneracy $2F + 1$.

To calculate the hyperfine splitting, a second, more complicated term must be added to Eq. 1.10. This term, which applies only to states for which $J \neq 1/2$, results in the four hyperfine manifolds being unevenly spaced, as shown in Fig. 1.2(b). As with the $5^2\mathrm{P}_{1/2}$ sublevel, the different values of I and J change the value of g_F and the magnitude of the Zeeman splitting. In the $5^2\mathrm{P}_{3/2}$ sublevel, g_F is equal to $+2/3$ for the three upper hyperfine manifolds but is undefined for the $F = 0$ hyperfine manifold, which does not exhibit Zeeman splitting. We are concerned with this sublevel primarily for three specific transitions from the ground state, shown in Fig. 1.2(b), that are important in the process of condensation.

Here, we establish a convention for referring to quantum states and transitions between them. In general, a specific quantum state will be denoted by $|F, m_F\rangle$. We will not be discussing specific transitions in the D_1 ($5^2\mathrm{S}_{1/2} \rightarrow 5^2\mathrm{P}_{1/2}$) line, so a primed state indicates a state in the excited $5^2\mathrm{P}_{3/2}$ level. Transitions that are part of the D_2 line will either be described using only the numbers of the hyperfine manifolds between which the transition occurs or the standard $|F, m_F\rangle$ notation. For example, the $5^2\mathrm{S}_{1/2}, F = 2 \rightarrow 5^2\mathrm{P}_{3/2}, F = 3$ "cycling" transition that is used in optical molasses will be denoted $2 \rightarrow 3'$, while a more specific instance of this transition which is important in magneto-optical trapping will be denoted $|2, 2\rangle \rightarrow |3, 3\rangle'$. All other transitions, which occur between states within the $5^2\mathrm{S}_{1/2}$ ground state, will be described using the standard $|F, m_F\rangle$ notation.

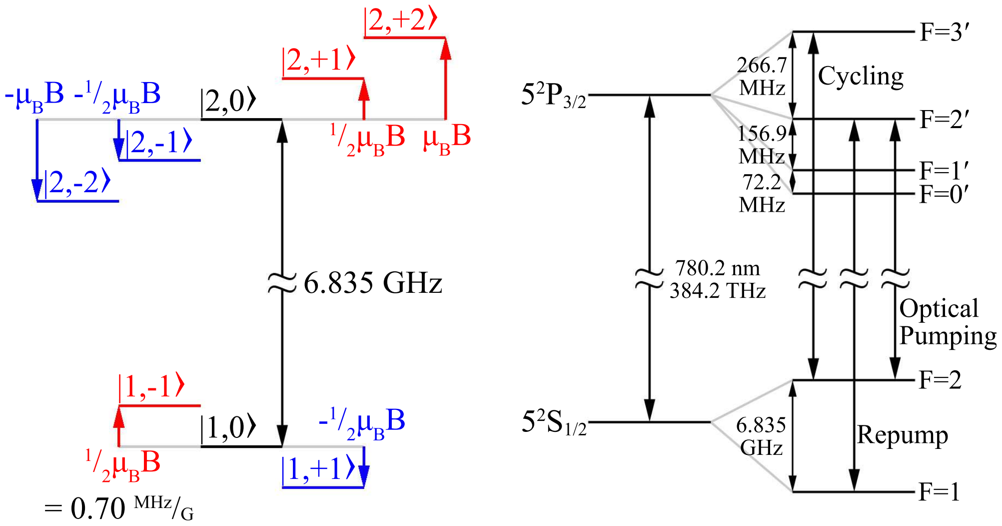

(a) (b)

Figure 1.2: Illustrations of the electronic structure of ^{87}Rb. Part (a) shows the ground state structure of ^{87}Rb, showing hyperfine and Zeeman splitting. Here, and throughout this thesis, red is used for magnetically trappable ($g_F m_F > 0$) states, blue for magnetically untrappable ($g_F m_F < 0$) states, and black for magnetically unaffected ($g_F m_F = 0$) states.
Part (b) shows the hyperfine structures of the ground and $5^2\mathrm{P}_{3/2}$ excited states and three important transitions between them. The scale of hyperfine splitting is twenty times larger for the excited state than for the ground state and Zeeman splitting is omitted for simplicity.

1.4 BECs at Amherst

In this section, we will provide a brief overview of the experimental procedure that produces the condensate with which we work. Our purpose here is to provide a familiarity with the theory and techniques of atomic trapping and cooling, as well as with the techniques' specific implementation in our apparatus, that will inform the discussion of our own experimental procedures later. For a more comprehensive and detailed description of the underlying theory or experimental implementation of any of these steps, we would encourage one to consult the theses of the past students who were instrumental in the construction of the apparatus [4, 17, 26–28].

First, we will sketch out a concise narrative of the complex sequence of events that is involved in preparing a Bose-Einstein condensate for our experiment. Speaking in the broadest possible terms, the apparatus consists of two Pyrex cells connected by a thin stainless steel manifold and maintained under ultrahigh vacuum [17]. ^{87}Rb atoms are evaporated by the getter dispensers into the collection cell, where they are cooled and trapped by optical molasses and a magneto-optical trap (MOT). The collection atoms, prior to the point of Bose-Einstein condensation, is known as a thermal cloud. The clouds of evaporated atoms being held in the collection cell are periodically transferred through the manifold until the desired number of atoms has accumulated in the science cell.

Once this point has been reached, the atoms are cooled further in a second

MOT and then transferred to a compressed magneto-optical trap (CMOT). At this point, all lasers are turned off and the atoms are transferred into a purely magnetic time-averaged orbiting potential (TOP) trap. The TOP, aided by RF evaporation, evaporatively cools the atoms further until they reach the critical phase space density for Bose-Einstein condensation. Once the condensate has formed, we have the option of creating a rotating perturbation of the magnetic field that imparts angular momentum to the condensate and forms vortices. The atoms are then transferred from the TOP trap to a far off-resonance optical dipole trap (FORT). At this point, we conduct the experiments described in Chapters 2 and 3. At the end of this process, the atoms are released from the optical trap and allowed to fall and undergo ballistic expansion before being imaged.

1.4.1 Collection

Gaseous ^{87}Rb atoms are supplied to the system by four rubidium getter dispensers. One pair of getters is mounted directly into the glass of the collection cell while the other is mounted in an adjacent cartridge and connected via a conflat vacuum flange. This latter pair is theoretically replaceable, but doing so would break the 10^{-9} Torr vacuum that has been maintained continuously since the system was baked out in November of 2000. The getters are heated by resistive heating and atoms sublimate into the collection cell. The cell itself is a six-way cross with 1.5-inch diameter windows on all ends for the MOT beams and a smaller window and port on the diagonal for transfer of the atoms to the science cell.

Optical Molasses

Upon vaporization into the collection cell, the slower atoms are initially cooled in an optical molasses [10]. The atoms are subjected to a radiation force from six mutually orthogonal directions by lasers that are slightly red-detuned from the $2 \rightarrow 3'$ transition. This is accomplished by locking a master laser via saturated absorption spectroscopy to the neighboring $2 \rightarrow 2', 2 \rightarrow 3'$ crossover peak [29] and modulating the beam with an acousto-optic modulator to a frequency approximately 18.5 MHz, or about 3 natural linewidths, below that of the $2 \rightarrow 3'$ "cycling" transition. The master beam is then used to injection lock three amplifier beams which each illuminate one axis from both directions.

As we will demonstrate analytically, as an atom moves toward the source of a specific laser, that laser is Doppler-shifted into resonance with the atom. Each absorbed photon imparts a small amount of momentum to the atom in the direction of propagation of the laser while the subsequent re-emission of the photon is isotropic and thus imparts no net momentum to the atom. Therefore, in the following analysis, we will only be concerned with the momentum of the absorbed photons.

Consider an atom in one dimension, motionless at this point, with one laser incident upon it from each direction. The lasers are each red-detuned by Δ from a specific transition with central frequency ν_0, or $\Delta \equiv \nu_0 - \nu$. The spectral profile of the absorption peak is given by the Lorentzian distribution,

$$P(\nu) = \frac{1}{\pi}\frac{\Gamma/2}{(\nu_0 - \nu)^2 + (\Gamma/2)^2}, \tag{1.20}$$

where Γ is the natural linewidth of the transition [30]. Because the atom is stationary until explicitly stated otherwise, this linewidth represents only natural and not doppler broadening. Therefore, the probability of absorption of a photon of a frequency between ν and $\nu + \mathrm{d}\nu$ is given by $P(\nu)\mathrm{d}\nu$. Since our aim here is not to calculate the magnitude of the force exerted on the atom by the photons but merely its direction, we define the laser intensity I so that

$$\frac{dn}{dt} = IP(\nu)\mathrm{d}\nu \tag{1.21}$$

represents the absorption rate of photons of frequency ν (meaning between ν and ν+dν) emitted by one laser. Each photon absorbed imparts a momentum

$$p_\gamma = \frac{h\nu_0}{c} \tag{1.22}$$

to the atom. Here, we assume that the radiation is sufficiently close to absorption (i.e. $\Delta \ll \nu_0$, or 18.5 MHz $\ll$ 384 THz for our apparatus) so that the momenta of the photons can be calculated using the central frequency. Therefore, the force exerted on the atom by the absorption of photons of frequency ν emitted by one laser is given by

$$|F_\gamma| = \frac{dn}{dt}p_\gamma = \frac{Ih\nu_0}{c}P(\nu)\mathrm{d}\nu. \tag{1.23}$$

Now, consider the atom to be moving with velocity v. We define laser A to be propagating from the positive direction and laser B to be propagating from the negative direction. Because of the atom's velocity, the detuning term $(\nu_0 - \nu)$ from Eq. 1.20 becomes the Doppler-shifted detuning

$$\Delta' = \nu_0 - \nu\left(1 \pm \frac{v}{c}\right) = \Delta \mp \frac{v}{c}(\nu_0 - \Delta) \approx \Delta \mp \frac{v}{c}\nu_0, \tag{1.24}$$

where the top operators are read for laser A and the bottom for laser B. We again claim that the laser frequency is sufficiently close to the transition that we are able to neglect the second-order $\Delta(v/c)$ term. Photons emitted from laser A have momentum $-h\nu_0/c$ so their absorption exerts a force in the negative direction, and vice versa for laser B. With this in mind, we substitute the Doppler-shifted detuning from Eq. 1.24 into Eq. 1.20 and substitute the result into Eq. 1.23 to find

$$F_\gamma = \mp\frac{Ih\nu_0}{\pi c}\frac{\Gamma/2}{(\Delta \mp v\nu_0/c)^2 + (\Gamma/2)^2}\mathrm{d}\nu. \tag{1.25}$$

Next, we simply sum the contributions to the force from each laser and perform some algebraic manipulation to find the net force

$$F_{\gamma,\mathrm{net}} = -\frac{2Ih\nu_0^2\Delta\Gamma}{\pi c^2}\frac{v}{g(v)}\mathrm{d}\nu, \tag{1.26}$$

with

$$g(v) = (\nu_0 v/c)^4 + 2(\nu_0 v/c)^2\left[(\Gamma/2)^2 - \Delta^2\right]^2 + \left[(\Gamma/2)^2 + \Delta^2\right]^2. \tag{1.27}$$

It is important to notice that the first term is composed entirely of positive constants. Similarly, $g(v)$ depends only on v^2 and can be shown to be positive for all real values of v. The one-dimensional result can be easily generalized to three dimensions to demonstrate that a particle in optical molasses experiences a force that is always opposite in direction to its motion. This has the effect of compressing the velocity distribution of the atoms and thereby cooling the thermal cloud. The limiting factor in the cooling of the atoms in optical molasses is the radiation pressure caused by the rescattering of photons, which places a lower limit on the temperature that can be reached at this stage.

Magneto-Optical Trap

While optical molasses slows the atoms, it cannot provide spacial confinement. Gravity would slowly pull the atoms downward until they escaped the optical molasses or atoms would simply travel out of the optical molasses slowly were it not for magneto-optical trapping. The magneto-optical trap is not so much an independent system as a refinement of the optical molasses. A pair of coils in the anti-Helmholtz configuration creates a magnetic field minimum in the center of the collection cell and the six lasers used in optical molasses are circularly ($\sigma^{\pm}$) polarized.

To illustrate how this configuration provides spatial confinement, consider a simplified one-dimensional model [30]. Our theoretical atom contains only two states, a ground state with zero angular momentum and $F = 0$ ($m_F = 0$) and an excited state with $F = 1$ ($m_F = -1, 0, +1$). The projection of this angular momentum onto the z-axis is $m_F\hbar$ and the magnetic field is given by $B(z) = B_0 z$. The circular polarization of each laser is taken to be the same as its direction of propagation, as determined by the right-hand rule, so the laser incident from the $+\hat{\mathbf{z}}$ direction is left-polarized and the laser incident from the $-\hat{\mathbf{z}}$ direction is right-polarized.

Right- or left-polarized light, when its direction of incidence is parallel to the magnetic quantization axis, is $\sigma_{\pm}$-polarized and can only drive transitions with $\Delta m_F = \pm 1$. Therefore, the σ^{+}-polarized laser incident from the $-\hat{\mathbf{z}}$ direction can only drive the $|0,0\rangle \rightarrow |1,+1\rangle'$ transition and the σ^{-}-polarized laser incident from the $+\hat{\mathbf{z}}$ direction can only drive the $|0,0\rangle \rightarrow |1,-1\rangle'$ transition. At positive values of z, the $m_F = -1$ state is lowered in energy relative to the ground state and the $m_F = +1$ state is raised. Because the incident radiation is red-detuned from the transition frequency, the $|0,0\rangle \rightarrow |1,-1\rangle'$ level spacing is tuned closer to the laser frequency and the $|0,0\rangle \rightarrow |1,+1\rangle'$ level spacing is tuned further from it. Therefore, the atom preferentially absorbs photons from the σ^--polarized laser and experiences a net radiation force in the $-z$ direction.

This simple analysis can be applied to ^{87}Rb using any Zeeman state of the $F = 2$ hyperfine manifold as the simplified $F = 0$ state. It can easily be shown that for any state $|2, m_F\rangle$, the relative energy of the $|3, m_F + 1\rangle'$ state increases and the relative energy of the $|3, m_F - 1\rangle'$ state decreases as B increases in the positive direction. The magnitudes of the rises and falls in the energies of the $|3, m_F \pm 1\rangle'$ states relative to the $|2, m_F\rangle$ state are dependent on the specific value of m_F. This Zeeman detuning in the transition frequency is added to the Doppler detuning derived in the previous section, resulting in a net force that both slows the atoms and confines them to the field minimum in the center of the collection cell.

Additionally, the MOT lasers preferentially drive σ^+ transitions, for which $\Delta m_F = +1$. This pumps atoms towards the "stretched" states $|2, +2\rangle$ and $|3, +3\rangle'$, which have the maximum possible z-projections of their angular momentum. Because selection rules for emission and absorption stipulate that $|\Delta m_F| \leq 1$ for every allowed transition, atoms that are excited into the $|3, +3\rangle'$ state can only decay to the $|2, +2\rangle$ state and thus remain trapped in a stable $2 \leftrightarrow 3'$ cycle.

The picture is complicated further when the multilevel ground and excited states of ^{87}Rb are considered. The MOT lasers are detuned approximately 18.5 MHz, or about three natural linewidths, below the cycling transition frequency but they are also only detuned approximately 140 MHz, or about

22 natural linewidths, above the $2 \rightarrow 2'$ "optical pumping" transition frequency. Therefore, a $\sigma^{\pm}$ photon occasionally excites an atom to the $F = 2'$ level instead of the intended $F = 3'$ level. From the $F = 2'$ level, atoms decay with equal probability to either the $F = 2$ or $F = 1$ ground state hyperfine manifolds.

Since optical molasses and magneto-optical trapping drive the $2 \rightarrow 3'$ cycling transition, only atoms in the $F = 2$ hyperfine manifold can be trapped in this manner. To prevent trap loss from the $F = 1$ atoms, an additional σ^{+}-polarized "repump" laser drives the $|1, m_F\rangle \rightarrow |2, m_F + 1\rangle'$ transition. From the excited state, the atoms again can either decay to the $F = 1$ hyperfine manifold, from which they would be excited again by the repump beam, or to the $F = 2$ hyperfine manifold, in which they would be trapped by the MOT's cycling beam. This serves to "pump" atoms towards $F = 2$ states with higher values of m_F and to depopulate the $F = 1$ manifold. Because of the combined effects of the cycling and repump lasers, atoms accumulate in the $|2, +2\rangle$ state.

Transfer

Our collection and science cells constitute a dual MOT, differentially pumped system of the type developed by Myatt et al. [31]. Once several million atoms have collected in the collection cell, they must be transferred to the science cell. To accomplish this, the magnetic field and trapping beams are shut off as the atoms are exposed to a "push" beam. The push beam is σ^{+}-

polarized and detuned 13 MHz, or about 2 natural linewidths, below the cycling transition frequency, allowing it to impart momentum to the atoms while pumping them into the magnetically trappable $|2, +2\rangle$ state. It is aligned on the transfer axis of the apparatus, passing through the centers of the collection cell, transfer tube, and science cell.

The two cells are connected by a stainless steel manifold 18 inches long and with an approximate inner diameter of 1/2 inch [17]. The manifold is encased by an array of permanent magnets in a hexapole configuration, which serves to increase the efficiency of the transfer process. The length and narrowness of the tube inhibit the flow of extraneous gas between the two cells so that the science cell can be maintained at a pressure of $\sim 10^{-11}$ Torr while the pressure inside the collection cell is $\sim 10^{-9}$ Torr. The collection cell is held at a higher pressure because the increased ^{87}Rb vapor pressure results in higher occupancy and faster trap loading, whereas the science cell is maintained at a lower pressure because the absence of extraneous room-temperature atoms results in an increased trap lifetime.

Once the atoms reach the science cell, they are collected in a second MOT. A photodiode mounted near the cell monitors the amount of light scattered by the atom cloud to provide a relative measure of the number of trapped atoms. This process is repeated every second until the voltage registered by the photodiode reaches a threshold value, a preset "fill level."

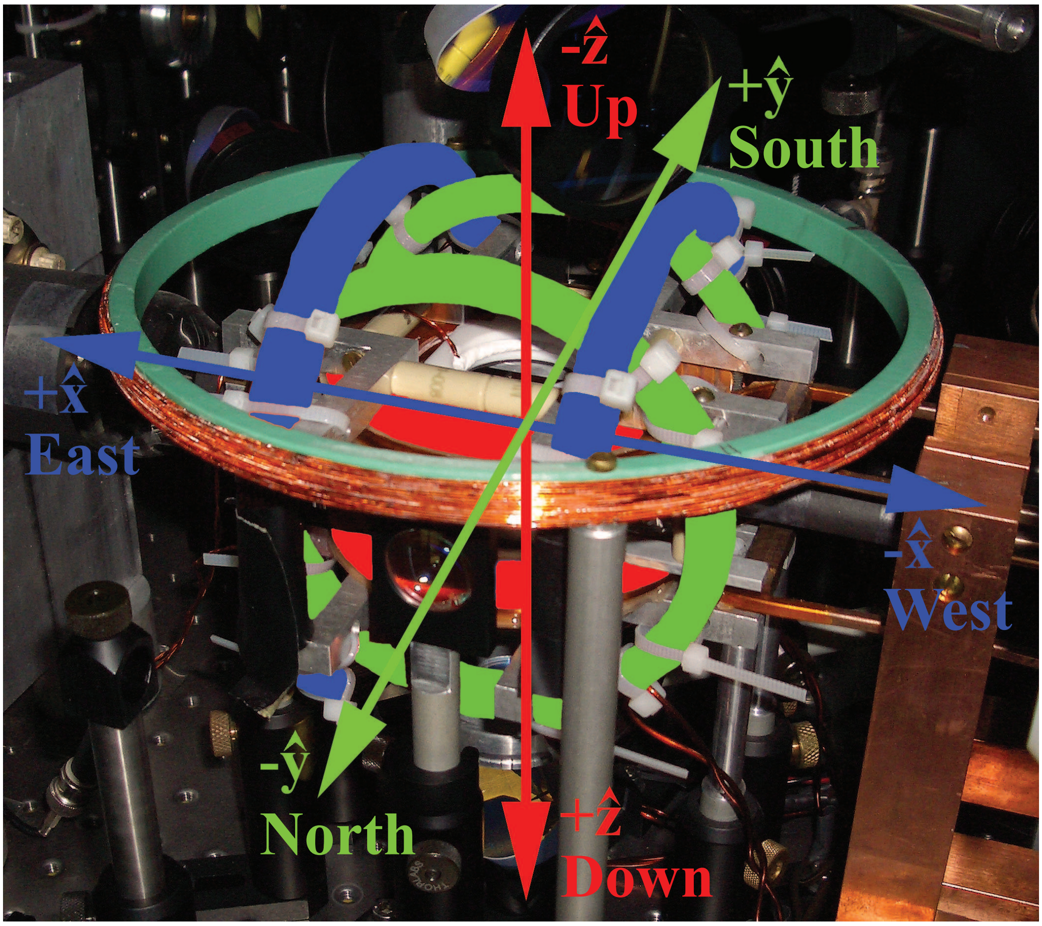

Figure 1.3: Illustration of the science cell magnetic coil configuration and definition of the laboratory reference frame. Here, we define our coordinates so that the AF (audio frequency)/bias coils and Helmholtz quadrupole coils create static fields in the $+\hat{\mathbf{x}}$, $+\hat{\mathbf{y}}$, and $+\hat{\mathbf{z}}$ directions, respectively. Highlighted are the North-South AF/bias coils in green, the East-West AF/bias coils in blue, and the vertical quadrupole coils in red. The single large coil in the green wire guide is the vertical bias coil. A matching vertical bias coil has been added below the cell since this photograph was taken but a photograph taken now would show the coil assembly partially obscured by the FORT final mirrors. The smaller vertical and horizontal RF coils, not distinctly shown, are situated within the upper quadrupole coil and northern AF/bias coil, respectively. The East-West and North-South shim coils, which cancel components of the Earth's magnetic field, are not shown because they are much larger and farther from the cell.

1.4.2 Evaporation

The science cell, where the atoms are Bose-Einstein condensed and where our experiment is conducted, is a $4 \times 1 \times 1$-inch rectangular cell with vacuum flanges on both ends. One flange couples the cell to the transfer manifold and allows the entry of ^{87}Rb atoms. The other flange couples the cell to an ion pump and a titanium sublimation pump, which maintain ultra-high vacuum in the cell [27].

Fig. 1.3 depicts the magnetic coil configuration of the science cell. The quadrupole coils each consist of ten windings of square, hollow wire. Because we routinely run over 400 amps of current through these coils, cool water is pumped through the hollow center of the wire to dissipate the substantial Joule heat created. When 580A, the maximum current our power supply can provide, is run in the Helmholtz (parallel current) configuration, the coils can produce a static field of up to 1200 G in the downward ($+\hat{\mathbf{z}}$) direction [26]. This configuration is used primarily for providing a steady axial field once the atoms are in the optical trap and for Landau-Zener transitions, as described in Section 2.2. When the current in the bottom coil is reversed to run in the anti-Helmholtz configuration, the quadrupole coils produce zero magnetic field at the center of the pair and a field gradient of up to 248 G/cm in the axial direction and 124 G/cm in the radial direction [26]. This configuration is used primarily for all magnetic trapping and for Stern-Gerlach separation, as described in Section 2.3. In our anti-Helmholtz configuration, current is run such that $\partial B_z/\partial z < 0$ and, by consequence of cylindrical symmetry of the coils and the conservation of magnetic flux (stated explicitly in Eq. 2.40), $\partial B_\rho/\partial\rho = -\frac{1}{2}(\partial B_z/\partial z) > 0$ at the center of the pair.

The four AF (audio frequency)/bias coils each consist of thirty-three windings of thinner 14 AWG wire [26]. Because of spatial considerations, the North-South coils are smaller, with a mean radius of 2.6 inches, and are nested inside of the larger East-West coils, which have a mean radius of 3.0 inches. Currently, these coils are run only in the Helmholtz configuration and can either create steady independent bias fields in the East $(+\hat{\mathbf{x}})$ and South $(+\hat{\mathbf{y}})$ directions or, by sinusoidally modulating the currents in the two pairs with a 90° phase shift, a bias field that rotates through the entire xy-plane at 2 kHz. We are planning, however, to implement an upgrade to the coils' current source that has recently been constructed by Melissa Moulton. Once implemented, this upgrade will enable us to control the current in each coil independently in the steady-field configuration. This will allow us to create a steady bias field in any arbitrary orientation in the xy-plane, instead of only those lying in the North-East quadrant. We will also be able to create superpositions of Helmholtz and anti-Helmholtz currents in each pair of coils, resulting in a field that has both a non-zero magnitude and non-zero gradients at the center of the pair.

Compressed MOT

Once the desired number of atoms have been transferred into the science MOT, they are transferred into a compressed magneto-optical trap (CMOT)

[32]. In the MOT, the density of the atoms is limited by the scattering of photons from the atoms, which creates a reradiation force that supports the thermal cloud against the compressing force of the trap. By removing the repump beam and detuning the MOT cycling beams even further to the red, the reradiation force is drastically reduced and the cloud collapses. The increase in density coincides with an increase in temperature, but the increases are such that the overall phase space density remains roughly constant.

Once the cloud has been allowed to rethermalize in the CMOT, the quadrupole coils are ramped off and the cloud expands in the optical molasses, cooling it even further. Since the MOT beams are further red-detuned, the radiation pressure caused by photon scattering is lessened and the atoms are cooled even beyond the limits of the collection and science MOTs. This stage also results in the atoms being distributed among the various states of the $F = 2$ hyperfine manifold.

Optical Pumping

In order to proceed with condensation, we must collect the atoms into either the $|2, +2\rangle$ or the $|1, -1\rangle$ state. We prepare the atoms in these states because they, along with the $|2, +1\rangle$ state, are magnetically weak field-seeking. Since $g_F m_F > 0$ for each of these states, their energies are raised by Zeeman splitting, as per Eq. 1.13, and atoms in these states are attracted to regions of low field magnitude. The $|2, +1\rangle$ state is eliminated as a possibility for direct condensation because of unacceptably high two-body loss rates. Two

$|2,+1\rangle$ atoms can exchange angular momentum to become a $|2,+2\rangle$ atom and a $|2,0\rangle$ or $|1,0\rangle$ atom [28, 33]. The latter interaction also releases 6.835 GHz of energy per interaction, which ejects the pair of atoms from the condensate and possibly heats other condensed atoms as well.

At this point, we can choose the state in which we want to make a condensate. We use $|1,-1\rangle$ condensates for the experiments outlined in this thesis, but producing a condensate in the $|2,+2\rangle$ state has certain advantages. The state's primary advantage is its larger magnetic moment, which allows its atoms to be trapped more tightly in the magnetic TOP trap. This allows us to evaporate a $|2,+2\rangle$ thermal cloud to condensation more quickly and reliably than a $|1,-1\rangle$ thermal cloud. This reliable high-speed condensation makes $|2,2\rangle$ condensates ideal for straightforward experiments, such as alignment of the optical trap, that involve producing a series of condensates as rapidly as possible. The more robust production of $|2,+2\rangle$ condensates is also less sensitive to various beam misalignments. There have been several instances in which the production of $|1,-1\rangle$ condensates was severely compromised but the reliable production of $|2,+2\rangle$ condensates allowed us to narrow the range of possible problems.

In order to pump the atoms into the selected state, we apply 50 μs pulses of circularly polarized light tuned to the $2 \rightarrow 2'$ optical pumping transition. The polarization is defined by a magnetic quantization axis provided by a rotating bias field, so these pulses must be emitted in phase with the field's rotation. To prepare a thermal cloud composed entirely of $|2,+2\rangle$ atoms, the light is σ^+-polarized and the pattern of transitions is similar to those that occur in the MOT. At the beginning of this stage, the atoms are distributed randomly within the $F = 2$ hyperfine manifold. The radiation excites atoms from the $|2, m_F\rangle$ state to the $|2, m_F + 1\rangle'$ state, from which they can decay with equal probability to either ground state hyperfine manifold. As in the MOT, atoms that decay to the $F = 1$ manifold are promptly excited by the high-intensity repump beam. Through successive excitations and decays, atoms are pumped by the two beams to the "dark" $|2, +2\rangle$ state. This state is called "dark" because atoms in it cannot interact with the incident radiation; the repump beam is tuned to the $1 \rightarrow 2'$ transition and the optical pumping beam cannot excite a transition to the non-existent $|2, +3\rangle'$ state. As a result, we are left with a thermal cloud composed entirely of $|2, +2\rangle$ atoms.

This mechanism can be used to prepare a thermal cloud of $|1, -1\rangle$ atoms with two simple changes. First, by inserting a π phase shift between the radiation pulses and the magnetic field rotation, the polarization of the optical pumping beam is changed from σ^+ to σ^-. Second, the intensity of the repump beam is drastically reduced. The σ^--polarized light pumps atoms to $2'$ states with lower values of m_F, from which they can decay to either ground state hyperfine manifold. The lowered intensity of the repump beam reduces the frequency with which atoms are excited out of the $F = 1$ manifold, allowing atoms to accumulate in the $|1, -1\rangle$ state. The $|2, -2\rangle$ state is dark to the σ^--polarized beam but the polarization of the beam with respect to the rotating magnetic field is imperfect. This imperfection makes linearly-or π-polarized transitions, for which $\Delta m_F = 0$, possible. Thus, atoms can be excited from this dark state to the $|2, -2\rangle'$ state and then decay to accumulate in the $|1, -1\rangle$ state.

Magnetic TOP Trap

The MOT, CMOT, and optical molasses function by using the momentum imparted by resonant photons to slow the atoms, but this photon scattering also places a lower limit on the temperature to which the condensate can be cooled by optical means. To cool the condensate beyond this limit and to the point of condensation, we must transfer the atoms into the purely magnetic time-averaged, orbiting potential (TOP) trap [34]. The atoms have been pumped entirely into either the $|1, -1\rangle$ or $|2, +2\rangle$ weak field-seeking magnetic sublevels, so they are attracted to the field minimum in the center of the cell.

The anti-Helmholtz quadrupole by themselves actually create a point of zero magnetic field in the center of the trap, which is known as the "hole of death." Were an atom to actually reach the hole of death, the orientation of the atom with respect to the magnetic field would change more quickly than the atom's magnetic moment could precess around to follow it [35]. This would cause the atom to undergo a Majorana transition to an untrapped state and be expelled from the trap. To prevent this, we use the AF coils to create a rotating bias field that displaces the "hole of death" horizontally away from the center of the trap. As a result, the atoms collect in the time-averaged field minimum in the center of the trap while the hole of death orbits around them at approximately 2kHz. This frequency is lower than the Larmor frequency, the frequency at which the atoms' magnetic moments precess about the bias magnetic field, so that the precession can follow the rotating field adiabatically [26]. The frequency is high enough, however, that the majority of the atoms cannot move quickly enough to reach the hole of death.

Conveniently, the atoms that can reach the hole of death are by necessity the fastest and most energetic atoms in the thermal cloud. Thus, as the most energetic atoms reach the hole of death and are expelled, the average energy of the thermal cloud is lowered and the atoms cool. This process is known as evaporative cooling and is analogous to how a hot cup of soup cools as the most energetic water molecules boil off. We take advantage of this self-selective removal from the trap by lowering the magnitude of the rotating bias fields, which moves the "hole of death" closer to the center of the trap. Here, we must balance the competing needs of evaporating atoms quickly and allowing the remaining atoms to rethermalize. Decreasing the bias field exponentially would be the most efficient method but we have found that decreasing the field in two linear stages works sufficiently well for evaporating both states [27]. This process cools the thermal cloud to a temperature of a few microkelvin but this is still well above the threshold for condensation. We could use evaporative cooling to cool the thermal cloud to the point of condensation, but completing the process using RF evaporation is far more efficient [4].

RF Evaporation

The final step to Bose-Einstein condensation is RF evaporation. We bathe the thermal cloud in radio-frequency radiation in order to excite transitions between trapped and untrapped magnetic sublevels and expel certain atoms from the trap. In describing this process, it is easiest to use the image a surface of constant field magnitude surrounding the hole of death [4]. At every point on this surface, which has the shape of an oblate spheroid, the magnitude of the Zeeman splitting an atom experiences is necessarily also constant. This surface is called the "RF knife" because RF radiation of a given frequency will eject the atoms on this surface from the trap. The atoms that are able to travel the farthest away from the field minimum in the center of the trap and reach the highest magnetic fields are the most energetic. By starting the RF frequency high, at 12 MHz, and gradually lowering it, we slowly contract the RF knife around the thermal cloud. As the most energetic atoms are cut away, the remaining atoms rethermalize via inelastic collisions and cool. Eventually, this process lowers the temperature and raises the phase space density enough so that Bose-Einstein condensation is accomplished.

In the summer of 2005, the author of this thesis installed a significant hardware upgrade to this system. The function generators we use to drive current through the RF coils are incapable of a phase-continuous frequency sweep, so we approximate a smoothly descending line with a series of descending steps. This concept is discussed later in greater detail in the context of the Landau-Zener magnetic field sweep. The function generator that was in place prior to this upgrade was capable of switching frequencies in 70-100 ms, resulting in a course stepwise approximation of a steady decline. Our task was to install a recently purchased PTS 310 function generator that is capable of switching frequencies in 5 microseconds. To this end, we constructed an electronically buffered interface box and, braving the vagaries of C, wrote software to allow the function generator to be controlled electronically. As a result, we can produce a far better approximation to a smooth frequency ramp. We can also program in a brief abrupt frequency decline at the end of the sweep, a technique that has been shown to produce larger condensates. This upgrade increased our maximum condensate population by a factor of 2, from 5×10^5 [28] atoms to more than 1×10^6 atoms.

1.4.3 Manipulation and Imaging

Once we have produced a Bose-Einstein condensate in the TOP trap, we can manipulate it in various ways before proceeding on to the experiments that form the basis of this thesis.

Vortex Production

While the condensate is in the TOP trap, we can induce vortices in the condensate by imparting angular momentum to it. By varying the magnitudes of the fields produced by the two pairs of AF coils, we elongate the orbit of the hole of death into an ellipse. We then rotate the major axis of the elliptical orbit, which exerts a torque on the condensate. At present, we are taking the first steps towards merging our vortex studies with several major topics addressed in this thesis. We have already observed vortices in optically trapped [4] and spinor [5] condensates and we plan to produce an atom laser containing a single vortex core. Other future investigations could possibly study the dynamics of a vortex-laden condensate around a Feshbach resonance, observing how changing the scattering length affects vortex evolution. For a far more comprehensive and enlightening discussion of all things vortex, we would recommend reading Elizabeth Petrik's thesis [5].

Transfer to Optical Trap

Our investigations of spinor condensates and Feshbach resonance involve atoms in magnetic sublevels that cannot be magnetically trapped, so we must transfer the condensate from the magnetic trap to the optical far off-resonance trap (FORT) [36]. For a detailed discussion of theory and design of the FORT, we would recommend reading Daniel Guest's thesis [4]. The optical trap consists of two horizontal beams that cross at a right angle. The lasers are tuned to 1064 nm, which is far detuned from the two optical transitions in ^{87}Rb at 795.0 nm and 780.4 nm. This detuning is necessary because resonant radiation would reheat the atoms through photon scattering and destroy the condensate. We ramp the anti-Helmholtz magnetic field down as we ramp the optical trap power up, gently transferring the atoms from one trap to the other. Appendix A contains a derivation of the optical trapping potential, which is simply proportional to the light intensity at any given point. By bringing the two crossed beams to a focus at the center of the trap, we create an optical potential well that overlaps the magnetic potential well. As demonstrated by Fig. A.2, a series of contour plots of the calculated optical trap potential, this potential well is approximately cylindrical close to its center. This allows us to create vortices that circulate around a vertical axis in the magnetic trap and then transfer them to the optical trap [5].

To perform the experiments described in this thesis, we need the condensate to be optically trapped and in a steady field created by the AF/bias coils and the quadrupole Helmholtz coils. To this end, we must switch the AF/bias coils from their rotating field configuration to their steady field configuration and switch the quadrupole coils from their anti-Helmholtz to their Helmholtz configuration. For technical reasons, these current switches can only be thrown with no current running through the coils. We cannot, however, allow the magnetic field to go to zero at any time because the atoms would undergo Majorana transitions and distribute themselves among the magnetic sublevels. Since the optical trap is independent of the atoms' magnetic moments, these distributed atoms would not be expelled from the trap but we would lose control of the spin degree of freedom.

In order to switch from a rotating field to a steady field with the magnetic quantization axis intact, we first bring the current running through the quadrupole coils to zero. We then switch them to their Helmholtz configuration and ramp the field linearly up to 10.0 G in the $+\hat{\mathbf{z}}$ direction over 3.0

ms. Then, we ramp the current running through the AF/bias coils to zero over 3.0 ms and flip the current switches from our audio-frequency oscillating current source to our steady current source. Finally, we ramp the bias fields up to the values calibrated to produce zero net magnetic field in the center of the trap. At this point, we are left with the $|1, -1\rangle$ or $|2, +2\rangle$ atoms in a 10.0 G field supplied by the Helmholtz quadrupole coils and the ability to produce any arbitrary bias field allowed by the technical limitations of our apparatus. This field configuration provides an ideal starting point from which we can begin an experiment on spinor condensates, Feshbach resonance, or any other topic involving optically trapped condensates.

Imaging

The majority of the data we collect about the condensate is taken by absorptive imaging, which Jason Merrill and Theodore Reber describe at length in their theses [27, 28]. We shine a resonant or near-resonant probe beam on the condensate, which scatters some of the light and creates a shadow in the beam. A charge-coupled device (CCD) camera measures this shadow, from which we can infer the optical density and atomic density of the condensate. Signal saturation occurs, however, because there exists a maximum rate at which the atoms of the condensate can scatter photons. When an atom is in an excited state, it requires a finite amount of time to decay back to the ground state and cannot absorb another photon until it has done so. To correct for saturation, we slightly detune the laser from resonance, which

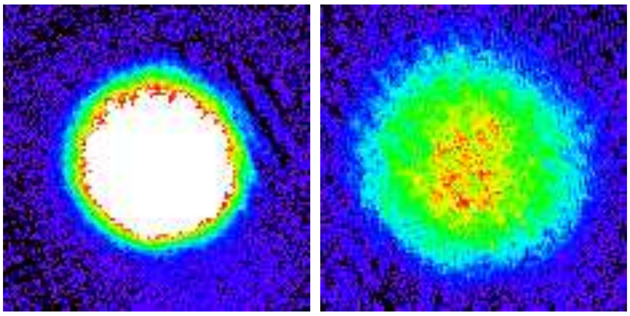

Figure 1.4: Condensates imaged using saturated on-resonance (left) and unsaturated detuned (right) radiation.

decreases the optical depth of the condensate. The laser is locked via saturation absorption spectroscopy to a peak approximately 120-130 MHz from the $2 \rightarrow 3'$ cycling transition and shifted into resonance by an AOM. This mechanism provides very precise control of the laser's detuning from resonance. Examples of condensates imaged using saturated on-resonance and unsaturated detuned radiation are shown in Fig. 1.4.

Before imaging, we release the condensate from the optical or magnetic trap. As the condensate falls, it undergoes ballistic expansion until we image it. We can either shine the probe beam horizontally or vertically through the cell. These two imaging methods, known as "side-view" and "top-view" imaging, respectively generate images that present the perspectives of looking at the condensate from the North and upward at the condensate from below. The majority of images taken for this thesis were collected using side-view imaging, but top-view imaging will play an important role in the continuing study of a Feshbach resonance, as is discussed in Chapter 3.

Chapter 2

Spinor Condensates

The primary advantage of the optical trap is that it allows manipulation of our condensate's spin degree of freedom. In the magnetic trap, we can hold and manipulate only the three magnetically trappable states, $|1,-1\rangle$, $|2,+1\rangle$, and $|2,+2\rangle$. Because the optical trapping potential is independent of magnetic moment, though, the optical trap enables us to trap and experiment on any of the eight magnetic sublevels of the ground state.

In particular, we are interested in the three magnetic sublevels of the $F = 1$ hyperfine manifold for two reasons. First, the three-state Landau-Zener problem presented by the $F = 1$ manifold is theoretically simpler than the five-state problem presented by the $F = 2$ manifold. Second, to study the interspecies Feshbach resonance that is described in Chapter 3, we need to produce a binary condensate composed of atoms in the $|1,+1\rangle$ and $|2,-1\rangle$ states. We cannot transfer a condensate of $|2,+2\rangle$ atoms entirely to the

$|2,-1\rangle$ state by a Landau-Zener sweep alone, so we would have to transfer the entire population to the $|2,-2\rangle$ state via a Landau-Zener sweep and then to the $|2,-1\rangle$ state via a radio-frequency pulse. We would then transfer half the population to the $|1,+1\rangle$ state via a two-photon pulse. It is far simpler, then, to transfer the entire population from the $|1,-1\rangle$ state to the $|1,+1\rangle$ state and then transfer half of the population to the $|2,-1\rangle$ state via a two-photon pulse, as we will describe in Chapter 3.

By producing a condensates in the $|1,-1\rangle$ state and then transferring atoms to the other $F = 1$ states, we create a condensate that has atomic spin as a degree of freedom. This is known as a spinor condensate and was first produced in a condensate of sodium atoms by the Ketterle group in 1998 [37]. Because of this additional degree of freedom, spinor condensates exhibit several quantum phenomena, briefly described below, that are absent in scalar condensates [38].

First, the lowest-energy state of a spinor condensate depends critically on the s-wave scattering length a. This parameter is central to our discussion on Feshbach resonance and will be explained more carefully in Chapter 3, but it suffices for now to say that a is a measure of the interaction strength between atoms in the condensate. Interatomic interactions are attractive for $a < 0$ and repulsive for $a > 0$. To find the lowest-energy state of a spinor condensate of atoms with $F = 1$, we compare the scattering lengths of two atoms whose total angular momenta are parallel ($F = 2$) or anti-parallel ($F = 0$). If $a_{F=0} > a_{F=2}$, then the repulsion between atoms with anti-parallel angular momenta is stronger than that between atoms with parallel angular momentum, and the system minimizes its energy when atoms are collected into the same state. Systems that meet this condition, such as ^{87}Rb with $a_{F=0} = 101.8(2)a_0$ and $a_{F=2} = 100.4(1)a_0$ [39], where a_0 is the Bohr radius, are known as ferromagnetic spinor condensates. Conversely, systems for which $a_{F=0} < a_{F=2}$, such as the first spinor condensate created in ^{23}Na, are known as polar spinor condensates.

In ferromagnetic spinor condensates such as ours, it has been theoretically shown [38] that single vortices with more than one unit of angular momentum are topologically and energetically unstable. Ferromagnetic spinor condensates can, however, support metastable Skyrmion vortices. A Skyrmion vortex is one in which atoms in one spin state circulate around a vortex core composed of atoms in another spin state [40]. At present, our optical trap lacks the high degree of long-term stability necessary to conduct a comprehensive investigation of vortices in a spinor condensate. Despite this instability in the FORT beam, we have created spinor atom lasers via outcoupling from the optical trap by gravity. We have also used the preferential spatial separation of the components of a spinor condensate to diagnose stray magnetic field gradients in the apparatus. These experiments, and details of the Landau-Zener transitions we use to create spinor condensates, are described in this chapter.

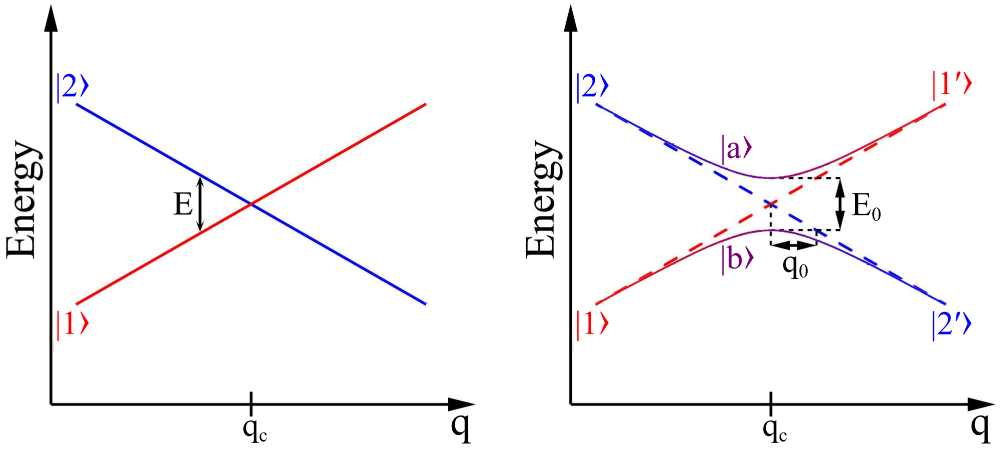

(a) (b)

Figure 2.1: Diagrams of abstract two-state Landau-Zener crossings. These diagrams show the energies of the (a) unperturbed and (b) perturbed states as functions of a generic parameter q. The unperturbed states $|1\rangle$ and $|2\rangle$ are degenerate at q_c, while the perturbed states $|a\rangle$ and $|b\rangle$, which are linear superpositions of $|1\rangle$ and $|2\rangle$, undergo an avoided crossing with separation E_0 and width q_0.

2.1 Landau-Zener Theory

2.1.1 Abstract Landau-Zener Theory

In this section, we will investigate in abstract the theoretical causes of avoided crossings, the quantum mechanical phenomenon that makes Landau-Zener transitions possible. Following the example of Rubbmark, et al. [25], we imagine a system with two states, $|1\rangle$ and $|2\rangle$, whose energies are dependent on a common parameter q and degenerate at a certain q_c, as shown in Fig.

2.1(a). We define the unperturbed Hamiltonian $H_0(q)$ such that

$$H_0(q)|n\rangle = E_n^0(q)|n\rangle. \tag{2.1}$$

An avoided crossing arises because a perturbation disturbs the degeneracy of the system, so we define the total Hamiltonian as

$$H(q) = H_0(q) + H', \tag{2.2}$$

where the perturbation H' is assumed to be independent of q. This results in the two states having energies

$$E_n(q) = E_n^0(q) + \langle n|H'|n\rangle. \tag{2.3}$$

Next, we can construct a matrix representation of the Hamiltonian with elements $W_{ij} = \langle i|H|j\rangle$, finding

$$H(q) = \begin{pmatrix} \langle 1|H_0|1\rangle + \langle 1|H'|1\rangle & \langle 1|H_0|2\rangle + \langle 1|H'|2\rangle \\ \langle 2|H_0|1\rangle + \langle 2|H'|1\rangle & \langle 2|H_0|2\rangle + \langle 2|H'|2\rangle \end{pmatrix}. \tag{2.4}$$

Since $|1\rangle$ and $|2\rangle$ are eigenstates of the unperturbed Hamiltonian, the terms $\langle 1|H_0|2\rangle$ and $\langle 2|H_0|1\rangle$ are equal to zero. We define the quantity

$$E_0 \equiv 2\langle 1|H'|2\rangle, \tag{2.5}$$

which is constant because H' is independent of q. Making these simplifications and substituting in Eq. 2.3, the Hamiltonian becomes

$$H(q) = \begin{pmatrix} E_1(q) & \frac{1}{2}E_0 \\ \frac{1}{2}E_0 & E_2(q) \end{pmatrix}. \tag{2.6}$$

According to degenerate perturbation theory, the perturbed energy levels are given by

$$E_\pm = \frac{1}{2}\left(H_{11} + H_{22} \pm \sqrt{(H_{11} - H_{22})^2 + 4|H_{12}|^2}\right). \tag{2.7}$$

Substituting in values from Eq. 2.6, Eq. 2.7 becomes

$$E_\pm = \frac{1}{2}\left(E_1 + E_2 \pm \sqrt{E(q)^2 + E_0^2}\right), \tag{2.8}$$

where we define $E(q) = E_1(q) - E_2(q)$ as the energy spacing between the two levels as a function of q. Observing that $E(q_c) = 0$ by definition (i.e. the energy splitting between states $|1\rangle$ and $|2\rangle$ is zero at the point of degeneracy), we can observe from Eq. 2.8 that E_0 represents the separation of the avoided crossing. We now define states $|a\rangle$ and $|b\rangle$, which are eigenstates of the total Hamiltonian with energies $E_a = E_+$ and $E_b = E_-$. The avoided crossing, with the perturbed and unperturbed states, is shown in Fig. 2.1(b).

We can now use $|a\rangle$ and $|b\rangle$ as our basis states to construct a time-varying system state $\Psi(t) = \alpha(t)|a\rangle + \beta(t)|b\rangle$. To simulate a sweep through the region of degeneracy, we let q vary from q_i to q_f over a time interval ranging from t_i to t_f. If the system starts in $|b\rangle$ (i.e. $\beta(t_i) = 1$), then the probability that the system undergoes a diabatic transition to $|a\rangle$ is given by

$$P_{b\to a} = |\alpha(t_f)|^2 = |\langle\Psi(t_f)|a\rangle|^2. \tag{2.9}$$

The system undergoing a diabatic transition from $|b\rangle$ to $|a\rangle$ is equivalent to it being swept from $|1\rangle$ to $|1'\rangle$. Conversely, the system remaining adiabatically in $|b\rangle$ is equivalent to it undergoing a transition from $|1\rangle$ to $|2'\rangle$, which is known as a Landau-Zener transition. Here, a primed state $|n'\rangle$ represents that state $|n\rangle$ for $q > q_c$. If E_1 and E_2 are linear in q and q is swept through the avoided crossing at a steady rate, then Eq. 2.9 can be solved [25] in the limit $t_i \to -\infty$, $t_f \to +\infty$ to find

$$P_{1\to 1'} = \mathrm{e}^{-2\pi\Gamma} \tag{2.10}$$

where Γ, the Landau-Zener parameter, is given by

$$\Gamma = \frac{|\langle 1|H'|2\rangle|^2}{\hbar(dE/dq)(dq/dt)}. \tag{2.11}$$

A comparison can be made here between the two-state Landau-Zener transition and Rabi oscillations. In this theoretical setting, Rabi oscillations typically occur when q is fixed at q_c and the system is in a sinusoidally time-dependent superposition of $|a\rangle$ and $|b\rangle$.

Notice that Eqs. 2.10 and 2.11 behave as they should in the limiting cases:

$$\lim_{dq/dt \to 0} P_{1 \to 1'} = 0, \tag{2.12}$$

$$\lim_{dq/dt \to \infty} P_{1 \to 1'} = 1.$$

In the case of an infinitely slow sweep ($dq/dt \to 0$), the system will adiabatically remain in $|b\rangle$ and entirely undergo a transition from $|1\rangle$ to $|2'\rangle$. In the case of an infinitely fast sweep ($dq/dt \to \infty$), the system will undergo a diabatic transition to $|a\rangle$ and proceed entirely from $|1\rangle$ to $|1'\rangle$. This result also makes intuitive sense, insofar as anything quantum mechanical can, because a parameter that passes infinitely quickly through some sort of resonance will not excite any transitions from $|1\rangle$ to $|2'\rangle$ but it is possible for a parameter that spends an infinite amount of time on resonance to cause the system to undergo the transition.

For a three-state system, this calculation is more complicated. Instead of two states, $|1\rangle$ and $|2\rangle$, whose energies are arbitrary linear functions of q, we have three states, $|+1\rangle$, $|0\rangle$, and $|-1\rangle$. For these states, $dE_{+1}/dq = +kq$, $dE_0/dq = 0$, and $dE_{-1}/dq = -kq$. Such a system, albeit using a different labeling convention ($|+1\rangle \to |1,-1\rangle$, $|0\rangle \to |1,0\rangle$, and $|-1\rangle \to |1,+1\rangle$) and energy parameter than we use in this abstract derivation, is shown in Fig. 2.2(a). If this system is initially entirely in $|+1\rangle$ and q is swept through the region of degeneracy, the final coefficients for the three states can be calculated numerically [41] and are given to better than 0.1% by

$$\begin{aligned} |c_{|+1\rangle}|^2 &= \mathrm{e}^{-2\pi\Gamma} \\ |c_{|0\rangle}|^2 &= 2\mathrm{e}^{-\pi\Gamma}(1-\mathrm{e}^{-\pi\Gamma}) \\ |c_{|-1\rangle}|^2 &= (1-\mathrm{e}^{-\pi\Gamma})^2. \end{aligned} \tag{2.13}$$

This expression is valid as long as q is swept completely through the region of degeneracy, which can be characterized by q_0, the width of the avoided crossing. This characteristic width is defined as

$$q_0 = \frac{E_0}{(dE/dq)_{q_c}} \tag{2.14}$$

or, again assuming that all unperturbed energies are linearly dependent on or independent of q, q_0 can be defined more simply by

$$E(q_c \pm q_0) = \pm E_0. \tag{2.15}$$

Because Eqs. 2.10 and 2.13 are given in terms of the dimensionless and abstract parameter Γ, this description of the dynamical behavior of the abstract two- and three-state systems holds for any physical system whose energy states are linearly dependent on some parameter and degenerate at a specific value of that parameter.

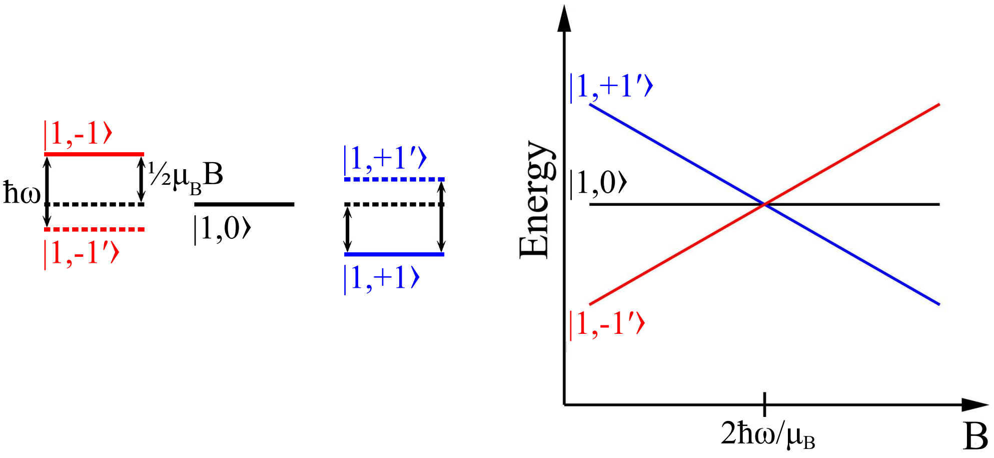

(a) (b)

Figure 2.2: Diagrams of a three-level Landau-Zener system in the $F = 1$ hyperfine manifold. Part (a) shows the $F = 1$ hyperfine manifold, with Zeeman splitting of magnitude $\frac{1}{2}\mu_B B$. The dressed states $|1, -1'\rangle$ and $|1, +1'\rangle$ are coupled to $|1, -1\rangle$ and $|1, +1\rangle$ respectively by the stimulated emission and absorption of a photon of angular frequency ω. As we hold ω constant and vary B, the energies of the two dressed states and the $|1, 0\rangle$ state vary as shown in part (b). These three states are degenerate at $2\hbar\omega/\mu_B$ and so constitute a three-state Landau-Zener system. As discussed in the text, this degeneracy gives rise to avoided crossings that can be traversed by Landau-Zener sweeps.

2.1.2 Landau-Zener Theory in ^{87}Rb

Now let us apply this Landau-Zener theory to our physical system of interest, the $F = 1$ hyperfine manifold of the ground state of ^{87}Rb. First, we will model the two-state system of $|1, -1\rangle$ and $|1, +1\rangle$ and then generalize to the complete three-state system. The unperturbed Hamiltonian is that which gives rise to linear Zeeman splitting. We choose to set our zero energy where the two states are degenerate at $B = 0$, so the unperturbed Hamiltonian is given by

$$H_0|1, \pm 1\rangle = \mp\frac{1}{2}\mu_B B|1, \pm 1\rangle, \tag{2.16}$$

where the magnetic field B takes the place of the general parameter q.

The system is perturbed by its interaction with incident radiation of frequency ω. For $|1, -1\rangle$, we consider the dressed state $|1, -1'\rangle$ created by the stimulated emission of a photon, so the expectation value of the perturbation is

$$\langle 1, -1|H'|1, -1\rangle = -\hbar\omega. \tag{2.17}$$

For $|1, +1\rangle$, however, we consider the dressed state $|1, +1'\rangle$ created by the absorption of a photon, so the expectation value of the perturbation is

$$\langle 1, +1|H'|1, +1\rangle = +\hbar\omega. \tag{2.18}$$

These dressed states and the relevant energy spacings are shown in Fig. 2.2(a). For the present discussion of the two-state system, we simply ignore the $|1, 0\rangle$ state. For this perturbation, the coupling matrix element of the Hamiltonian is given by

$$\langle 1, -1|H'|1, +1\rangle = \frac{\hbar\Omega}{\sqrt{2}}, \tag{2.19}$$

where Ω is the Rabi frequency of the stimulated transition [41].

Knowing these values, we can simply plug them into expressions that we read off from the abstract derivation. The total Hamiltonian in matrix form becomes

$$H(q) = \begin{pmatrix} \frac{1}{2}\mu_B B - \hbar\omega & \hbar\Omega/\sqrt{2} \\ \hbar\Omega/\sqrt{2} & -\frac{1}{2}\mu_B B + \hbar\omega \end{pmatrix}. \tag{2.20}$$

From this expression, we see that field-dependent splitting of the two dressed states is given by

$$E(B) = \mu_B B - 2\hbar\omega, \tag{2.21}$$

and thus the field strength at which the unperturbed states are degenerate is

$$B_c = \frac{2\hbar\omega}{\mu_B}. \tag{2.22}$$

From Eq. 2.4, we see that the energies of the perturbed states are given by

$$E_\pm = \pm\frac{1}{2}\sqrt{(\mu_B B - 2\hbar\omega)^2 + 2(\hbar\Omega)^2}, \tag{2.23}$$

from which we can determine the avoided crossing separation

$$E_0 = \sqrt{2}\hbar\Omega, \tag{2.24}$$

and the avoided crossing width

$$q_0 = \frac{\sqrt{2}\hbar\Omega}{\mu_B}. \tag{2.25}$$

The dynamical behavior of the system as B is swept through resonance also can be applied easily to the system of ^{87}Rb. Equation 2.10, with a change of indices, correctly represents the results of sweeping the two-state system through resonance. More interesting, though, is the extension of Landau-Zener theory to the three-state system, which is a more accurate model of the $F = 1$ hyperfine manifold. By introducing the $|1, 0\rangle$ level, the energy of which is independent of B, we create the three-level system shown in Fig. 2.2(b).

If the system is entirely in the $|1, -1\rangle$ state prior to the Landau-Zener sweep, as it would have to be in order to Bose-Einstein condense in the $F = 1$ hyperfine manifold, then the proportions of the populations after the sweep are given by

$$\begin{aligned} |c_{|1,-1\rangle}|^2 &= \mathrm{e}^{-2\pi\Gamma} \\ |c_{|1,0\rangle}|^2 &= 2\mathrm{e}^{-\pi\Gamma}(1 - \mathrm{e}^{-\pi\Gamma}) \\ |c_{|1,+1\rangle}|^2 &= (1 - \mathrm{e}^{-\pi\Gamma})^2. \end{aligned} \tag{2.26}$$

These equations are simply a recopying of Eq. 2.13 with different indices, but they are worth repeating. The majority of our experimentation on Landau-Zener transitions consists of trying to take data that can be fitted to these functions, which are plotted in Fig. 2.3.

As mentioned before, extending equations such as these that are parameterized by the Landau-Zener parameter Γ to diverse physical systems requires only a recasting of Γ. From the definition of Γ (Eq. 2.11) and the value of

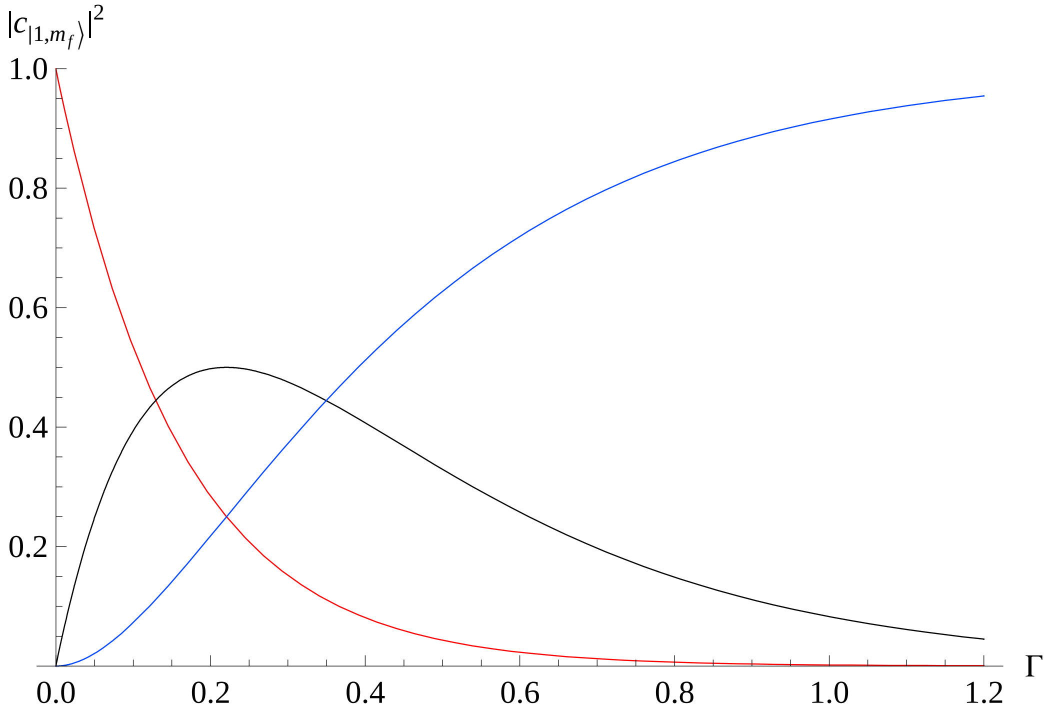

Figure 2.3: The theoretical relative populations of the three $F = 1$ states after a Landau-Zener sweep, as functions of the abstract Landau-Zener parameter Γ. The $|1, +1\rangle$ state is plotted in blue, $|1, 0\rangle$ in black, and $|1, -1\rangle$ in red. Each point represents atoms prepared in the $|1, -1\rangle$ state and then subjected to a Landau-Zener sweep characterized by a specific value of Γ.

the coupling matrix element for this particular system (Eq. 2.19), we find

$$\Gamma = \frac{\hbar\Omega^2}{2(dE/dB)(dB/dt)}. \tag{2.27}$$

Taking dE/dB from Eq. 2.21 and rearranging slightly, we find

$$\Gamma = \frac{\Omega^2}{4\pi\beta(dB/dt)}, \tag{2.28}$$

where $\beta \equiv \mu_B/h = 0.70$ MHz/G is the constant we calculated in Chapter 1 that relates the magnitude of the magnetic field to the Zeeman energy spacing, given in terms of frequency, that it produces. This fact leads one to recast Eq. 2.28 as

$$\Gamma = \frac{\Omega^2}{4\pi(d\nu/dt)}, \tag{2.29}$$

where ν is the frequency of the incident radiation.

Physically, Eq. 2.28 corresponds to holding the frequency of the incident radiation fixed and sweeping the magnetic field strength through resonance, while Eq. 2.29 corresponds to holding the field fixed and sweeping the radiation frequency through resonance. Essentially, instead of sweeping the radiation frequency through resonance, we sweep the resonance through the radiation frequency. These two approaches are equivalent insofar as the Zeeman splitting is linear with respect to the field strength, an approximation that we have already shown to be true to better than 0.4%. We have extensively studied both of these methods of conducting a Landau-Zener sweep and both are vital to our ongoing experimentation.

2.2 Landau-Zener Sweeps

2.2.1 Magnetic Field Sweep

Landau-Zener transitions have been used in past experiments [4] as a means to prepare a condensate to study Feshbach resonance, but characterization of the transitions had not been an end in itself prior to this thesis. For reasons that will be explained at the end of this section, a magnetic field sweep emerged as the most convenient method of performing Landau-Zener transitions to prepare atoms for Feshbach studies.

To express Γ in terms of experimental parameters, we can make the derivative in Eq. 2.28 discrete and recast it as

$$\Gamma = \frac{\Omega^2}{4\pi\beta\Delta B}\Delta t, \tag{2.30}$$

where ΔB is the range over which the field is swept and Δt is the ramp time.

Equation A.12 implies that the Rabi frequency Ω is proportional to the magnitude of the radiative electric field, and thus also to the magnitude of the radiative magnetic field. Experimentally, the latter magnitude is set by the RF power P_{RF}, in units of dBm. Therefore, we find

$$|E|^2 \propto 10^{P_{\mathrm{RF}}[\mathrm{dBm}]/10} \tag{2.31}$$

and we can express the Rabi frequency as

$$\Omega = \Omega_0 10^{P_{\mathrm{RF}}[\mathrm{dBm}]/20}, \tag{2.32}$$

where the proportionality in Eq. 2.31 and the other factors in Eq. A.12 are both rolled into the experimental constant Ω_0. Finally, we can express the Landau-Zener parameter purely in terms of experimental parameters:

$$\Gamma = \frac{\Omega_0^2 10^{P_{\mathrm{RF}}[\mathrm{dBm}]/10}}{4\pi\beta\Delta B}\Delta t. \tag{2.33}$$

Thus, the population distribution functions (Eq. 2.26) become functions of the sweep time Δt that are scaled by the RF power P_{RF}.

In our apparatus, Landau-Zener sweeps are performed using three coils. We run steady parallel current through the quadrupole coils, shown in Fig. 1.3, to create a uniform and precisely controllable vertical magnetic field and sinusoidal current through the horizontal RF coil to produce an oscillating horizontal magnetic field. The vertical field defines the atoms' magnetic quantization axis and the horizontal oscillating field, being perpendicular to the axis, drives the necessary σ-transitions between the magnetic sublevels.

We have been describing non-degenerate energy states as being coupled by electromagnetic radiation but they are coupled by a driven oscillating magnetic field in this case. Since the two types of magnetic fields are effectively equivalent for the purposes of Landau-Zener transitions, the term "radiation" will be understood to represent the oscillating magnetic field throughout this chapter.

Experimentally, the Landau-Zener procedure is fairly straightforward. As described in Section 1.4.3, after the condensate has been transferred into the optical trap and the rotating magnetic field has been disabled, the atoms are in a 10.0 G vertical field. The RF radiation is enabled with a frequency of 4.0 MHz and a power of P_{RF} and allowed to stabilize for 1.0 ms. Then, the field is ramped from 10.0 G to 1.5 G over a given ramp time and the radiation is disabled immediately thereafter.

To test the reliability of this Landau-Zener transition method, we plot the relative proportions of the three populations after a Landau-Zener sweep. Plotted as a function of the ramp time, these data should resemble Fig. 2.3. Our data, however, are messy to the point at which their resemblance to the theoretical functions is only vaguely recognizable. Figure 2.4 compares the clearest set of data collected using the field sweep method with a set collected using the frequency sweep method. The most obvious difference between the two sets is the amount of noise. While the second data set can be fit closely to theory, the data of the first can only be seen to follow the correct general trends; the proportion of $|1,-1\rangle$ atoms decreases to zero, the proportion of $|1,0\rangle$ atoms peaks, and the proportion of $|1,+1\rangle$ atoms approaches one in the same portion of the plot.

We believe that this unreliability is caused by a combination of instability in the magnetic field and discontinuities in the field ramp. Although the electronics and current sources that control the coils are stable, we cannot

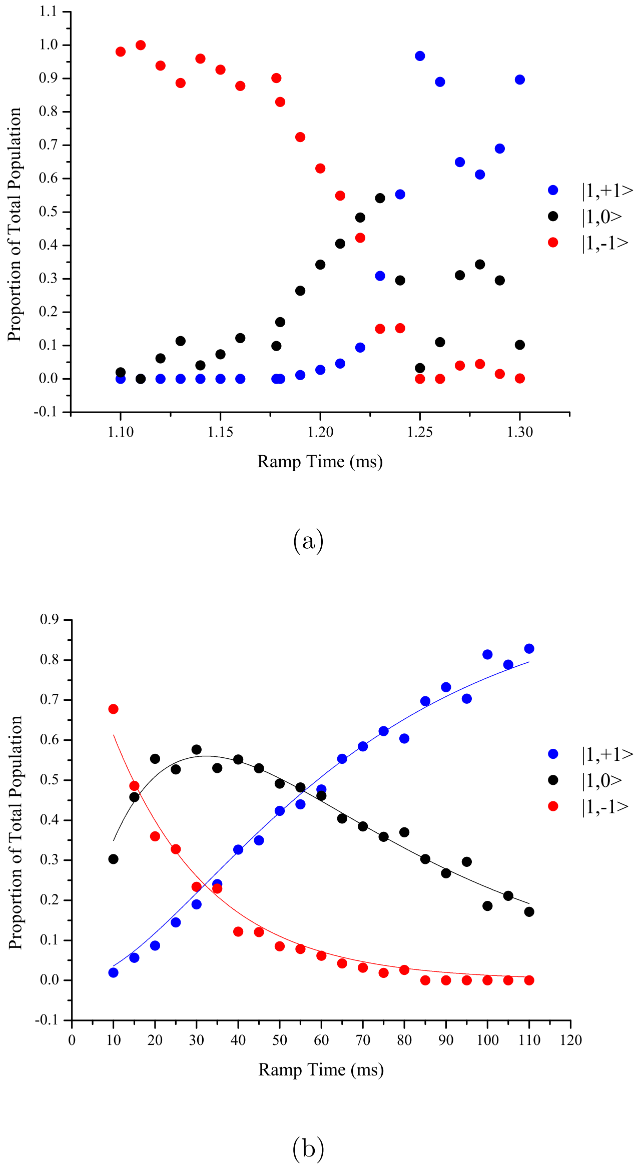

Figure 2.4: Relative populations of $F = 1$ atoms after a Landau-Zener (a) magnetic field sweep or (b) radiation frequency sweep, as functions of the ramp time Δt. Notice that the field sweep method produces far messier data that only vaguely follow the correct trends, which the data produced by the frequency sweep method adhere well to the theoretical fit shown. The different time scales are explained by the fact that $P_{\mathrm{RF}} = -13$ dBm for the data in part (a) and $P_{\mathrm{RF}} = -27$ dBm for the data in part (b).

easily control for shifting ambient magnetic fields. Stray currents in the lab can be produced by any number of sources, such as our electronic equipment or the 2 T fields created in the lab next door, and have been observed to drift 0.3 mG overnight. Magnetization is hysteretic, so if an external magnetic field magnetizes some part of the apparatus, then a trace of this external field remains even after the field itself has been removed. Also, the changing magnetic field magnitude induces eddy currents in the metal structure of the trap, which themselves create secondary magnetic fields.

Perhaps the more significant factor is the discontinuous nature of the magnetic field ramp. The field strength is proportional to a precise analog voltage put out by the computer controller. The computer cannot vary this voltage smoothly but must increment it up or down in a series of discrete steps. There is a time constant associated with each sudden field change, so the time-dependence of the magnetic field actually resembles a series of steep exponential decays, as depicted qualitatively in Fig. 2.5. The ramp approximates a smooth sweep as the step intervals become increasingly small, but the actual instantaneous time derivative of the field strength is rarely equal to the average sweep rate. This discrepancy is critical for this specific experiment because our experimental definition of the Landau-Zener parameter Γ (Eq. 2.33) is predicated on the assumption of a constant sweep rate. This assumption is implicitly made by changing the dB/dt of Eq. 2.28 into the $\Delta B/\Delta t$ of Eq. 2.30.

Also, the portion of the magnetic field sweep data that resembles the

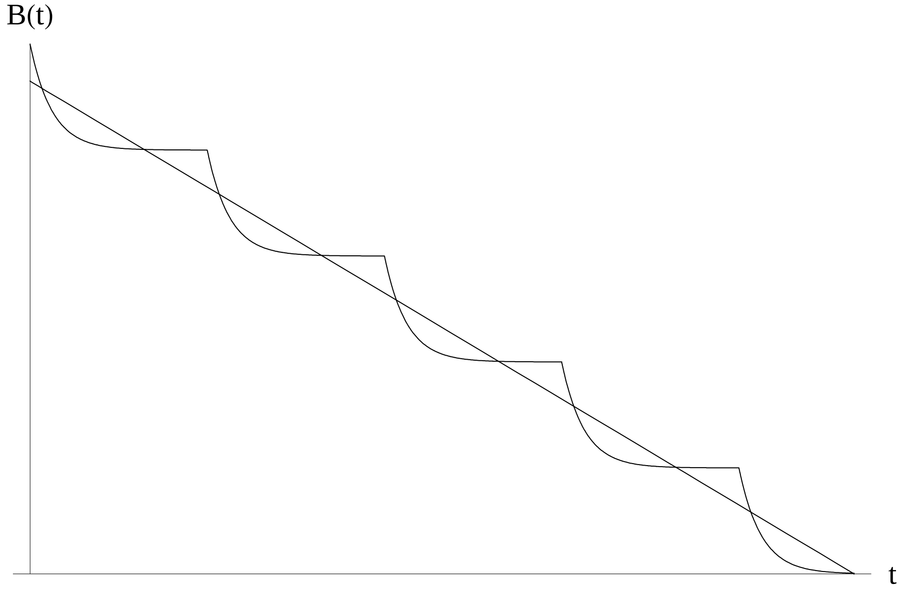

Figure 2.5: A qualitative illustration of the discontinuous nature of the magnetic field ramp versus the linear ramp approximation. Our magnetic field magnitude cannot be ramped continuously but must be increased or decreased in a series of discrete steps. There is a time constant associate with the response of the control equipment and current source to each discontinuous step, so the ramp is actually composed of a series of steep exponential decays. The approximation of a linear ramp becomes increasingly accurate as the step size decreases.

theoretical population distributions begins around $\Delta t = 1.17$ ms and not $\Delta t = 0$ ms, as would be expected. Other data sets are similarly inconsistent with theory for ramp times of less than approximately 1 ms. This offset hints at a slight delay in some portion of the mechanism that supplies current to the coils, although this, too, could be a result of the discontinuous nature of the sweep.

Noticing that the ramp times in the frequency sweep data set are approximately a factor of 200 greater than those in the field sweep set, one might wonder whether reducing P_{RF} and extending the ramp times might mitigate the aforementioned effects and produce cleaner data. We are still, however, limited by the step size and response time. Upon attempting to lengthen the ramp time, we encountered a pathology that is even more pronounced and less understood than those already mentioned. Because this pathology was observed while studying Landau-Zener transitions and is not well understood, it will be referred to as the field sweep pathology. For certain values of the ramp time, the Landau-Zener sweep fails to transfer any atoms to the $|1, 0\rangle$ or $|1, +1\rangle$ states. For the ramp times shown in Fig. 2.6, all of the atoms should be in the $|1, +1\rangle$ state but an increasing number are not being transferred. In this case, the transition from the "normal" regime, in which all atoms are in the $|1, +1\rangle$ state, to the "pathological" regime, in which all atoms are in the $|1, -1\rangle$ state, is gradual. In fact, if one reverses the order of the four images in Fig. 2.6 and makes Δt start at 0 ms instead of 3.9 ms, the resulting transfer pattern would be almost exactly what we expect.

This observation by itself suggests the possibility that atoms are being transferred over to the $|1, 0\rangle$ and $|1, +1\rangle$ states and subsequently transferred back, a rough analog of Rabi oscillation for a three-state system.

In other instances, however, the transition has been more abrupt. Figure 2.7 shows data taken during an exploration of this pathology conducted on a different day. Notice first that these values of Δt are approximately 1.5 ms larger than those in Fig. 2.6, which indicates a drift in the system, and second that the interval between them is two orders of magnitude smaller. The proportions of the three populations shift as much in Fig. 2.7 with a difference in Δt of 2 μs as they do in Fig. 2.6 with a difference of 100 μs or in Fig. 2.4(a) with a difference of approximately 40 μs. In this particular exploration, the range of Δt over which the Landau-Zener transfer was observed to fail completely extended from around 5.7 ms to 7.0 ms, although these limits drifted minutely from shot to shot.

We have found a pathology that disables Landau-Zener transitions over a sharply defined and finite yet variable range of ramp times. This effect, together with the noisiness and offset of the data mentioned before, suggests some combination of drift in the ambient magnetic field, some sort of resonance involving the sweeping magnetic field, or subtle technological pathologies. Further understanding of any of these three sources of unreliability would provide a motivation for a more thorough investigation of the field sweep Landau-Zener method.

Despite this method's inability to produce precise population distribu-

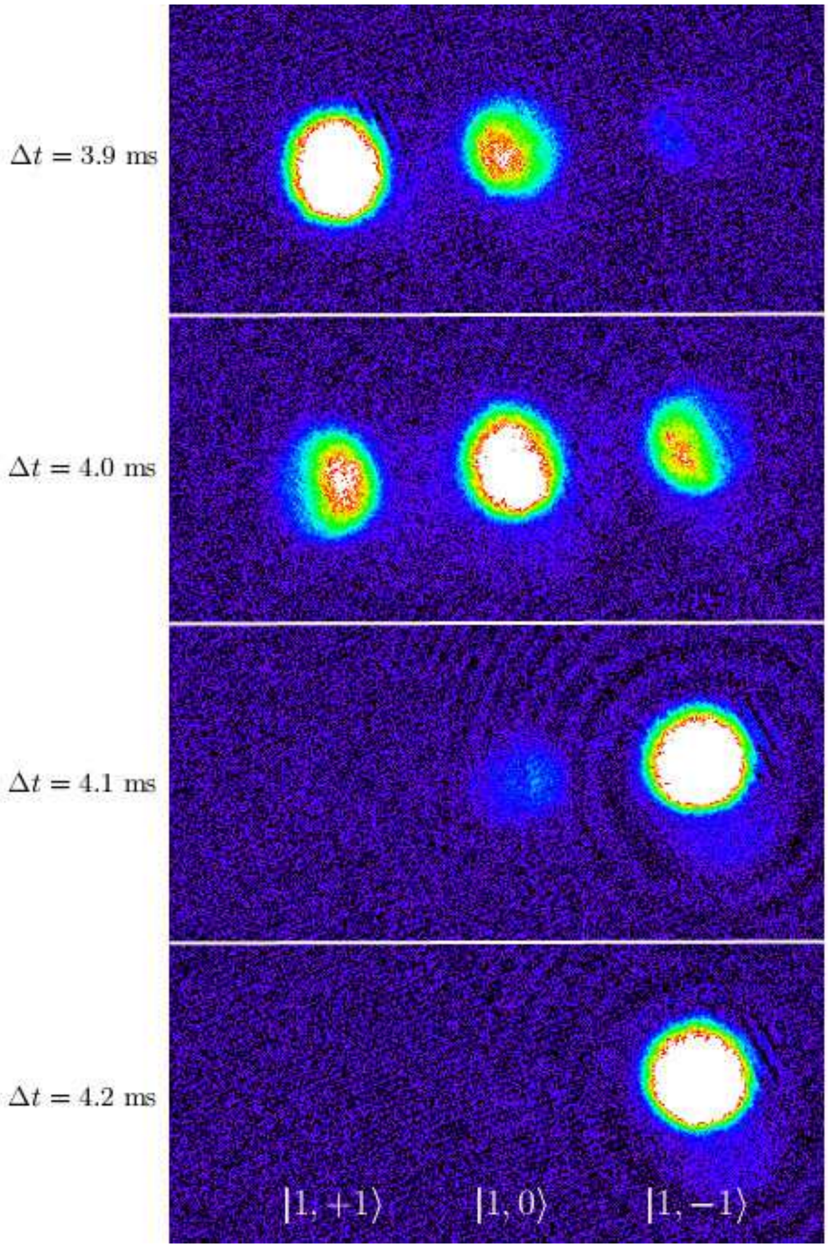

Figure 2.6: Gradual onset of the field sweep pathology. A Landau-Zener field sweep slowly begins to fail to transfer atoms out of the $|1, -1\rangle$ state. Notice that the time scale for the onset of the pathology here is an order of magnitude smaller than for the data shown in Fig. 2.7.

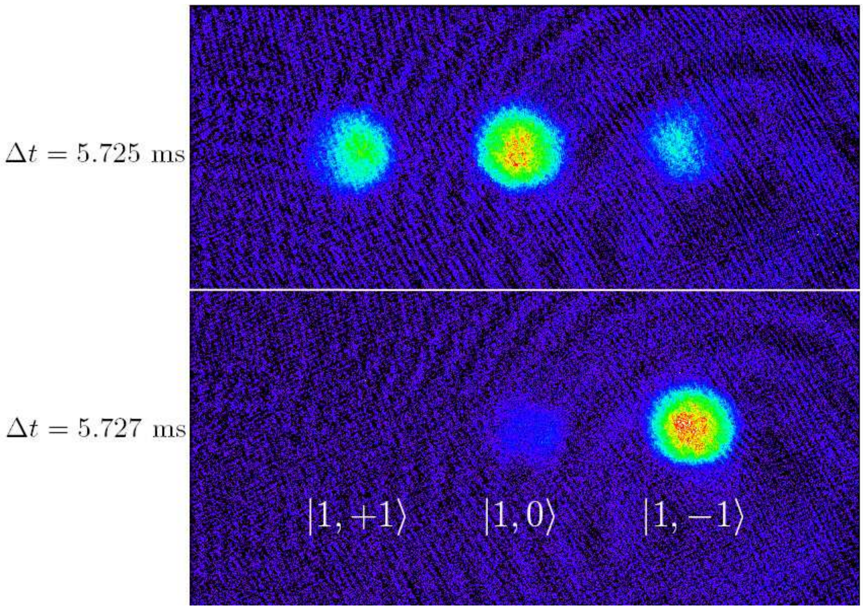

Figure 2.7: Sudden onset of the field sweep pathology. A Landau-Zener field sweep quickly begins to fail to transfer atoms out of the $|1,-1\rangle$ state. Note that the difference in Δt between partial and almost non-existent transfer is only 2 μs, an order of magnitude smaller than the similar intervals in Fig. 2.6 or 2.4(a).

tions, it can transfer the entire population to the $|1,+1\rangle$ state with great reliability. As we can see in Fig. 2.3 and Eq. 2.26, $|c_{|1,-1\rangle}|^2$ and $|c_{|1,0\rangle}|^2$ asymptote to zero and $|c_{|1,+1\rangle}|^2$ asymptotes to one at high values of Γ. Therefore, if the sweep time is made sufficiently long, the proportion of atoms transferred to the $|1,+1\rangle$ state will be highly insensitive to the field fluctuations and sweep discontinuities that have plagued our attempts to plot population distribution curves with this method.

For this purpose, we use a sweep time of 25.0 ms with $P_{\mathrm{RF}} = -13.0$ dBm, which corresponds to a suitably large value of $\Gamma = 28$. Using these parameters, the field sweep method transfers the entire population to the $|1,+1\rangle$ state as reliably as the generally more precise frequency sweep method. This makes the field sweep method suitable for preparing a mixture of $|1,+1\rangle$ and $|2,-1\rangle$ states for studies of the interspecies Feshbach resonance. This is particularly convenient because the function generator used to sweep the radiation frequency is also used to create the RF half of the two-photon pulse. By using the field sweep method instead of the frequency sweep method, we save the time necessary to reprogram the function generator and so we can move swiftly from the Landau-Zener sweep to the two-photon transition when preparing for Feshbach studies.

2.2.2 Radiation Frequency Sweep

Because the pronounced instability and pathologies inherent in the field-sweep method are believed to be a result of the discontinuous nature of the field ramp, we turned to keeping the magnetic field strength constant and sweeping the frequency of the RF radiation. This is the method that the Ketterle group used to make the first spinor Bose-Einstein condensate and in later experiments [37, 41]. We use a Hewlett-Packard 3325A function generator to produce a phase-continuous frequency ramp that is amplified to produce the oscillating magnetic field. The function generator has a frequency resolution of 1 mHz, which is nine orders of magnitude smaller than the sweep range. Since the ramp is phase-continuous and consists of such small frequency steps, the frequency of the radiation changes relatively smoothly and the problems associated with the discontinuity of discrete steps are reduced.

Another advantage of this method is its insensitivity to variations in the magnetic field. The Landau-Zener parameter, now recast from Eq. 2.29 as

$$\Gamma = \frac{\Omega_0^2 10^{P_{\mathrm{RF}}[\mathrm{dBm}]/10}}{4\pi\Delta\nu}\Delta t, \tag{2.34}$$

is dependent only on the rate at which the RF frequency is swept through resonance and not on the specific value, given either in terms of frequency or field strength, at which resonance occurs. One requires only that the resonant frequency corresponding to the field strength, given by Eq. 1.16, be well within the frequency range that is swept. For our experimental parameters, this corresponds to an acceptable field strength range of 0.7 G to 29.3 G, which is far wider than the range of any possible drift.

The procedure for the Landau-Zener frequency sweep is straightforward and analogous to the procedure for the field sweep. As with the field sweep method, we use the horizontal RF coil to supply the oscillating magnetic field and the vertical quadrupole coils in the Helmholtz configuration to supply the static field. First, the magnetic field is ramped to 1.0 G and the RF coil is activated at zero power (-70 dBm) and 500 kHz. After the system is allowed to stabilize for 3.0 ms, the power driven through the RF coil is ramped up to P_{RF} to prepare for the sweep. It is necessary to activate the RF radiation smoothly in this way because enabling the coil while current is being driven at full power produces transient radiation at a range of frequencies that causes unintentional transitions between the three $F = 1$ states. The field sweep method, however, was not found to be affected by this problem and so would not be improved by ramping on the radiation in this way. The driving frequency is then swept smoothly from 500 kHz to 20.5 MHz over the ramp time Δt, which is, as with the field sweep, the independent parameter for data collection. Finally, the RF power is ramped back to zero and the coil is disabled.

Because of the technical limitations of the HP3325A, we are constrained by a minimum sweep time of 10 ms and a maximum output frequency of 21.0 MHz, resulting in a maximum sweep rate of 2.1 GHz/s. So that our observable range of Δt begins with most of the atoms still in the $|1, -1\rangle$ state, we lower P_{RF} to roughly -30 dBm. The proportional populations of $|1, -1\rangle$, $|1, 0\rangle$, and $|1, +1\rangle$ atoms are shown in Fig. 2.8 as functions of the

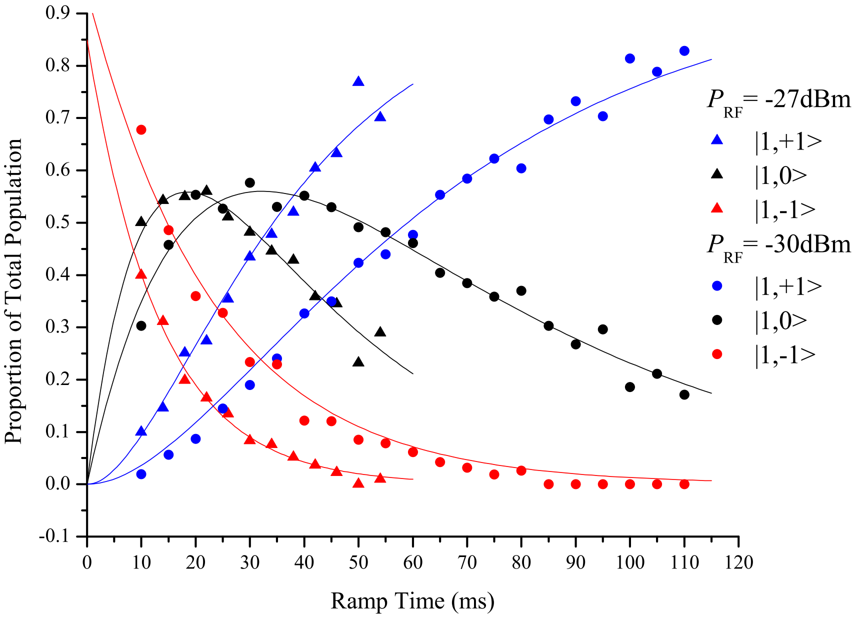

Figure 2.8: Results of Landau-Zener frequency sweeps performed at two values of P_{RF}. As per Eqs. 2.32 and 2.34, decreasing P_{RF} decreases the Rabi frequency for transitions between the magnetic sublevels and consequently scales the population distribution functions outward towards longer ramp times.

ramp time Δt for two values of P_{RF}.

As we can see in Figs. 2.4(b) and 2.8, sweeping the RF radiation frequency instead of the magnetic field magnitude produces far cleaner data that are consistent with theoretical predictions. For each plot, the theoretical fits share a common horizontal scaling parameter, equal to $\Omega^2/4\Delta\nu$, but the vertical scaling parameters are allowed to vary individually to take into account the different imaging efficiencies of the three magnetic states.

This allows us to calculate a Rabi frequency from each set of data, the results of which are plotted in Fig. 2.9. As expected, the Rabi frequency of the transition between adjacent magnetic states is roughly proportional to $10^{P_{\mathrm{RF}}[\mathrm{dBm}]/20}$, as per Eq. 2.32, and the three runs conducted with $P_{\mathrm{RF}} = -30$ dBm result in values that are well within uncertainty of each other.

We have two complementary methods of conducting a Landau-Zener sweep. The magnetic field sweep method, while riddled with pathologies in the short ramp time regime that we study to characterize the Landau-Zener process, very reliably transfers the entire population of atoms to the $|1, +1\rangle$ state. This reliable performance makes a field sweep the convenient choice for preparing a condensate for studies of the $|1, +1\rangle \otimes |2, -1\rangle$ interspecies Feshbach resonance. The frequency sweep method, on the other hand, produces reliable population distributions at any allowed value of the ramp time, making it ideal for producing balanced population distributions, in which the $|1, -1\rangle$ and $|1, +1\rangle$ populations are equal. This reliable performance makes a frequency sweep the default choice for preparing a spinor condensate with approximately equal components.

2.3 Stern-Gerlach Separation

Our absorptive imaging technique only measures the density distribution of the atoms within the condensate and provides no data on their magnetic quantum states. In order to observe the atoms in the $|1, -1\rangle$, $|1, 0\rangle$, and

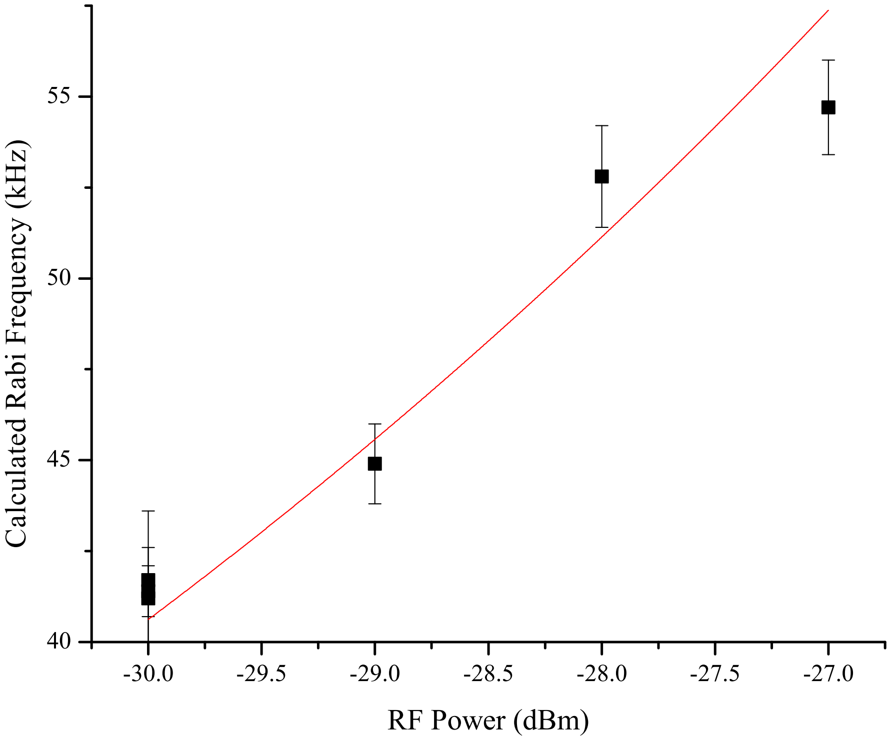

Figure 2.9: Rabi frequency of transitions between magnetic sublevels as a function of RF power, with a theoretical fit to $\Omega = \Omega_0 10^{(P_{\mathrm{RF}}[\mathrm{dBm}]-P_0)/20}$ (Eq. 2.32 with an offset in the independent variable P_{RF}). These data were collected by analyzing the theoretical fits to several sets of Landau-Zener sweep data, such as the set shown in Fig. 2.4(b). Note that the three data points for $P_{\mathrm{RF}} = -30$ dBm are well within uncertainty of each other and the data roughly follow the theoretical trend.

$|1,+1\rangle$ states distinctly, we must spatially separate the three populations. To do this, we employ the technique first used by Otto Stern and Walther Gerlach in 1922 to separate electrons on the basis of their magnetic moments [42]. We apply an inhomogeneous magnetic field to the condensate as it falls prior to imaging, which separates the three populations along an arbitrary magnetic quantization axis. This technique can also be modified slightly to detect any stray magnetic field gradients in the trap. To do this, we simply provide a uniform bias field and allow the stay field gradients to exert forces on the condensate components.

2.3.1 Derivation of Forces

In general, the force on a magnetic dipole in an inhomogeneous magnetic field is given by

$$\mathbf{F} = \nabla(\boldsymbol{\mu} \cdot \mathbf{B}). \tag{2.35}$$

For an atom in a magnetic field $\mathbf{B}_0 = B_0\hat{\mathbf{z}}$, the projection of its magnetic moment along the magnetic quantization axis $\hat{\mathbf{z}}$ is given by

$$\mu_z = -g_F m_F \mu_B, \tag{2.36}$$

where g_F is the Landé g-factor, m_F is the magnetic quantum number, and μ_B is the Bohr magneton. Therefore, the force exerted on a ^{87}Rb atom in the $F = 1$ hyperfine manifold, for which $g_F = -1/2$, is

$$\mathbf{F} = \frac{1}{2} m_F \mu_B (\hat{\mathbf{B}}_0 \cdot \nabla \mathbf{B}). \tag{2.37}$$

Note that for an atom in a given location, the magnetic field is spacially variant but the direction of the atom's magnetic moment is not. It is because of the inclusion of m_F here that this force discriminates between the $|1, -1\rangle$, $|1, 0\rangle$, and $|1, +1\rangle$ states.

In our apparatus, the field gradient is produced by running the vertical quadrupole coils in the anti-Helmholtz configuration. We assume that the magnetic field gradients produced by these coils are sufficiently strong so that stray field gradients in the trap may be neglected. The arbitrary bias field is created by three pairs of bias coils, one with its axis along each axis of the lab reference frame. For reference, all of these coils are shown in Fig. 1.3. We assume that this bias field is homogeneous over our region of interest. The condensates are pushed approximately 100 μm horizontally from the center of the trap by Stern-Gerlach forces and fall roughly 2 mm before they are imaged, so the dimensions of the area in which the condensate can be found are two and three orders of magnitude smaller than the radii of the bias coils.

Because of the cylindrical symmetry of this configuration, we define a cylindrical-polar coordinate system coaxial with the anti-Helmholtz pair of coils and with its origin at the pair's center. To make this reference frame consistent with the lab reference frame, shown in Fig. 1.3, we define $+\hat{\mathbf{z}}$

as downward. In the anti-Helmholtz field, only $\partial B_\rho/\partial\rho$ and $\partial B_z/\partial z$ are non-zero. Therefore, Eq. 2.37 becomes

$$\mathbf{F} = \frac{1}{2} m_F \mu_B \left(B_{0\rho} \frac{\partial B_\rho}{\partial \rho} \hat{\boldsymbol{\rho}} + B_{0z} \frac{\partial B_z}{\partial z} \hat{\mathbf{z}} \right). \tag{2.38}$$

It must be noted that here B_{0x_i} is defined as $\frac{\mathbf{B}_0}{|\mathbf{B}_0|} \cdot \hat{\mathbf{x}}_i$ and not $\mathbf{B}_0 \cdot \hat{\mathbf{x}}_i$; the force on the atoms is dependent only on the direction of the bias field and not on its magnitude.

From the nonexistence of magnetic monopoles, we know

$$\nabla \cdot \mathbf{B} = \frac{1}{\rho} \frac{\partial}{\partial \rho} (\rho B_\rho) + \frac{1}{\rho} \frac{\partial B_\phi}{\partial \phi} + \frac{\partial B_z}{\partial z} = 0. \tag{2.39}$$

The azimuthal term is zero for the cylindrically symmetric configuration and the atoms remain sufficiently close to the common axis of the anti-Helmholtz coils so that the first-order approximation of $B_\rho = (\partial B_\rho/\partial\rho)\rho$ represents a calculated deviation of less than one part in 5×10^5 from the precise field value. Substituting this expression for B_ρ into Eq. 2.39, we find

$$2 \frac{\partial B_\rho}{\partial \rho} + \frac{\partial B_z}{\partial z} = 0. \tag{2.40}$$

Thus, Eq. 2.38 can be simplified to

$$\mathbf{F} = \frac{1}{2} m_F \mu_B \frac{\partial B_\rho}{\partial \rho} (B_{0\rho} \hat{\boldsymbol{\rho}} - 2 B_{0z} \hat{\mathbf{z}}). \tag{2.41}$$

For the purpose of imaging a multi-component condensate, we generally apply a bias field only in the $\hat{\boldsymbol{\rho}}$ direction, resulting in the simplification of Eq. 2.41 to an expression of horizontal force:

$$F_\rho = \frac{1}{2} m_F \mu_B \frac{\partial B_\rho}{\partial \rho}. \tag{2.42}$$

Imaging occurs, however, after the condensate has been released from the optical trap and has fallen through the center of the pair of anti-Helmholtz coils. The negative value of $\partial B_z/\partial z$ implies a negative z-component of the magnetic field below the center of the coils ($z > 0$), and thus a second-order component of the Stern-Gerlach force parallel to $m_F \hat{\mathbf{z}}$. As a result, the $|1, -1\rangle$ component of the condensate is imaged slightly above the $|1, 0\rangle$ component and the $|1, +1\rangle$ component is imaged slightly below.

2.3.2 Application to Stray Gradient Detection

We also use Stern-Gerlach separation to detect stray magnetic field gradients. To do this, we do not use the anti-Helmholtz coils to impose strong field gradients and we set the bias field along an axis of the lab reference frame so that $\hat{\mathbf{B}}_0 = \hat{\mathbf{x}}_i$. We are adopting the Einstein summation convention for the following analysis. Recasting Eq. 2.37 into Cartesian coordinates and using this choice of $\hat{\mathbf{B}}_0$, we find

$$\mathbf{F}_{\hat{\mathbf{B}}_0 = \hat{\mathbf{x}}_i} = \frac{1}{2} m_F \mu_B \frac{\partial B_i}{\partial x_j} \hat{\mathbf{x}}_j. \tag{2.43}$$

With three choices for both i and j, Eq. 2.43 implies nine gradients to be measured.

There are two constraints, however, that reduce the number of independent gradients to five. First, we can recast Eq. 2.39 into Cartesian coordinates to find

$$\nabla \cdot \mathbf{B} = \frac{\partial B_i}{\partial x_i} = 0, \tag{2.44}$$

which constrains the three divergence partial derivatives. Also, because there is zero current density at the center of the trap and we are neglecting the magnetic induction of time-dependent electric fields, we know

$$\nabla \times \mathbf{B} = \mu_0 \mathbf{J} + \mu_0 \epsilon_0 \frac{\partial \mathbf{E}}{\partial t} = 0, \tag{2.45}$$

and so

$$\frac{\partial B_i}{\partial x_j} = \frac{\partial B_j}{\partial x_i} \tag{2.46}$$

for all values of i and j. Therefore, using three iterations of Eq. 2.43 and Eqs. 2.44 and 2.46 as constraints, we arrive at five independent field gradients to be measured.

2.4 Stray Magnetic Field Gradients

2.4.1 Preliminary Detection

Understanding the stray magnetic field gradients in our apparatus is important because they exert asymmetric forces on the condensate that hamper our investigations of its time evolution in the trap. For example, Fig. A.2(a) shows that the center of the crossed-beam FORT is approximately cylindrically symmetric around a vertical axis. As mentioned before, this symmetry allows us to study the evolution of vertical vortices in a single condensate or in the components of a spinor condensate as they evolve in the optical trap. Stray field gradients, however, exert a force on the condensate that breaks this symmetry. This disturbance is especially severe for a spinor condensate, in which the gradient force is exerted on the $|1,-1\rangle$ and $|1,+1\rangle$ components in opposite directions.

For this reason, stray field gradients also hamper the observation of the evolution of a spinor condensate without vortices. Because these stray gradients are far weaker than the gradient we purposefully impose to separate the components for imaging, the forces they exert on the condensate are not sufficient to cause spatial separation. The condensates in different quantum states have different s-wave scattering lengths, though, which causes them to separate regardless of external discriminating forces. The gradient forces simply cause the components to separate asymmetrically. Previous work [33] has shown that a two-body condensate evolves in a complex pattern of interpenetrating rings, which are not observed if the symmetry of forces in the trap is broken by stray field gradients.

Fortunately, though, stray field gradients do not appear to significantly affect the time evolution of the two states used in our studies of the interspecies Feshbach resonance. As with the $|1, -1\rangle$ and $|2, +1\rangle$ states observed previously, the $|1, +1\rangle$ and $|2, -1\rangle$ states used in our Feshbach studies have identical projections of their magnetic moments along the magnetic quantization axis, given by Eq. 2.36. Therefore, the magnetic field gradients exert the same force on both components and do not significantly disturb how they spatially separate as they evolve.

We can use this asymmetric spatial separation and Eq. 2.43 to determine the sign and compare the magnitudes of stray field gradients in the trap. In Fig. 2.10(a), a bias field was applied in the $+\hat{\mathbf{y}}$ direction and the $|1, -1\rangle$ component was out-coupled preferentially. This result indicates that stray gradients exerted a force on that component in the $-\hat{\mathbf{z}}$ direction, which implies that $\partial B_y/\partial z = \partial B_z/\partial y < 0$. In Fig. 2.10(b), the $|1, -1\rangle$ and $|1, +1\rangle$ components display preferential spatial separation, indicating other non-zero stray field gradients. A bias field was also applied in the $+\hat{\mathbf{y}}$ direction in this case and the $|1, -1\rangle$ component separated in the $+\hat{\mathbf{x}}$ and $+\hat{\mathbf{y}}$ directions, indicating that $\partial B_y/\partial y < 0$ and $\partial B_x/\partial y = \partial B_y/\partial x < 0$.

To ensure that these separations are not due to the brief but large force applied by our applied quadrupole gradient to separate the components for imagining, we repeated this experiment a number of times, applying a bias

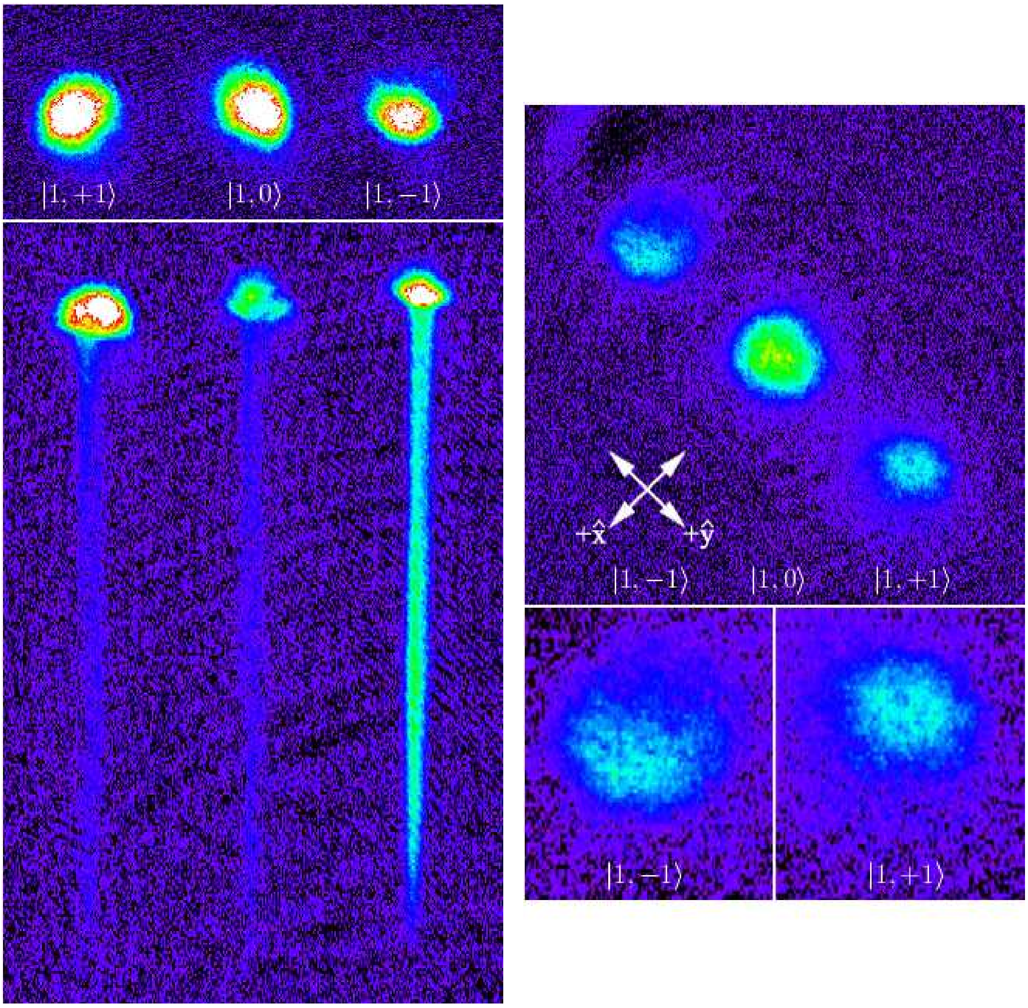

(a) (b)

Figure 2.10: Preliminary evidence of stray magnetic field gradients. Part (a) shows a spinor condensate, with and without atom lasing. Note the preferential out-coupling of the $|1, -1\rangle$ component, despite the other two components' larger initial populations. Part (b) shows a spinor condensate, imaged from below, that displays spatial separation of the $|1, -1\rangle$ and $|1, +1\rangle$ components. For clarity, magnified images of the two magnetically affected states are shown. In all cases, a bias field in the $+\hat{\mathbf{y}}$ direction was applied as the condensate was evolving or lasing.

field and separating for imaging along both the x- and y-axes. These data are imprecise due to the currently fairly subjective judgment of how the components of a condensate have separated out, but they are also generally consistent. Further experimental steps in this direction might include allowing the condensate to evolve for different lengths of time or somehow increasing the interatomic repulsion between the magnetically affected states to achieve a more clearly defined separation axis. Higbie et al. have measured field gradients to high precision by measuring Larmor precession in spinor condensates [43]. We could replicate this experiment once we have implemented phase-contrast imaging in order to gain a much clearer picture of the stray field gradients. We might also take measurements repeatedly on different days to determine how the stray field gradients drift over time. We have already mentioned that the stray field magnitude drifts over time, so its gradients should do so as well.

2.4.2 Proposed Nullification

A diagnosis of the stray gradient problem, however, is only useful insofar as it helps us to find a solution. The solution to minimizing the stray divergence gradients $\partial B_x/\partial x$, $\partial B_y/\partial y$, and $\partial B_z/\partial z$ is already largely in place. Using the quadrupole coils in the anti-Helmholtz configuration, we can exactly cancel one of these three arbitrary gradients. We might alternatively set the anti-Helmholtz current so as to minimize the sum of these three gradients but because the one pair of coils allows us only one degree of freedom, we cannot cancel all three exactly. Once the upgrade to the coil control circuits mentioned in Chapter 1, which will allow us to create superpositions of Helmholtz and anti-Helmholtz current in each pair of coils, is installed, we will be able to cancel all three arbitrary divergence gradients.

The pre-existing coils will not, however, help us to nullify stray mixed gradients. There are six mixed gradients but Eq. 2.46 reduces the number of independent gradients to three - $\partial B_x/\partial y$, $\partial B_y/\partial z$, and $\partial B_z/\partial x$. So as not to couple canceling of the divergence and mixed gradients, we want a current configuration that will have at its center all three of the divergence gradients and two of the independent mixed gradients equal to zero and one mixed gradient not equal to zero. With three of these configurations installed, the current run through each of them could be adjusted in order to precisely cancel all three stray mixed field gradients.

First, we assume that the ideal coil configuration will be some assembly of infinitely long straight wires carrying current parallel or anti-parallel to the z-axis. If the current configuration has no z-dependence, then the magnetic field will have no z-dependence or z-component, and so

$$\partial B_x/\partial z = \partial B_y/\partial z = \partial B_z/\partial z = 0. \tag{2.47}$$

Equation 2.44, the result of the non-existence of magnetic monopoles, equates the divergence gradients and now sets

$$\partial B_x/\partial x = -\partial B_y/\partial y. \tag{2.48}$$

Therefore, simply by making this assumption about the geometry of the configuration, we reduce the number of independent gradients to be calculated to two - $\partial B_x/\partial x$ and $\partial B_x/\partial y$.

Setting $\hat{\mathbf{I}} = \pm\hat{\mathbf{z}}$, we use the Biot-Savart law to find the current created at the center of the trap, defined as our origin, by an arbitrary array of n wires:

$$\mathbf{B} = \frac{\mu_0 I}{4\pi}\sum_{i=1}^{n}\left(\delta_i \int_{-\infty}^{+\infty} \frac{\hat{\mathbf{z}} \times \hat{\mathbf{r}}_i}{z^2 + r_i^2}\mathrm{d}z\right), \tag{2.49}$$

where $\mathbf{r}_i$ is the vector from the origin to the point at which the ith wire intersects the xy-plane and $\delta_i = \pm 1$ gives the direction of the current conducted by the ith wire. By using this formula and taking the appropriate derivatives, we find that the "simple cross" configuration shown in Fig. 2.11(a) satisfies our conditions $\partial B_x/\partial x = 0$ and $\partial B_x/\partial y \neq 0$. This configuration is not physically permissible, because placing bundles of wires in this configuration, which has two wires set at $\pm d$ on the x-axis carrying current $-I\hat{\mathbf{z}}$ and two wires set at $\pm d$ on the y-axis carrying current $+I\hat{\mathbf{z}}$, would physically interfere with the lasers incident on the cell from those directions.

Next, we try rotating this configuration by an angle θ, defining counterclockwise to be positive, from the axes, creating the "tilted cross" configuration shown in Fig. 2.11(b). This is a simple rotation of axes, so as we would

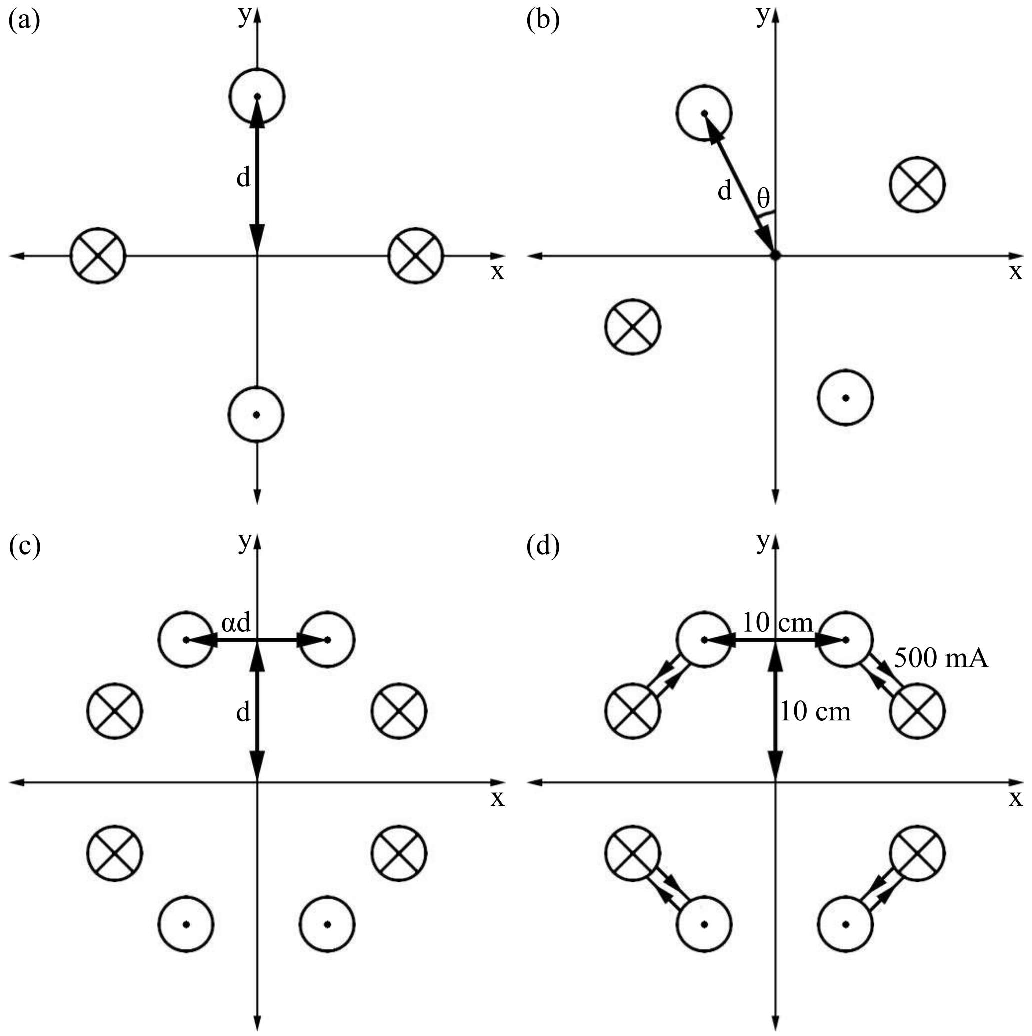

Figure 2.11: Four potential wire configurations for canceling stray magnetic field gradients. The first three configurations use ideal wires - straight, unconnected, and infinitely long - carrying current in the $\pm z$-direction. The (a) simple cross configuration satisfies our field requirements but blocks lasers incident along all four axes, while the (b) tilted cross configuration produces a non-zero $\partial B_x/\partial x$. The (c) double cross configuration, essentially a superposition of two tilted cross configurations, satisfies all field and space requirements. The (d) physically realistic double cross configuration uses wires 20 cm long that are parts of square coils and still satisfies all requirements to a high degree.

expect, the gradients transform like

$$\begin{aligned} \partial B_x/\partial x &= A\cos(\theta) \\ \partial B_x/\partial y &= -A\sin(\theta), \end{aligned} \tag{2.50}$$

where A is dependent on d and I. Here, a solution presents itself: if we construct one set of four wires rotated by θ and another rotated by $-\theta$, then their contributions to $\partial B_x/\partial x$ will cancel and their contributions to $\partial B_x/\partial y$ will add. For this "double cross" configuration, shown in Fig. 2.11(c), the size d of the configuration has been redefined and the rotation angle θ has been reparameterized by $\alpha = 2\tan(\theta)$. To prove that this configuration would still work if made more realistic, we make the wires and the corresponding integral in Eq. 2.49 run from $z = -l/2$ to $z = +l/2$, where l is the length of the wires. Using the physical parameters shown in Fig. 2.11(d) to calculate the field produced by the four coils, we find $\partial B_x/\partial y = 4.40$ mG/cm, $\partial B_x/\partial x \sim 10^{-16}$ mG/cm, and $\mathbf{B} = 0$ at the origin. One can qualitatively check these results by examining the plot of the magnetic fields created by the realistic loop configuration shown in Fig. 2.12.

Theoretically, then, we could cancel any arbitrary field gradients by building one of these configurations for each lab axis. Realistically, though, it would be a daunting task to fit twelve more coils into the already-crowded space around the science cell. More feasible options might include building the "tilted cross" configuration for each axis and using the existing anti-

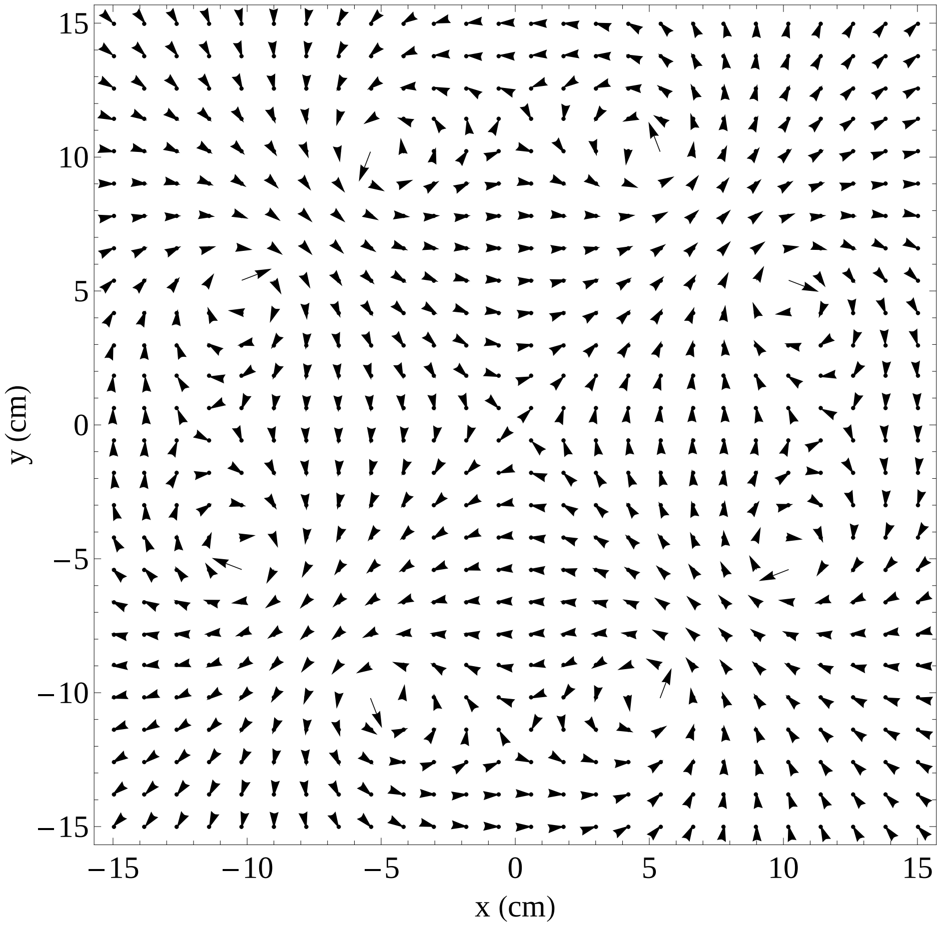

Figure 2.12: Magnetic fields of the realistic, four-coil configuration (Fig. 2.11(d)) we propose to cancel stray gradients. Notice that at the center, $\partial B_x/\partial y = \partial B_y/\partial x > 0$, $\partial B_x/\partial x = \partial B_y/\partial y = 0$, and $\mathbf{B} = 0$, as required.

Helmholtz coils to cancel the small divergence gradients created, building the gradient-canceling coils larger and farther away from the science cell, or concentrating on nullifying the gradients along one or two axes. A more comprehensive study of what magnetic field gradients actually need to be corrected would better enable us to decide which of these options, or combination of options, would most be worth the time, effort, and increase in apparatus complexity that such a project would entail.

2.5 Spinor Atom Laser

One of the interesting experiments we can perform with a spinor condensate involves the production of a spinor atom laser. Following the experimental realization of Bose-Einstein condensation in 1995, there was a surge of proposals of methods by which this newly created medium could be used to produce an atom laser [44]. As its name suggests, the atom laser is the matter analog to the conventional photon laser. The trap, be it magnetic or optical, represents the lasing cavity in which atoms in a single quantum state accumulate through the gain mechanism of Bose-Einstein condensation. The atoms are somehow outcoupled from the trapped mode in the cavity to an untrapped lasing mode, which results in a phase-coherent stream of atoms propagating in the same quantum state.

A pulsed atom laser was first created by the Ketterle group in 1996 by using a Landau-Zener frequency sweep to outcouple sodium atoms from the

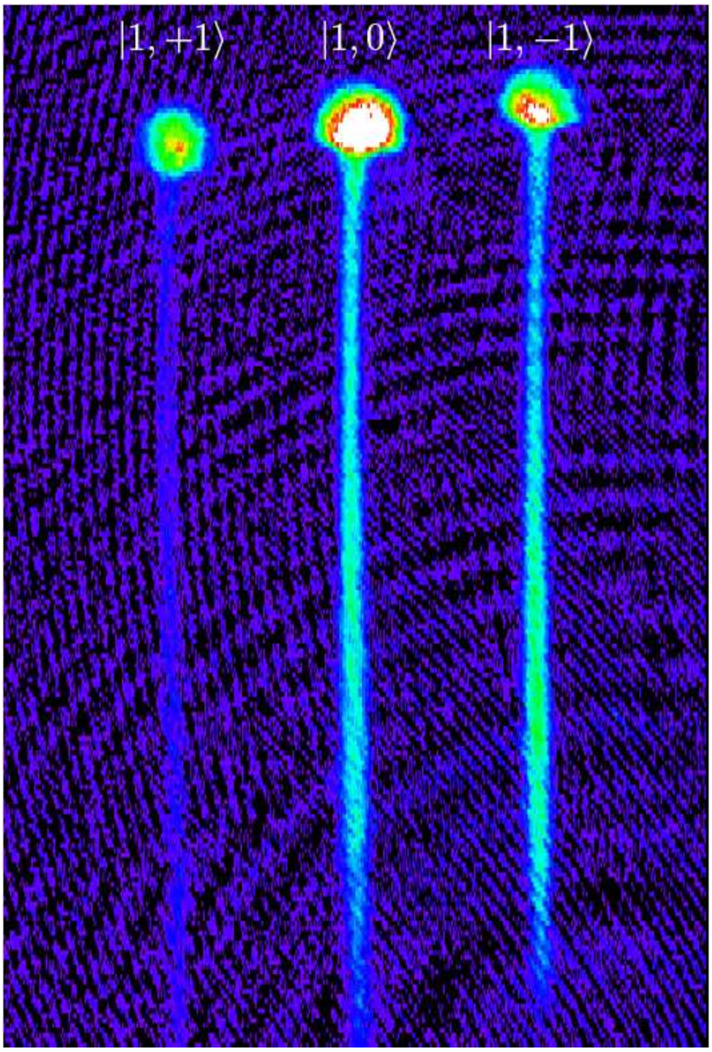

Figure 2.13: The three components of a spinor condensate are outcoupled from the optical trap by gravity to form a spinor atom laser

magnetically trapped $|1,-1\rangle$ state to the magnetically untrapped $|1,0\rangle$ and magnetically repelled $|1,+1\rangle$ states [41]. Once outcoupled, the atoms simply propagated downward under the influence of gravity. Atom lasers have also been outcoupled from magnetic trapping by Raman coupling [45] and from optical trapping by gravity [46], as we do. Pulsed atom lasers have also been created by allowing atoms to tunnel under the influence of gravity out of a vertical optical lattice, an array of potential wells created by the antinodes of a standing optical wave [2]. Since a spinor condensate cannot be created in a magnetic trap, we use the last method of outcoupling to produce spinor atom lasers like the one shown in Fig. 2.13.

Once we have performed a Landau-Zener sweep on the optically trapped condensate, we simply lower the optical trapping potential until atoms begin to leak out of the trap. To produce an atom laser of uniform but appreciable intensity, we must adjust both the amount by which and duration for which the trap potential is lowered. As shown in Fig. 2.14(a), if we reduce the potential too far, the trapped condensate is quickly depleted by outcoupling but if we do not reduce the potential far enough, the atom stream is anemic.

Our attempts to observe a pulsed atom laser have been limited by the fact that the condensate requires the potential to be lowered for approximately 9 ms in order to lase properly. When the potential is lowered for shorter periods of time, the condensate leaks out in a tapered shape and lacks a clean distinction between the trapped condensate and the outcoupled stream, as shown in Fig. 2.14(b). By the time a second pulse could begin to lase cleanly,

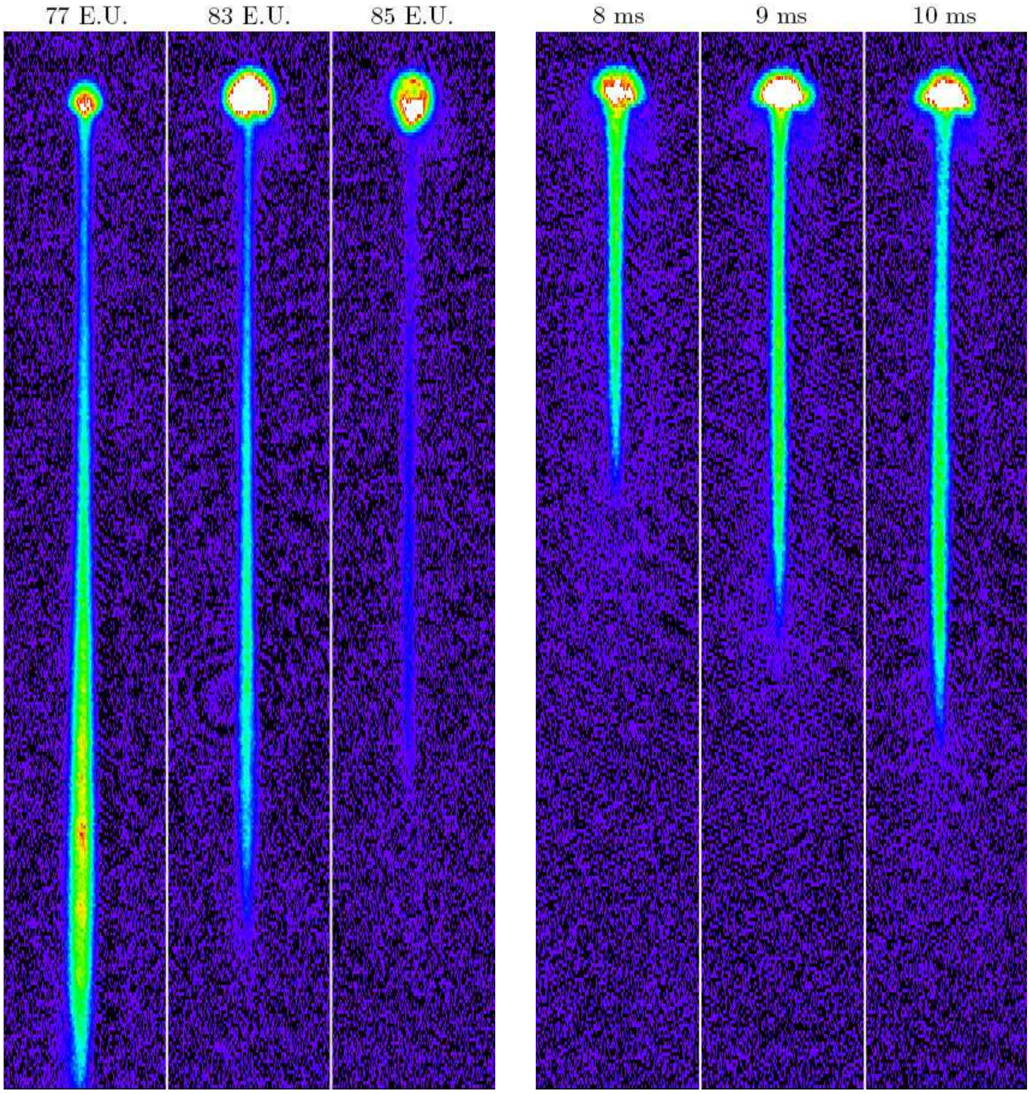

(a) (b)

Figure 2.14: Illustrations of the dependence of the atom laser's shape on the (a) value to which and (b) duration for which the optical trapping potential is reduced. The lasing time is 12 ms for the examples in (a), so even a relatively thin atom stream begins to taper off. Notice that for each parameter, there is a range of values that are optimal for atom lasing, wherein the stream is fully formed but does not taper off too quickly as the condensate is depleted.

the first would have already fallen below the range of our imaging. Also, potential ramping that is rapid enough to create pulses that are brief enough to be imaged in their entirety would cause excitations in the condensate.

If we allow the condensate to lase for more than approximately 10 ms, the stream tapers as the condensate is depleted, even for a well-chosen value of the lowered trapping potential. In order to compensate for this, we should lower the trapping potential quickly to begin the outcoupling and then continue to lower it slowly to the keep the rate of outcoupling constant. By carefully calibrating the initial potential drop and the slow potential ramp, we should be able to produce an atom stream that maintains a uniform thickness until the trapped condensate has been completely depleted.

Note that this outcoupling procedure does not involve the spinor nature or magnetic states of the condensate in any way, so it can be used to create an atom laser out of any optically trapped condensate. Upon further refinement of our optical trap alignment, we plan to study the evolution of a single vortex core in an atom laser, which is similar to the model of a Raman-outcoupled topological atom laser proposed by Blakie et al. [47]. By transferring horizontal cross-sections of this laser into the $F = 2$ hyperfine manifold and imaging these slices, we hope to be able to study the evolution of a vortex in a single condensate.

Chapter 3

Feshbach Resonance

By making all sublevels of the ^{87}Rb ground state available for experimentation, the optical trap and Landau-Zener sweeps have together enabled us to pursue studies of Feshbach resonances. No resonances are predicted for the $|1,-1\rangle \otimes |1,-1\rangle$ scattering channel [48] but many have been predicted [39, 48] and observed [49–51] for scattering channels involving the magnetically untrappable $|1,+1\rangle$ state. Of these many intra- and interspecies Feshbach resonances, we are interested specifically in the interspecies resonance between the $|1,+1\rangle$ and $|2,-1\rangle$ states that occurs at a very accessible magnetic field of 9.1 G. We have chosen to investigate this resonance first because of the ease with which we can produce a 9.1 G field, and because the interspecies nature of the resonance allows us to observe the binary condensate's time evolution, as we discuss in Section 3.6.

Feshbach resonances are a topic of great theoretical and experimental interest because the scattering length of the condensate varies drastically around resonance with small changes in an external experimental parameter. Feshbach resonances can be observed by tuning a time-dependent optical [52] or RF field [53], but we and others [49–51, 54, 55] observe resonance by tuning a static magnetic field. The Wieman group has recently varied the scattering length in order to tune a binary condensate composed of ^{85}Rb and ^{87}Rb atoms between miscibility and immiscibility [56]. They determine the miscibility of the condensate by observing the spatial separation of its components, which is very similar to the experiment we describe in Section 3.6. The scattering length has also been tuned to negative values in order to observe matter wave solitons propagating in a single-beam optical trap [54] and the collapse of a condensate with attractive interactions [57], a so-called "bosenova."

The other important feature of Feshbach resonance is molecule formation and increased condensate loss. Feshbach resonance involves two atoms tunneling between an unbound state and a quasi-bound molecular state. Both atoms can be ejected from the trap if they undergo an inelastic collision that causes them to undergo transitions to other quantum states and release energy. When they are in the quasi-bound state, a collision with a third atom can be sufficient to cause the two atoms to undergo a transition to a bound molecular state. This molecule formation has been used to create Bose-Einstein condensates of diatomic molecules from ultra-cold Fermi gases [23, 24]. In this chapter, we discuss the theoretical background of the

Feshbach losses and scattering length variability associated with Feshbach resonances and discuss the results of experiments that we have undertaken to measure these features directly.

3.1 Scattering Length Theory

Remarkably, the majority of interatomic interactions within a Bose-Einstein condensate are characterized by a single parameter, the s-wave scattering length a. Essentially, a is a measure of the interaction between atoms in the condensate, which is attractive for $a < 0$ and repulsive for $a > 0$. In this section, we will sketch out a brief explanation of the origin of this parameter and the role it plays in determining the behavior of the condensate. For further details, we recommend consulting the more mathematically rigorous discussions [30, 58] of scattering theory from which we draw this sketch.

3.1.1 Two-Particle Scattering

In Bose-Einstein condensates, interatomic interactions are predominately elastic, in which the two atoms exchange momentum but do not change their individual quantum states. This enables the condensate to rethermalize continuously, a mechanism that is crucial for evaporative cooling. Here we address a simple case, a low-energy elastic collision of two particles in the same quantum state. Working in the center-of-mass frame, we describe the scattering of one particle as a sum of an incoming plane wave and a scattered spherical wave:

$$\psi = \mathrm{e}^{ikz} + f(\theta)\frac{\mathrm{e}^{ikr}}{r}, \tag{3.1}$$

where k is the wave number of the incident particle propagating in the $+\hat{\mathbf{z}}$ direction. The function $f(\theta)$ is the scattering amplitude and is only dependent on the scattering angle, which, as in classical mechanics, is the angle between the incident and scattered momentum vectors. This scattering amplitude is important because it is the amplitude of the scattered wave and, when squared and integrated over all angular space, gives the scattering cross section:

$$\sigma = 2\pi \int_0^\pi |f(\theta)|^2 \mathrm{d}\theta. \tag{3.2}$$

Our task, then, is to determine a value for $f(\theta)$. Since the interaction potential of the atoms is spherically symmetric, we can express the scattering wave function as an expansion in terms of Legendre polynomials, or

$$\psi = \sum_{l=0}^{\infty} A_l P_l(\cos\theta) R_{kl}(r). \tag{3.3}$$

We can solve the Schrödinger equation using this wave function and, comparing the solution to Eq. 3.1, we find the scattering amplitude to be given by

$$f(\theta) = \frac{1}{2ik} \sum_{l=0}^{\infty} (2l+1)(\mathrm{e}^{i2\delta_l(k)} - 1) P_l(\cos\theta), \tag{3.4}$$

where $\delta_l(k)$ is a phase shift associated with the radial wave function that is induced by the potential.

Here, since $k = 2\pi/\lambda = p/\hbar$ and we are working in the low-energy limit, we are also working in the limit $k \to 0$. For elastic collisions of neutral atoms in the ground state, it can be shown [58] that for $l = 0$, $\delta_l(k)$ approaches

$$\lim_{k\to 0} \delta_0(k) = -ak, \tag{3.5}$$

where a is introduced as the s-wave scattering length, and that $\delta_l(k)$ is proportional to an order of k^3 or higher for all $l > 0$. Therefore, as k approaches zero, the $(\mathrm{e}^{i2\delta_l(k)} - 1)$ term in Eq. 3.4 quickly goes to zero for all $l > 0$ and so the scattering magnitude is dominated in the low-energy limit by the $l = 0$ (s-wave) term. For the $l = 0$ case, we take advantage of the fact that $\mathrm{e}^{i2\delta_l} \approx \mathrm{e}^{-i2ak} \approx 1 - i2ak$ if k is small to find that $f(\theta)$ from Eq. 3.4 simply approaches

$$f(\theta) = -a \tag{3.6}$$

in the low-energy limit.

We can now insert this value for $f(\theta)$ into Eq. 3.2 to find the one-particle scattering cross section

$$\sigma = 4\pi a^2. \tag{3.7}$$

In order to describe two-particle scattering, we simply modify the original wave function from Eq. 3.1 to describe an additional particle incident in the $-\hat{\mathbf{z}}$ direction and scattering at an angle of $\pi - \theta$. As described in Chapter 1, this two-particle wave function must be symmetric under the exchange operator if the particles are bosons and anti-symmetric if the particles are fermions, so we find

$$\psi = [\mathrm{e}^{ikz} \pm \mathrm{e}^{-ikz}] + [f(\theta) \pm f(\pi - \theta)]\frac{\mathrm{e}^{ikr}}{r}, \tag{3.8}$$

where we use + for bosons and − for fermions. The two-particle scattering cross section is calculated by integrating the total scattering amplitude, so we find

$$\sigma = 2\pi \int_0^\pi |f(\theta) \pm f(\pi - \theta)|^2 \mathrm{d}\theta. \tag{3.9}$$

Therefore, the two-particle scattering cross section evaluates to

$$\sigma = 8\pi a^2 \tag{3.10}$$

for identical bosons and $\sigma = 0$ for identical fermions. This result indicates that the incidence of interatomic interactions is proportional to a^2, which is consistent with the observations of non-interacting condensates when the scattering length is tuned to $a \approx 0$ [59].

3.1.2 Gross-Pitaevskii Equation

The parameter a characterizes the strong scattering interactions of specific pairs of particles, but we would also like to describe the behavior of the condensate as a whole. Although scattering interactions are strong and important in determining the behavior of the condensate, they occur only at very close range. When the average interparticle spacing is much greater than the scattering length, as in the dilute gas of our condensate, then the short-range interatomic interactions can be “integrated out” in the low-energy limit. The effective interaction between two particles then is simply represented by the pseudopotential

$$U = \frac{4\pi\hbar^2 a}{m}\delta(\mathbf{r}_1 - \mathbf{r}_2), \tag{3.11}$$

where $\mathbf{r}_1$ and $\mathbf{r}_2$ are the positions of the two particles. This step, the reprentation of individual interactions within a multi-particle system by an effective interaction, is known as the mean-field approximation.

To describe the state of the entire condensate, we can simply add this pseudopotential to the regular Hamiltonian and construct the Gross-Pitaevskii equation, which is the analog to the Schrödinger equation for a Bose gas:

$$\left[-\frac{\hbar^2}{2m}\nabla^2 + V(\mathbf{r}) + \frac{4\pi\hbar^2 a}{m}|\Psi(\mathbf{r},t)|^2\right]\Psi(\mathbf{r},t) = i\hbar\frac{\partial}{\partial t}\Psi(\mathbf{r},t). \tag{3.12}$$

Here, the Dirac delta $\delta(\mathbf{r}_1 - \mathbf{r}_2)$ from Eq. 3.11 becomes the density of particles $|\Psi(\mathbf{r},t)|^2$, which makes the interaction pseudopotential term non-linear. There are two properties of this equation that are of particular interest to our present discussion.

First, in keeping with the analogy to the Schrödinger equation, we can solve the time-dependent Gross-Pitaevskii equation with respect to time to find the time-independent Gross-Pitaevskii equation:

$$\left[-\frac{\hbar^2}{2m}\nabla^2 + V(\mathbf{r}) + \frac{4\pi\hbar^2 a}{m}|\psi(\mathbf{r})|^2\right]\psi(\mathbf{r}) = \mu\psi(\mathbf{r}). \tag{3.13}$$

Here, the eigenvalue of the modified Hamiltonian is the chemical potential μ instead of the total energy E because the condensate number is not assumed to be constant; atoms are free to condense into the ground state and rethermalize from it without altering this result. As with the stationary states found by solving the time-dependent Schrödinger equation, the time-dependent stationary state order parameter $\Psi(\mathbf{r}, t)$ is related to the time-independent order parameter $\psi(\mathbf{r})$ by

$$\Psi(\mathbf{r}, t) = \psi(\mathbf{r})\mathrm{e}^{-i\mu t/\hbar}. \tag{3.14}$$

This introduces the phase of the condensate order parameter, which plays a central role in the theory of vortices. According to hydrodynamics, the velocity of the condensate is given by

$$\mathbf{v} = \frac{\hbar}{m}\nabla\phi, \tag{3.15}$$

where ϕ is the phase of the order parameter. Since the order parameter can only have a single value at any given point, the change in its phase along any

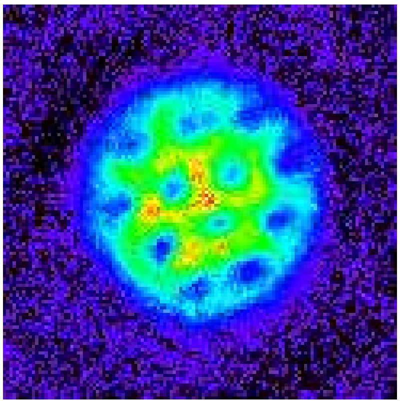

Figure 3.1: Vortices in an optically trapped condensate [60]. A subject of current investigation in the lab, vortices are a theoretical consequence of the phase of the condensate order parameter that arises by solving the time-dependent Gross-Pitaevskii equation.

closed loop must be an integer multiple of 2π, or

$$\Delta\phi = \oint \nabla\phi \cdot \mathrm{d}\mathbf{l} = 2\pi l, \tag{3.16}$$

where l is an integer. Therefore, the circulation Γ around a closed loop is also quantized, or

$$\Gamma = \oint \mathbf{v} \cdot \mathrm{d}\mathbf{l} = l\frac{h}{m}. \tag{3.17}$$

Because of this quantization of circulation, when the condensate is given angular momentum, it forms a matrix of vortex cores with one unit of angular momentum each instead of rotating cohesively, as viscous fluids do. The behavior of vortices in optically trapped condensates, such as the one pictured in Fig. 3.1, are a topic of ongoing investigation [5] in the lab.

Second, notice the effect that the sign of a has on the total energy of the system. For a constant number of particles, the time-independent Gross-Pitaevskii equation states that as the system's density increases, its total energy increases for positive a, decreases for negative a, and remains the same for $a = 0$. These results imply that interatomic interactions are repulsive for $a > 0$ and attractive for $a < 0$, and that atoms are effectively non-interacting for $a \approx 0$. In the first two cases, the change in energy is proportional to $|a|$ for a given change in density, so, as demonstrated already, a provides a measure of the interaction strength within the condensate.

The Gross-Pitaevskii equation can also be used to describe a binary condensate composed of atoms in states $|1 - +1\rangle$ and $|2, -1\rangle$. Neglecting losses, the system in this case is described by a pair of coupled non-linear equations:

$$\left[-\frac{\hbar^2}{2m}\nabla^2 + V_1(\mathbf{r}) + \frac{4\pi\hbar^2 a_{11}}{m}|\Psi_1|^2 + \frac{4\pi\hbar^2 a_{12}}{m}|\Psi_2|^2\right]\Psi_1 = i\hbar\frac{\partial}{\partial t}\Psi_1,$$

$$\left[-\frac{\hbar^2}{2m}\nabla^2 + V_2(\mathbf{r}) + \frac{4\pi\hbar^2 a_{22}}{m}|\Psi_2|^2 + \frac{4\pi\hbar^2 a_{12}}{m}|\Psi_1|^2\right]\Psi_2 = i\hbar\frac{\partial}{\partial t}\Psi_2, \quad (3.18)$$

where a_{11} and a_{22} are the intraspecies scattering lengths for the $|1, +1\rangle$ and $|2, -1\rangle$ states and a_{12} is the interspecies scattering length. As is usually the case, Ψ_1 and Ψ_2 are functions of $\mathbf{r}$ and t here. As we will describe in Section 3.6 on the time evolution of a binary condensate near an interspecies Feshbach resonance, the inclusion of the interspecies scattering cross-term leads to interesting non-equilibrium component separation dynamics [33].

3.2 Feshbach Theory

This picture of interatomic interactions, wherein unbound atoms come together and scatter elastically, is valid as long as the energy of the unbound atoms is not close to the energy of a bound molecular state. When the unbound state is close in energy to an allowed bound state, the two states are coupled in a phenomenon known as Feshbach resonance.

Figure 3.2 shows a schematic representation of a Feshbach resonance. Here, we must define the terms we will use in our theoretical description of this event. Each of the two potential curves in Fig. 3.2 represents one channel, or quantum state. Each channel has a threshold energy E_{th}, which is the asymptotic value of the potential at infinite separation. If the atoms have a combined energy greater than E_{th}, then the channel is said to be open and the atoms are in an unbound continuum state. If the atoms have a combined energy less than E_{th}, then the channel is said to be closed. Within each closed channel is a series of bound states, which could correspond to the rotational or vibrational modes of a diatomic molecule.

Looking at Fig. 3.2, we can observe what happens in the absence of any coupling between the two channels. The atoms approach each other in the continuum state, repel each other strongly as their filled electronic orbitals begin to overlap, and have sufficient energy to escape the potential well again. In other words, in the absence of a Feshbach resonance, atoms scatter as described in the previous section. When the continuum state of

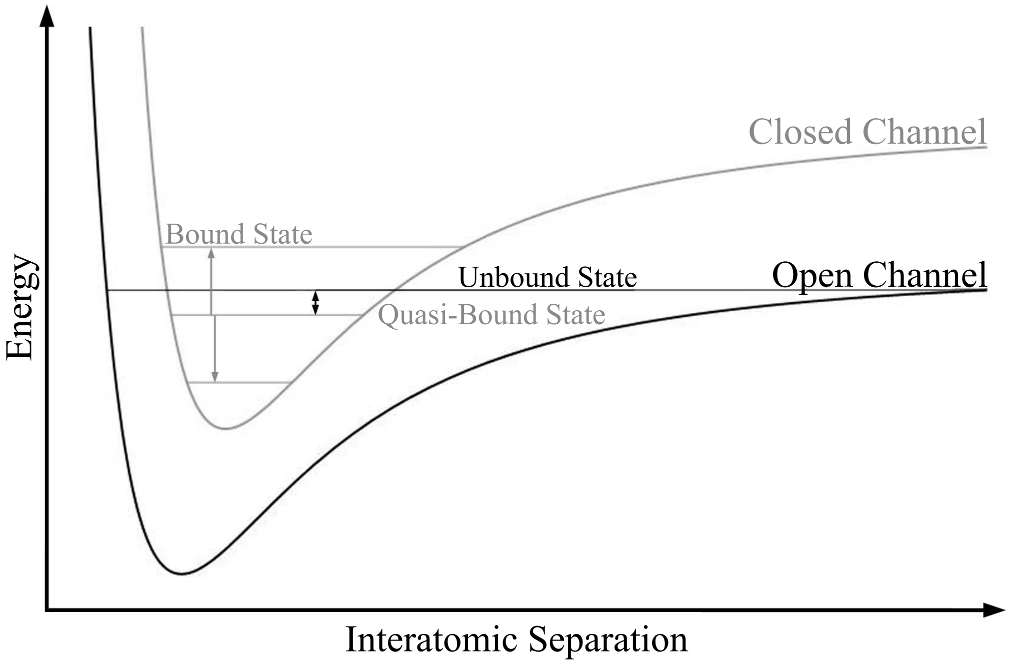

Figure 3.2: Conceptual diagram of the two channels involved in Feshbach resonance. The atoms are initially in the unbound state of the open channel. If the unbound state's energy is far from the energy of any state in the closed channel, then collisions are elastic and the atoms remains in the unbound state. If the energy of an allowed state in the closed channel is nearly degenerate with the energy of the unbound state (as very loosely shown), then the atoms can tunnel (black arrow) into and out of the quasi-bound state, a phenomenon known as Feshbach resonance. If a third atom collides with the pair while they are in the quasi-bound state, then they can undergo a transition (grey arrow) to a bound state, form a stable molecule, and leave the trap.

the open channel is nearly degenerate in energy with a bound state in the closed channel, however, atoms can tunnel from the continuum state to the bound state. This specific bound state is considered "quasi-bound," because the atoms are just as likely to tunnel back out of the bound state as they are to tunnel in.

3.2.1 Tunable Scattering Length

The phenomenon of Feshbach resonance has two important physical manifestations. First, the scattering length a changes dramatically, in both sign and magnitude, in the vicinity of a Feshbach resonance. To see why this occurs, we examine the perturbation of the interaction pseudopotential (Eq. 3.11) due to the coupling of open and closed channels. To first order, the energy correction is given by

$$U_1 = \langle \Psi_{\mathrm{u}} | H_{\mathrm{CO}} | \Psi_{\mathrm{u}} \rangle = 0, \tag{3.19}$$

where Ψ_{u} is the unbound continuum state that the atoms occupy initially and H_{CO} is the Hamiltonian that represents the coupling between the open and closed channels. The first-order energy correction is equal to zero because, by definition, the continuum state cannot be coupled to itself using this specific Hamiltonian.

The second-order energy correction is given by

$$U_2 = \sum_n \frac{|\langle \Psi_n | H_{\mathrm{CO}} | \Psi_{\mathrm{u}} \rangle|^2}{E_{\mathrm{u}} - E_n}, \tag{3.20}$$

where Ψ_n is the nth bound state in the closed channel and E_n is its energy. If the unbound state Ψ_{u} is nearly degenerate with the quasi-bound state Ψ_{qb}, then this sum is dominated by the term involving Ψ_{qb}. All other terms in the sum vary slowly with respect to changes in E_n and E_{u}, so they can be assumed to be constant over the region of a Feshbach resonance. Thus, the total perturbed interaction pseudopotential is given by

$$\frac{4\pi\hbar^2}{m}a = \frac{4\pi\hbar^2}{m}a_{\mathrm{bg}} + \frac{|\langle\Psi_{\mathrm{qb}}|H_{\mathrm{CO}}|\Psi_{\mathrm{u}}\rangle|^2}{E_{\mathrm{u}} - E_{\mathrm{qb}}}, \tag{3.21}$$

where a_{bg}, the background scattering length, takes into account the scattering length without coupling between the channels and the contributions from coupling with all non-resonant bound states.

We now specify that the energy levels are dependent on the magnitude of an external magnetic field, as in our experiment. We define a field B_0 at which $E_{\mathrm{u}} = E_{\mathrm{qb}}$ and the energy of each state is dependent on its magnetic moment

$$\mu = -\frac{\partial E}{\partial B}. \tag{3.22}$$

Therefore, the denominator in Eq. 3.21 becomes

$$E_{\mathrm{u}} - E_{\mathrm{qb}} = (\mu_{\mathrm{qb}} - \mu_1 - \mu_2)(B - B_0), \tag{3.23}$$

where μ_1 and μ_2 are the magnetic moments of the two atoms in the unbound state and μ_{qb} is the magnetic moment of the quasi-bound molecular state. We can insert this expression into Eq. 3.21 and rearrange to find an expression for the scattering length

$$a = a_{\mathrm{bg}} + \frac{m}{4\pi\hbar^2}\frac{|\langle\Psi_{\mathrm{qb}}|H_{\mathrm{CO}}|\Psi_{\mathrm{u}}\rangle|^2}{(\mu_{\mathrm{qb}} - \mu_1 - \mu_2)(B - B_0)}. \tag{3.24}$$

We can recast this into a far simpler expression for the scattering length in the region of a Feshbach resonance:

$$a(B) = a_{\mathrm{bg}}\left(1 - \frac{\Delta B}{B - B_0}\right), \tag{3.25}$$

where we define the width of the resonance

$$\Delta B = \frac{m}{4\pi\hbar^2 a_{\mathrm{bg}}}\frac{|\langle\Psi_{\mathrm{qb}}|H_{\mathrm{CO}}|\Psi_{\mathrm{u}}\rangle|^2}{(\mu_1 + \mu_2 - \mu_{\mathrm{qb}})}. \tag{3.26}$$

Notice that the scattering length diverges to $\pm\infty$ as B approaches B_0, meaning that the magnitude and sign of a can be changed dramatically by a slight change in B. In reality, however, inelastic decay from the closed channel necessitates a modification to this approximation. If the atoms are not assumed to spend an infinite amount of time in the quasi-bound state, then that state must have a finite width. When decay from the quasi-bound state and the state's finite width are considered, Eq. 3.25 becomes the complex expression

$$a(B) = a_{\mathrm{bg}}\left(1 - \mathrm{e}^{2i\phi_R}\frac{\Delta B_{\mathrm{el}}}{B - B_0 + \frac{1}{2}i\Delta B_{\mathrm{inel}}}\right), \tag{3.27}$$

where ϕ_R is a resonance phase constant, ΔB_{el} is the elastic resonance width described above, and ΔB_{inel} is the inelastic resonance width [39]. The real part of this function represents the effective scattering length and the imaginary part is proportional to the two-body loss rate due to Feshbach interactions. This resonance width is given by

$$\Delta B_{\mathrm{inel}} = \hbar\Gamma_{\mathrm{qb}}/(\mu_{\mathrm{qb}} - \mu_1 - \mu_2), \tag{3.28}$$

where Γ_{qb} is the finite width, in terms of frequency, of the quasi-bound state. The real part of this expression,

$$\mathrm{Re}\big(a(B)\big) = a_{\mathrm{bg}}\left[1 - \gamma_{\mathrm{Re}}(B)\frac{\Delta B_{\mathrm{el}}}{(B - B_0)^2 + (\frac{1}{2}\Delta B_{\mathrm{inel}})^2}\right], \tag{3.29}$$

where

$$\gamma_{\mathrm{Re}}(B) = \cos(2\phi_R)(B - B_0) + \sin(2\phi_R)\Delta B_{\mathrm{inel}}/2, \tag{3.30}$$

is now a smooth function that does not diverge at $B = B_0$. Thus, the effective scattering length does not diverge at a Feshbach resonance when inelastic processes are considered.

We would like to know, then, how exactly the effective scattering length does vary under these conditions. By taking the derivative of Eq. 3.29 with respect to B and performing some algebraic manipulation, we find that the real part of the scattering length reaches its extrema of

$$\mathrm{Re}\big(a(B_{\mathrm{ex}})\big) = a_{\mathrm{bg}}\left[1 - \big(\sin(2\phi_R) \pm 1\big)\frac{\Delta B_{\mathrm{el}}}{\Delta B_{\mathrm{inel}}}\right] \tag{3.31}$$

at

$$B_{\mathrm{ex}} = B_0 + \frac{-\sin(2\phi_R) \pm 1}{2\cos(2\phi_R)}\Delta B_{\mathrm{inel}}. \tag{3.32}$$

As expected, when we neglect inelastic scattering and the finite width of the quasi-bound state, the limits of these two values are

$$\lim_{\Gamma_{\mathrm{qb}}\to 0} \mathrm{Re}\big(a(B_{\mathrm{ex}})\big) = \mp\infty \tag{3.33}$$

and

$$\lim_{\Gamma_{\mathrm{qb}}\to 0} B_{\mathrm{ex}} = B_0. \tag{3.34}$$

Equation 3.31 also allows us to define the range Δa of the scattering length over a resonance as

$$\Delta a = 2a_{\mathrm{bg}}\frac{\Delta B_{\mathrm{el}}}{\Delta B_{\mathrm{inel}}} = \frac{m}{2\pi\hbar^2}\frac{|\langle\Psi_{\mathrm{qb}}|H_{\mathrm{CO}}|\Psi_{\mathrm{u}}\rangle|^2}{\hbar\Gamma_{\mathrm{qb}}}, \tag{3.35}$$

which we can use as a measure of the strength of a particular resonance.

3.2.2 Loss Rates

The second physical manifestation of a Feshbach resonance are increased two- and three-body loss rates due to molecule formation. Two-body losses occur

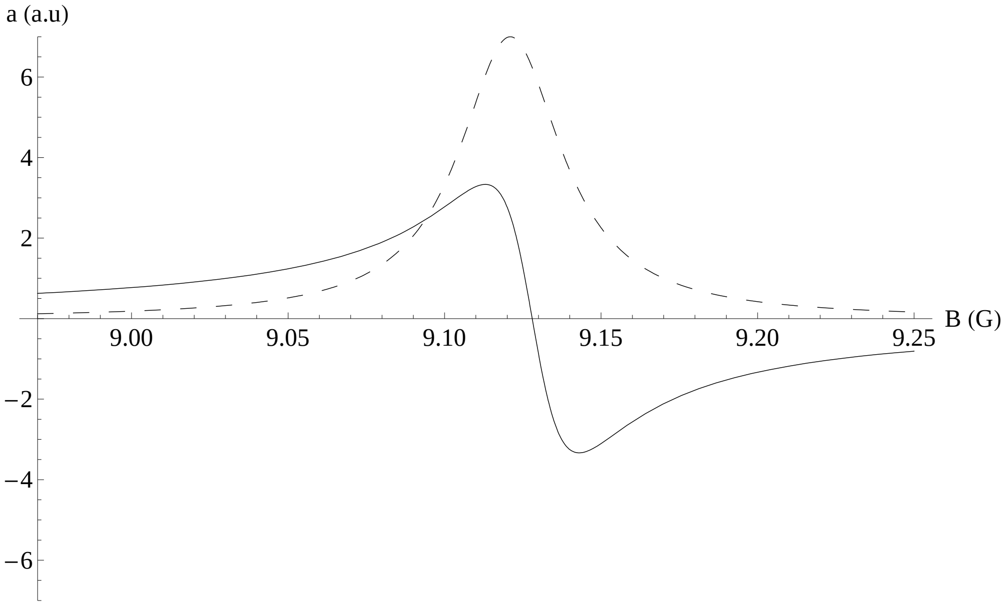

Figure 3.3: A theoretical plot of the real (solid) and imaginary (dashed) parts of the complex scattering length around the 9.1 G interspecies resonance. For this plot, we use parameters extracted from the results of Widera et al. [51] and listed as Refs. 1 and 2 in Table 3.1. Because the scaling of each function cannot be determined directly from the data given, both are scaled in arbitrary units and re-centered on $a = 0$.

if the two atoms undergo an inelastic collision that conserves angular momentum but results in energy being released. This extra energy, whether gained from transitions between magnetic sublevels or between the two hyperfine manifolds, can be sufficient to eject both atoms from the trap. Three-body losses can occur when two atoms in the quasi-bound state collide with a third atom. If the pair gains or loses a quantum of energy through this collision, then the two atoms can undergo a transition to a fully bound molecular state from which they cannot tunnel back out. The molecule can then become untrapped because of its different electric dipole moment and the energy released by the transition might eject the third atom, as well. We collectively refer to these two loss mechanisms as Feshbach losses, although we do not presently know which of these loss mechanisms is dominant. By measuring the total loss rate as the condensate evolves at various magnetic fields, we are able to map out our selected Feshbach resonance.

Just as the real part of our complex expression for a (Eq. 3.25) represents the effective scattering length for two-body collisions, the imaginary part is proportional to the two-body Feshbach loss rate. The imaginary part is given by

$$\mathrm{Im}\big(a(B)\big) = -a_{\mathrm{bg}}\gamma_{\mathrm{Im}}(B)\frac{\Delta B_{\mathrm{el}}}{(B-B_0)^2+(\frac{1}{2}\Delta B_{\mathrm{inel}})^2}, \tag{3.36}$$

where

$$\gamma_{\mathrm{Im}}(B) = \sin(2\phi_R)(B-B_0) - \cos(2\phi_R)\Delta B_{\mathrm{inel}}/2. \tag{3.37}$$

Therefore, we would expect the two-body loss rate around a Feshbach resonance to have the form of a Lorentzian distribution with an asymmetry introduced by the $\sin(2\phi_R)(B - B_0)$ term. For the sake of this thesis, we will assume our total loss rate is proportional to $\mathrm{Im}(a)$, even though the three-body loss mechanism should not be described using a component of the two-body scattering length. Since the three-body loss mechanism outlined above also depends on the number of atoms in the quasi-bound state, though, it should also increase around resonance. Further research is needed to determine exactly how each of these loss rates varies around resonance.

3.3 Two-Photon Transitions

In this thesis, we examine the $|1, +1\rangle \otimes |2, -1\rangle$ interspecies Feshbach resonance that occurs in a 9.1 G magnetic field. The preparation of a condensate composed equally of $|1, +1\rangle$ and $|2, -1\rangle$ atoms consists, speaking very broadly, of three distinct steps. First, we produce a condensate of $|1, -1\rangle$ atoms, transfer it to the optical trap, and fix the axial magnetic field, as described in Section 1.4. This portion of the process, which we mention so briefly here, represents years [4, 5, 17, 26–28] of diligent effort, and so we are fortunate to be able to consider this a stable base for our current experiment.

Second, we perform a slow Landau-Zener sweep of the magnetic field, as described in Section 2.2.1, to transfer the entire population of atoms to the $|1, +1\rangle$ state. This process has been extensively studied and tweaked slightly in the course of our current experimentation, but again, it remains fundamentally as we found it.

For the third step, we must transfer half of the atoms from the $|1, +1\rangle$ state to the $|2, -1\rangle$ state. Because $\Delta m_F = -2$ for this transition, we require the atoms to undergo two transitions simultaneously. As with Landau-Zener transitions, these transitions between different magnetic sublevels are actually driven by creating an oscillating magnetic field in the cell. For two-photon transitions and Feshbach studies, we use the North-South bias coils to produce a static field in the $+\hat{\mathbf{y}}$ direction and the vertical RF coil, which is located inside of the top quadrupole coil, to produce a vertical oscillating field. Again, we will treat these oscillating fields as radiation for the sake of conceptual simplicity, so this process is known as a two-photon transition.

As shown in Fig. 3.4, we use a microwave pulse at $\nu_{\mathrm{MW}} = 6.841$ GHz to excite atoms to a virtual state that is on the order of 300 kHz detuned above the $|2, 0\rangle$ state. From this virtual state, we use a simultaneous radio-frequency pulse to stimulate an emission to the $|2, -1\rangle$ state. We detune the intermediate state from the $|2, 0\rangle$ state so that atoms cannot remain in the intermediate state. To calibrate the two-photon pulse, we fix the microwave frequency and adjust the RF frequency to map out the resonance peak.

Considering only the RF transition, the proportion of atoms transferred to the $|2, -1\rangle$ state is given by

$$P(t) = \left(\frac{\Omega}{\Omega'}\right)^2 \sin^2\!\left(\frac{\Omega'}{2}t\right), \tag{3.38}$$

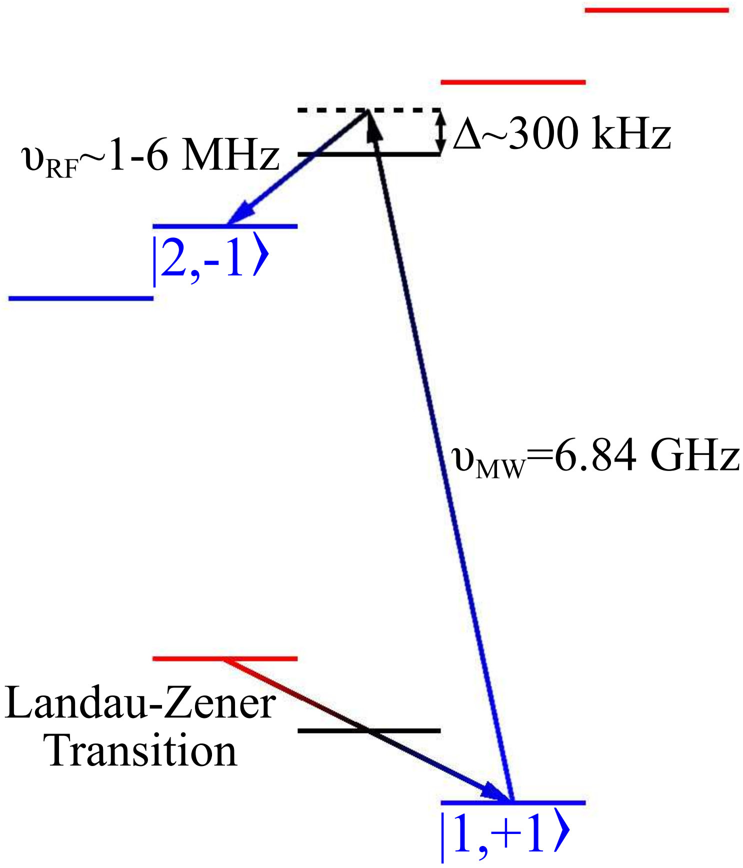

Figure 3.4: The two-photon transition consists of a microwave transition from the $|1,+1\rangle$ state to a virtual state detuned approximately 300 kHz above the $|2,0\rangle$ state and an RF transition from the virtual state to the $|2,-1\rangle$ state. The microwave transition involves the absorption of a 6.841 GHz photon and the RF transition involves the stimulated emission of a 6 MHz photon. This latter frequency is given imprecisely here because we recalibrate the RF frequency to transfer atoms in different magnetic fields.

where the effective detuned Rabi frequency Ω' is given by

$$\Omega' = \sqrt{\Omega^2 + \delta^2}. \tag{3.39}$$

The detuning δ of the angular frequency from resonance is given by

$$\delta = 2\pi(\nu - \nu_0). \tag{3.40}$$

A plot of this function and profiles of the resonance peak taken at two different values of of t are shown in Fig. 3.5.

For the purposes of studying the interspecies Feshbach resonance, we want to transfer half of the atoms from the $|1, +1\rangle$ state to the $|2, -1\rangle$ state. Although these two states have identical linear Zeeman splittings, their different quadratic Zeeman splittings make the RF frequency calibration highly dependent on the magnetic field. To compensate for this shift, we adjust how far the RF radiation is detuned from resonance. Fixing the pulse length at 700 μs, we tune the RF frequency to find $\nu_{1/2}$, the RF frequency on the lower side of the large central resonance peak that results in half of the atoms in the condensate being transferred to the $|2, -1\rangle$ state. Because producing equal populations of $|1, +1\rangle$ and $|2, -1\rangle$ atoms is crucial to our investigation of Feshbach resonance, considerations of how precisely we can calibrate $\nu_{1/2}$ at a given magnetic field are important to the design of experimental procedures for this investigation.

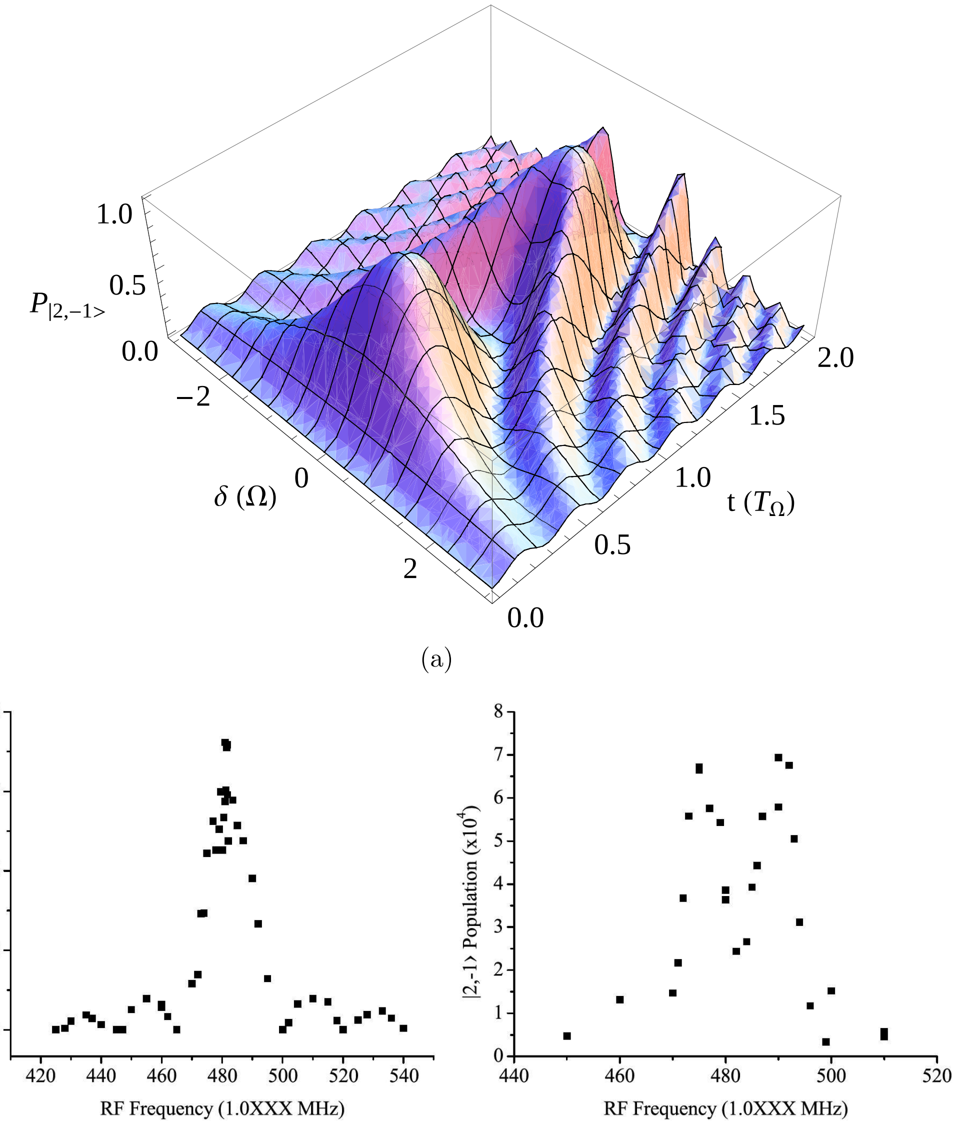

(a)

(b) t=500 μs

(c) t=1090 μs

Figure 3.5: Two-photon calibration data showing Rabi oscillations of atoms to the $|2,-1\rangle$ state. As per Eq. 3.39, the detuned Rabi frequency is greater than the resonant Rabi frequency, so the phase of the transition varies as the RF radiation is detuned from resonance. Part (a) shows the theoretical $|2,-1\rangle$ population as a function of the pulse length t and detuning δ. Parts (b) and (c) show the profile of the resonance peak at two different pulse lengths, which correspond to cuts in the preceding plot.

3.4 Feshbach Procedure

Our investigation of the interspecies Feshbach resonance is twofold; we map out the Feshbach resonance by measuring condensate losses at a range of field strengths and we infer how the scattering length changes around resonance by observing the time evolution of the two states on both sides of resonance. In order to do this, we need to produce equal populations of $|1,+1\rangle$ and $|2,-1\rangle$ atoms in a magnetic field close to resonance at 9.1 G.Let B_{ex} denote the value of the field in the vicinity of the Feshbach resonance, centered on B_0, that we are examining in a given trial. We have developed two different methods by which this can be accomplished: we can either perform a two-photon pulse in a 1.0 G field and then increase the field to B_{ex}, or we can set the field at B_{ex} and then perform a two photon pulse. As we will discuss, each method has complementary advantages and difficulties, but the transfer-at-field method is ultimately a more precise method and will be the default for future experimentation.

3.4.1 Ramp-to-Field Method

The main advantage of the ramp-to-field method is that the two-photon transfer process is completely independent of the resonant field value we are probing. We take advantage of Feshbach losses to calibrate the two-photon transition, but the loss rate near the center of the peak is too high to allow direct calibration. Because of the resonance peaks shown in Fig. 3.5 and various other calibration data sets, we have a detailed understanding of how the proportion of atoms transferred to the $|2,-1\rangle$ state varies with the pulse length and RF detuning.

Although the broad behavior of two-photon transfer process at 1.0 G is very well understood, we cannot calibrate $\nu_{1/2}$, the value of practical interest, nearly as precisely as we can using the method described in the "Transfer-at-Field Method" section. In short, because Feshbach losses deplete both states equally, any initial population difference results in a surplus population remaining in one of the states after the system has been allowed to evolve for a long period of time. By minimizing the total population of atoms remaining, we can very precisely calibrate $\nu_{1/2}$.

Because we perform the two-photon pulse far away from the Feshbach resonance in the ramp-to-field method, though, we cannot use this precise calibration method and we must simply image the large initial populations of each state. Using this method, we are measuring small changes in a relatively large signal instead of detecting marginal signal, so this method is far more vulnerable to variations in condensate production, imaging saturation, and differences in imaging efficiency between the two states. Therefore, we can only achieve roughly equal proportions in the two states with any reliability.

The ramp to B_{ex} is also problematic, regardless of the ramp speed. If we ramp the field quickly (1.0 G to B_{ex} in 1.0 ms), the ramp is likely to overshoot B_{ex} and the final field value is inexact. Since Feshbach losses are highly sensitive to the value of the magnetic field, particularly near the center of resonance, the imprecision with which the field is set at the end of a rapid ramp introduces a good deal of noise into our attempts to map the resonance.

A more gradual field ramp (1 G to 8.6 G in 1.0 ms and 8.6 G to B_{ex} in 10.0 ms) ends at a field that is closer to the intended B_{ex}, but it results in an overestimation of Feshbach losses. The more slowly we ramp the field to B_{ex}, the more time the system spends in fields around B_{ex} that are near resonance. Although we are only interested in the loss rate at B_{ex} over an evolve time Δt, or $L(B_{\mathrm{ex}})\Delta t$, we also measure a contribution to condensate loss from the ramp to B_{ex}, or

$$L_{\mathrm{Apparent}}(B_{\mathrm{ex}}) = L(B_{\mathrm{ex}})\Delta t + \int_{1G}^{B_{\mathrm{ex}}} \frac{L(B)}{(\mathrm{d}B/\mathrm{d}t)}\mathrm{d}B. \tag{3.41}$$

This overestimation is particularly severe if B_{ex} is above resonance, as the contribution of $L(B_0)$ to the integral in Eq. 3.41 becomes significant in comparison to $L(B_{\mathrm{ex}})\Delta t$. This inaccuracy is demonstrated in Fig. 3.6, which shows a highly asymmetric resonance peak that was produced by ramping upward through resonance to B_{ex}.

We can eliminate the need to ramp through resonance by discontinuously setting the field to a value well above 9.1 G and then ramping down to B_{ex}, for all $B_{\mathrm{ex}} > B_0$. Still, however, the additional condensate loss incurred by ramping through one of the tails of the Lorentzian distribution can be significant, particularly if B_{ex} is close to B_0.

Also, ramping the field slowly does not allow us to observe the time evo-

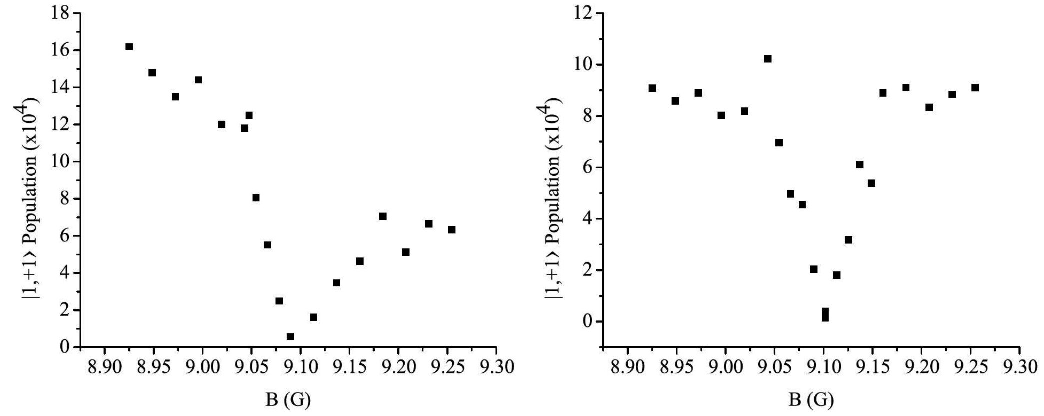

(a) (b)

Figure 3.6: Demonstration of Feshbach losses due to the field ramp. The data in part (a) were taken by ramping the field slowly (50 G/s) upward to the desired value. Notice that the points above 9.09 G, for which the field was ramped through resonance, exhibit significantly greater losses than the points symmetrically below resonance. The data in part (b) were taken by ramping upward to points for which $B \leq 9.10$ G and downward to points for which $B \geq 9.10$ G. Note how closely the two halves fit together at 9.10 G and the vast improvement in symmetry gained by not ramping through resonance.

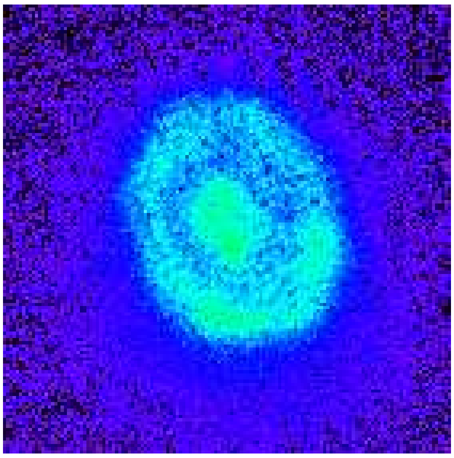

Figure 3.7: Ring structure in a condensate slightly below Feshbach resonance. According to Fig. 3.12, ring structures such as this one occur in the condensate approximately 3-5 ms after the two-photon pulse. We are unable to observe this region of the condensate's time evolution if we use the ramp-to-field method with a slow 10-ms field ramp. These data were taken a detuned probe beam to make the structure visible without saturation.

lution from the moment the two-component condensate is formed. A binary condensate forms a series of complex interpenetrating rings even without the influence of Feshbach resonance [33], we would like to be able to observe the time evolution of our binary condensate near the Feshbach resonance starting as soon after the two-photon pulse as possible. An example of a structure that can be observed in the condensate using a slow ramp is shown in Fig. 3.7.

Using the ramp-to-field method, then, we are forced to choose between a quick ramp, which imprecisely sets the field to be studied, and a slow ramp, which exaggerates condensate loss and prevents observation of the condensate's evolution for a significant period of time. These difficulties are inevitable results of performing the two-photon pulse at a field other than the field near the Feshbach resonance that we want to study.

3.4.2 Transfer-at-Field Method

The solution, then, is not to ramp the field at all after the two-photon pulse. By performing the two-photon pulse at the magnetic field to be studied, we can eliminate each problem mentioned in the previous section; we can ramp the field to the desired value slowly enough to ensure accuracy without considering spatial evolution or Feshbach interactions within the purely $|1, +1\rangle$ condensate.

Additionally, we are able to calibrate $\nu_{1/2}$ with far greater precision near the Feshbach resonance. To do this, we take advantage of the fact that one atom in each state is lost for every molecule that forms and escapes from the trap. If the two initial populations are equal, then the third atom in the three-body loss mechanism also has an equal probability of being in either state and so, on average, Feshbach losses deplete each state equally. By allowing the system to evolve for a long period of time in a field region with significant Feshbach losses, any initial difference in the populations of the two states results in a small surplus population remaining in one of the states. By simply minimizing the total number of atoms remaining in both states after the system has evolved, we can very precisely balance the initial populations of the states.

The simplicity of this method allows us to quickly calibrate $\nu_{1/2}$ for a range of fields. First, we tune the RF frequency until we can observe atoms remaining in both states. If these populations are substantial, we lengthen the period of time and tune the RF frequency more finely. By repeating this process, we can determine $\nu_{1/2}$ with a precision that is bounded by how finely we can program the function generator that produces the RF radiation. This precision is also almost an order of magnitude smaller than the day-to-day drift in the magnetic field. We can set these values very precisely, then, but they only remain accurate for a short period of time.

Because this calibration method is based on observing Feshbach losses over long time periods, it is only effective over small field ranges on either side of resonance. Closer to resonance, losses are too high to tune $\nu_{1/2}$ precisely and further away from resonance, losses are insufficient to dissipate the condensate within a time period of under 150 ms. The approximate viable ranges for direct $\nu_{1/2}$ calibration are shown in Fig. 3.8.

Note the drastically different slopes of the linear fits to the subsets above and below resonance. Theoretically, all eight data points should lie on the same line, and we can calculate what the slope of that line should be. The energies of the $|1,+1\rangle$ and $|2,-1\rangle$ states are given by the Breit-Rabi equation (Eq. 1.17) and the energy splitting between these two states is given by

$$\Delta\nu(B) = \frac{\Delta E_{\mathrm{HF}}}{2h}\left(\sqrt{1+\gamma B+(\gamma B)^2}+\sqrt{1-\gamma B+(\gamma B)^2}\right), \tag{3.42}$$

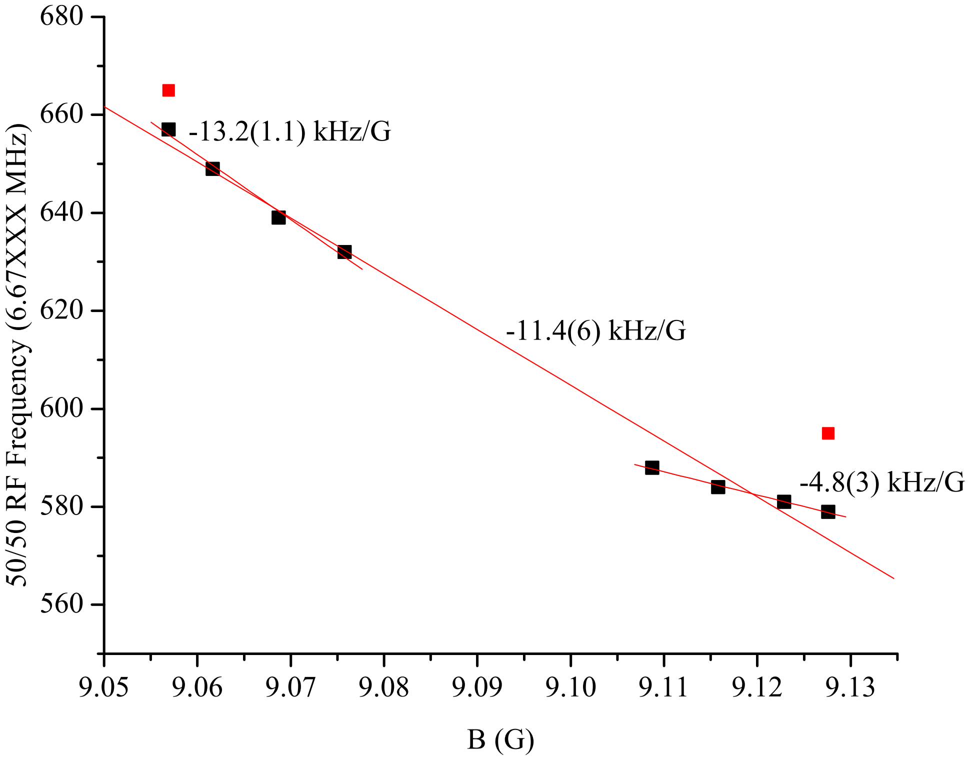

Figure 3.8: Calibrated values of $\nu_{1/2}$ around the Feshbach resonance. The eight points span, to within 5 mG on each side, the viable ranges for direct calibration. Closer in towards resonance, Feshbach losses are too high to provide sufficient signal and further away from resonance, losses are insufficient to dissipate the condensate in under 150 ms. Note the drastically different slopes of the linear fits to the complete data set and to the two subsets. The theoretical value of the slope, calculated from changes in the relative energies of the states given by the Breit-Rabi equation, is -10.6 kHz/G, which is roughly consistent with the slope of the overall fit. The points in red were taken two days after the other points, illustrating how the drift of the ambient magnetic field compounds this problem. At present, our inability to accurately predict $\nu_{1/2}$ over the entire range of the Feshbach resonance presents the largest obstacle to an accurate characterization of the resonance.

with

$$\gamma = (g_J + g_I)\frac{\mu_B}{\Delta E_{\mathrm{HF}}}, \tag{3.43}$$

where, as before, ΔE_{HF} is the hyperfine splitting, g_J and g_I are the Landé g-factors for the total electron and nuclear magnetic moments, and μ_B is the Bohr magneton. Observing the structure of the two-photon transition shown in Fig. 3.4, we see

$$\nu_{\mathrm{RF}}(B) = \nu_{\mathrm{MW}} - \Delta\nu(B), \tag{3.44}$$

where ν_{MW} is assumed to be constant. The change in ν_{RF} is then given by

$$\nu_{\mathrm{RF}}(B) - \nu_{\mathrm{RF}}(0) = \frac{\Delta E_{\mathrm{HF}}}{2h}\left(2 - \sqrt{1 + \gamma B + (\gamma B)^2} - \sqrt{1 - \gamma B + (\gamma B)^2}\right). \tag{3.45}$$

This equation is, to a very good approximation, linear over the small region from 9.00 G to 9.15 G, and its derivative at the Feshbach resonance is

$$\left.\frac{d\nu_{\mathrm{RF}}}{dB}\right|_{9.10\mathrm{G}} = -10.6\mathrm{kHz/G}. \tag{3.46}$$

This value is roughly consistent with the slope of the fit to the entire data set, but it is markedly different from the slopes of either subset.

Our inability to predict $\nu_{1/2}$ accurately throughout the region of the Feshbach resonance is at present the largest obstacle to an accurate characterization of the resonance. The drift in the stray magnetic field further compounds this problem. The red points plotted in Fig. 3.8 were taken two days after the other points, demonstrating the significant magnitude of the drift.

Ideally, we would be able to define a function, which will likely be piecewise with respect to the center of resonance, that accurately predicts $\nu_{1/2}$ at all points in the region of resonance. By measuring one or two points at the beginning of each day or periodically throughout the day, we would be able to shift the function in some predetermined way and preserve its accuracy. Until significant progress is made in this direction, our measurements of Feshbach losses will be heavily skewed by variable initial populations of the two states.

3.5 Resonance Mapping

For a first rough attempt to map the Feshbach resonance using the transfer-at-field method, we tried using a single linear fit to determine $\nu_{1/2}$ for all fields across resonance. This data set is plotted in Fig. 3.9 with a theoretical fit to $\text{Im}(a)$ (Eq. 3.36).

The most striking characteristic of the data is the apparent asymmetry of the resonance. Although a close fit to $\text{Im}(a)$ is allowed by the $\sin(2\phi_R)(B - B_0)$ term in Eq. 3.37, it is more likely that this asymmetry is the result of a systematic experimental error. With the exception of sets like the one plotted in Fig. 3.6 that were taken by sweeping the field in only one direction, neither the data we took using the ramp-to-field method nor the findings [50, 51] of other groups display a similar trend. These other groups explored the same resonance in condensates of ^{87}Rb atoms using the ramp-to-field method [50]

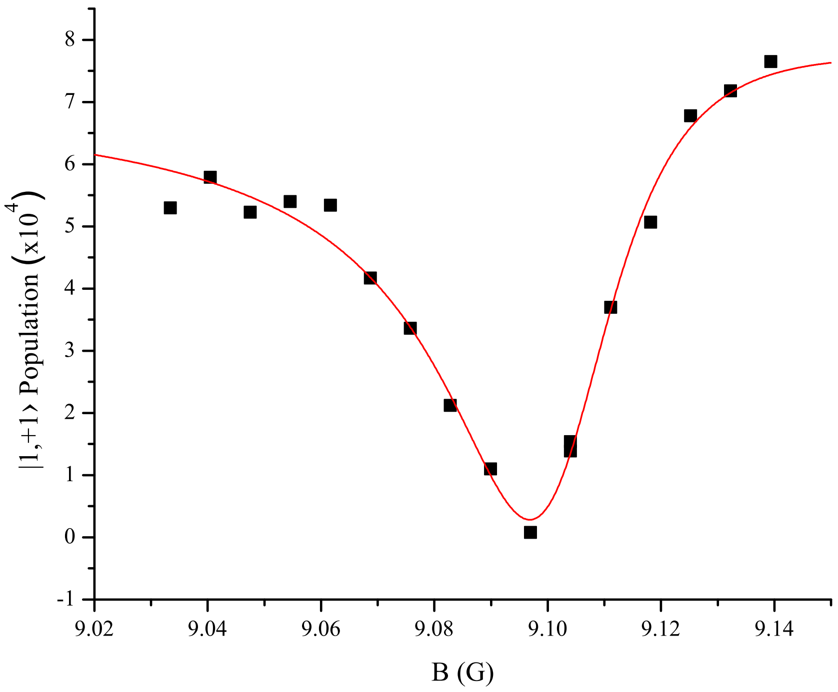

Figure 3.9: Plot of the Feshbach resonance taken using the transfer-at-field method, with a fit to Im(a). We slowly ramp the field to the desired value, perform the two-photon pulse, and allow the condensate to evolve for 2.0 ms before dropping and imaging it. Note both the apparent asymmetry of the resonance and the lack of noise in the data. Although these data can be fit closely to Im(a), which is proportional to the Feshbach loss rate, this asymmetry is consistent neither with other trials conducted using the ramp-to-field method nor with other groups' findings [50, 51]. More likely, this asymmetry is a result of our use of inaccurate values of $\nu_{1/2}$ when performing the two-photon pulse.

	Data Fit	Erhard, Im(a)	Widera, Re(a)	Widera, Im(a)
B_0 (G)	9.105(1)	9.09(1)	9.128(9)	9.121(9)
ΔB_{inel} (mG)	36(3)	26-43	30(8)	40(10)
ϕ_R	0.26(3)	0	0	0

Table 3.1: Feshbach resonance parameters. Our experimental values are extracted from fitting the data plotted in Fig. 3.9 and the reference data are extracted from the measurements of Feshbach loss rates (Im(a)) and the magnitude of the scattering length (Re(a)) made by Erhard et al. [50] and Widera et al. [51].

and by trapping pairs of atoms in an optical lattice potential [51].

As mentioned in the previous section, this systematic error probably stems from our inability to accurately calibrate the two-photon pulse around resonance to achieve equal initial populations. Using the two-photon calibration data in Fig. 3.8 as an example, if we were to use the slope of -11.4 kHz/G to calculate $\nu_{1/2}$ when we should actually be using -4.8 kHz/G, then our predicted $\nu_{1/2}$ would fall with respect to the actual value as the field increases and the relative proportion of $|1, +1\rangle$ atoms would rise. This theory is further supported by the fact that the data only seem to skew noticeably upward above resonance, where we should hypothetically use -4.8 kHz/G instead of -11.4 kHz/G, and not below resonance, where we should use -13.2 kHz/G.

Despite the asymmetry, however, fitting the data to Eq. 3.36 provides us with values and uncertainties for B_0, ΔB_{inel}, and ϕ_R, which are listed in Table 3.1. Because the Feshbach losses are merely proportional to Im(a), however, we cannot use this experiment to determine a_{bg} or ΔB_{el}. We can compare these extracted values to those found by Erhard et al. [50] and Widera et al. [51]. Erhard uses a method that is very similar to ours to measure the loss rate. They measure two-body Feshbach losses of pairs of atoms trapped in an two-dimensional optical lattice potential. The key difference between this procedure and ours is that they measure two-body losses between individual pairs of atoms in distinct lattice sites whereas we measure two- and three-body losses within the whole condensate. They also use a Ramsey interferometer to measure the magnitude of the scattering length of the atoms. The measurement of loss rates produces a Lorentzian distribution and the measurement of the interspecies scattering length produces a dispersion curve. Comparing the general forms of these two functions to our expressions for $\mathrm{Re}(a)$ and $\mathrm{Im}(a)$, we find that they set $\phi_R = 0$ and give peak widths that are equal to $\Delta B_{\mathrm{inel}}/2$.

These extracted values are listed in Table 3.1 alongside our own. Our value for ΔB_{inel} is consistent with their findings, but our magnetic field calibrations evidently are in disagreement. We use these parameters to plot in Fig. 3.10 the real and imaginary parts of the complex scattering length, as predicted by our data and by Widera. One can easily see the discrepancy in the magnetic field calibration and the agreement on peak width, but notice also the asymmetry of our experimental plots. This is a direct result of the asymmetry in our data and is manifested mathematically in the non-zero value of ϕ_R. Thus, as stated in the previous section, this asymmetry and the factors that cause it are the largest obstacles to a detailed and accurate

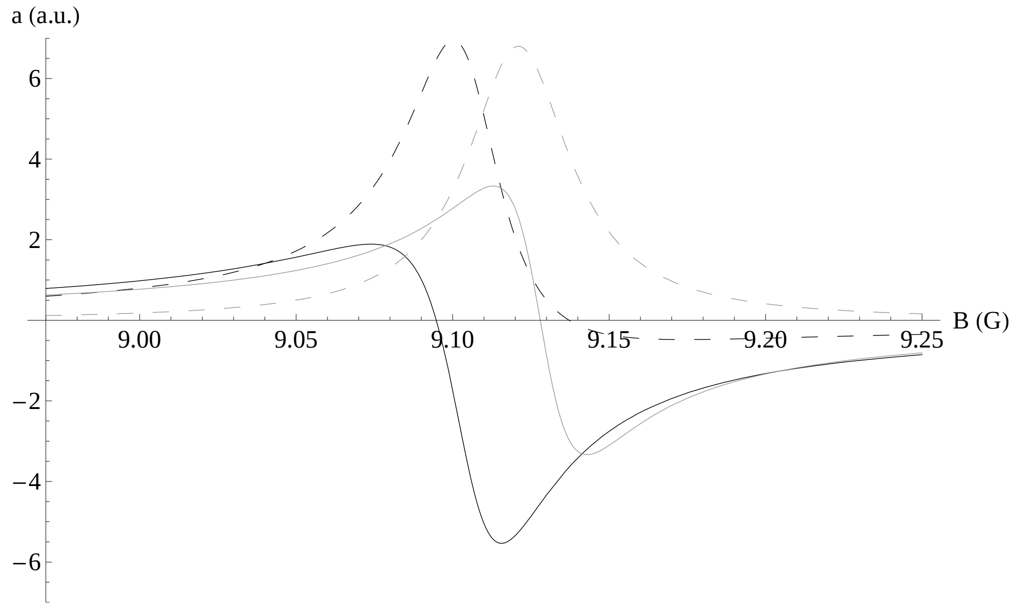

Figure 3.10: Theoretical plots of the real (solid) and imaginary (dashed) parts of the complex scattering length around the 9.1 G interspecies Feshbach resonance. For these plots, we use parameters extracted from our initial mapping of the resonance (black) and from Widera et al. [51] (grey), which are listed in Table 3.1. Because the scaling of each function cannot be determined directly from the data interpretation, all are scaled in arbitrary units and re-centered on $a = 0$.

picture of the behavior of the interspecies scattering length near resonance.

3.6 Time Evolution

We can, however, observe large changes in the interspecies scattering length more directly. Because the coupled Gross-Pitaevskii equations that describe the binary condensate have both inter- and intraspecies scattering terms, the behavior of the system is critically dependent on the relative values of the inter- and intraspecies scattering lengths. We can define a critical value of $|a_{12}|$, the magnitude of the interspecies scattering length, above which the condensates cannot spatially coexist [61]:

$$|a_{12}^{\mathrm{cr}}| = \sqrt{a_{11}^2 + a_{22}^2}. \tag{3.47}$$

If $a_{12} < -a_{12}^{\mathrm{cr}}$, then attraction between the two species overwhelms repulsion between the atoms of each species and the condensate collapses. If $a_{12} > +a_{12}^{\mathrm{cr}}$, then repulsion is stronger between atoms of different species than between atoms of the same species and the components spatially separate.

The latter case has been extensively studied in our lab by Mertes et al. [33]. Refining an earlier experiment by Hall et al. at JILA [62], they studied the interspecies interactions in a binary condensate composed of atoms in the $|1,-1\rangle$ and $|2,+1\rangle$ states and observed a complex series of interpenetrating ringlike structures that oscillate in time. By comparing the observed component separation patterns to the results of a numerical simulation calculated using a multi-component mean-field model, they were able to conclude that motional damping is not intrinsic to the process of component separation, an important result for the study of binary superfluids. The primary difference between this experiment and our current investigation is their use of a magnetic trap instead of an optical trap. This provides them with a more harmonic potential but limits them to the magnetically trappable $|1, -1\rangle$ and $|2, +1\rangle$ states. These states do not exhibit as accessible a Feshbach resonance as the one we are currently investigating, so the scattering lengths involved in this prior experiment were fixed at $a_{11} = 100.40a_0$, $a_{22} = 95.00a_0$, and $a_{12} = 97.66a_0$ and accordingly, the condensate was found to be unstable with respect to component separation.

Our current investigation of the interspecies Feshbach resonance enables us to examine the time evolution of the system while varying the interspecies scattering length. Because of Feshbach losses near the center of resonance, we will not be able able to observe time evolution with the scattering length set at its extreme values. Preliminary evidence suggests, though, that we can alter the scattering length enough to lower it below a_{12}^{cr} and change the binary condensate from miscible to immiscible. Figure 3.12 shows the result of an extensive observation of the time evolution of both states at fields above and below resonance. For this experiment, we slowly ramp the field to either $B_{-} = 9.058$ G or $B_{+} = 9.128$ G and apply the two-photon pulse for 700

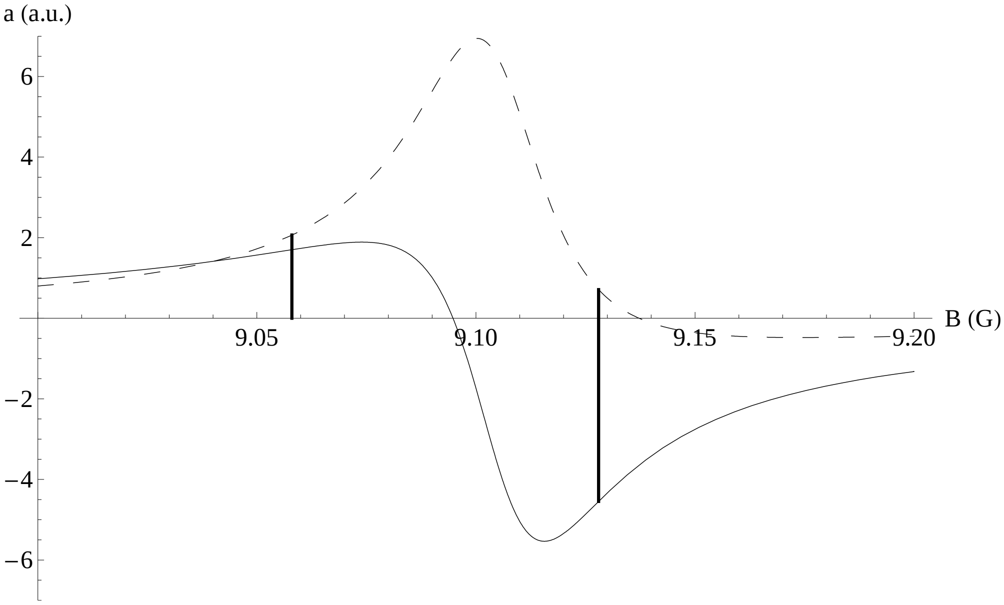

Figure 3.11: Fields used for time evolution observation with respect to resonance. Note the drastically different theoretical values of Re(a) (solid function) at $B_{-} = 9.058$ G (left vertical line) and $B_{+} = 9.128$ G (right vertical line). Note also that the values of Im(a) (dotted function) are slightly different at the two fields because of the plot's asymmetry. This should result in different loss rates at the two fields, which the data shown in Fig. 3.12 do not reflect. If the plot were more symmetric, as we believe it should be, then the values of Im(a) would be roughly equal for the two fields and the values of Re(a) would still be drastically different. The time evolution data in Fig. 3.12 appear to offer further confirmation of the inaccuracy of the skewed data.

μs at field. The values of these fields with respect to our experimentally determined Feshbach resonance are shown in Fig. 3.11. We then allowed the condensate to evolve for a given duration of time before dropping it from the optical trap and imagining it using side-view imaging. Here, the convenience of the transfer-at-field method is particularly apparent; the short duration of the two-photon pulse notwithstanding, the time evolution of the binary condensate and the Feshbach resonance both have the same precisely defined $t = 0$.

These data possess several interesting features that should be highlighted and commented on. First, the $|1, +1\rangle$ atoms, particularly those at B_-, exhibit ringlike structures that persist approximately from 2.0 ms to 5.0 ms, which is qualitatively similar to the oscillating rings observed by Mertes et al. For clarity, this images are enlarged in Fig. 3.13. Also notice in this figure the marked difference between the formation of rings at the two different field values. Below resonance, the $|1, +1\rangle$ atoms quickly coalesce in the center of the condensate and form a clearly defined ring. Above resonance, in contrast, the spatial distribution of the atoms is more diffuse and almost appears to be the inverse of the spatial distribution below resonance. These results are consistent with the interspecies scattering length being higher below resonance than above it, as predicted by theory and by our plot of the resonance shown in Fig. 3.3.

The emergence and disappearance of these ringlike structures between 2.0 ms and 5.0 ms give the impression of periodicity, even though rings distinct

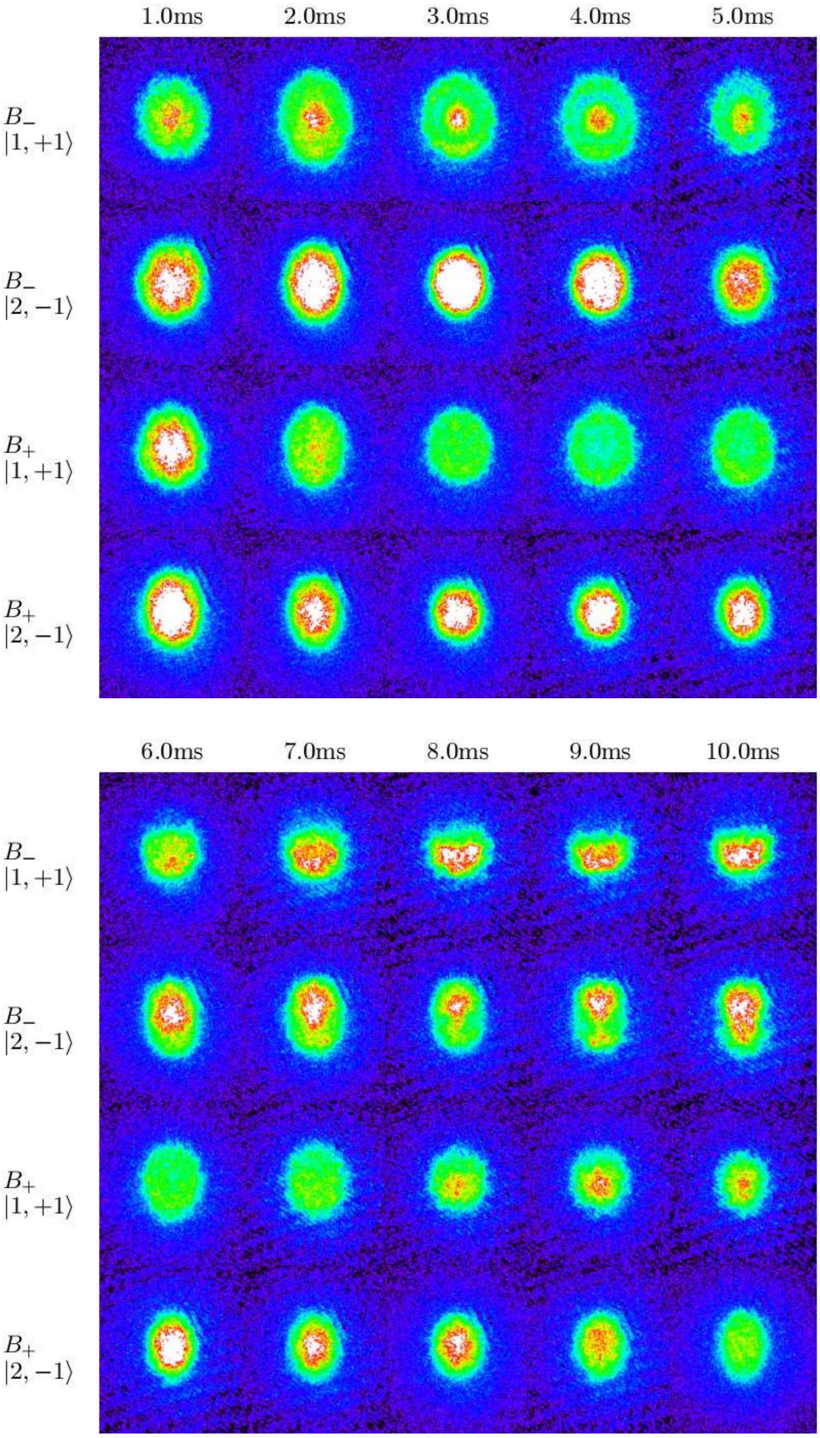

Figure continued on following page

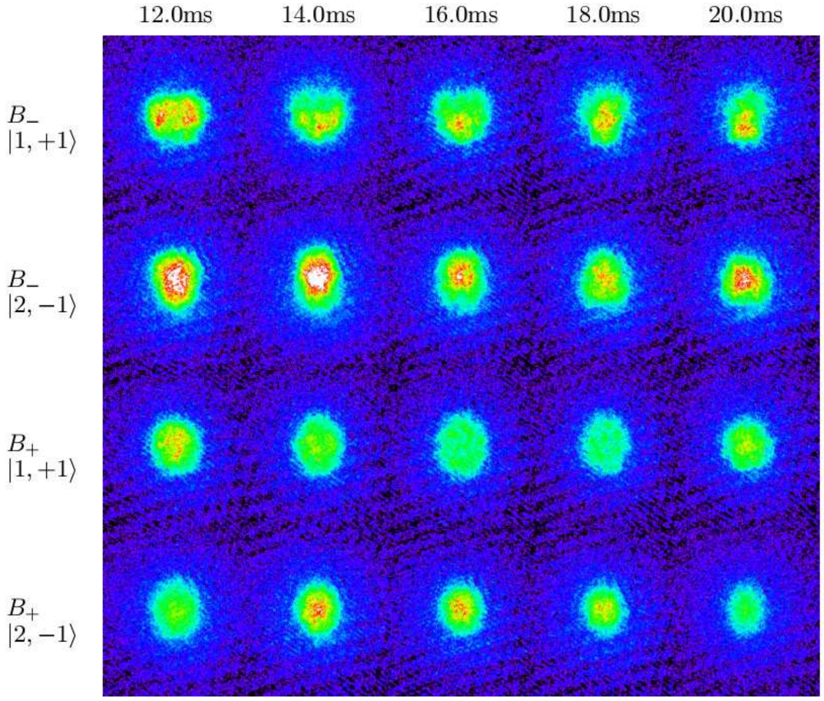

Figure 3.12: Co-evolution of $|1,+1\rangle$ and $|2,-1\rangle$ condensates near a Feshbach resonance. The fields observed are $B_- = 9.058$ G and $B_+ = 9.128$ G, and the resonant field is 9.102 G. The comprehensive set of data is presented here to provide a complete illustration of the behavior of the binary condensate above and below resonance. Various features are highlighted in subsequent figures and analyzed in the text.

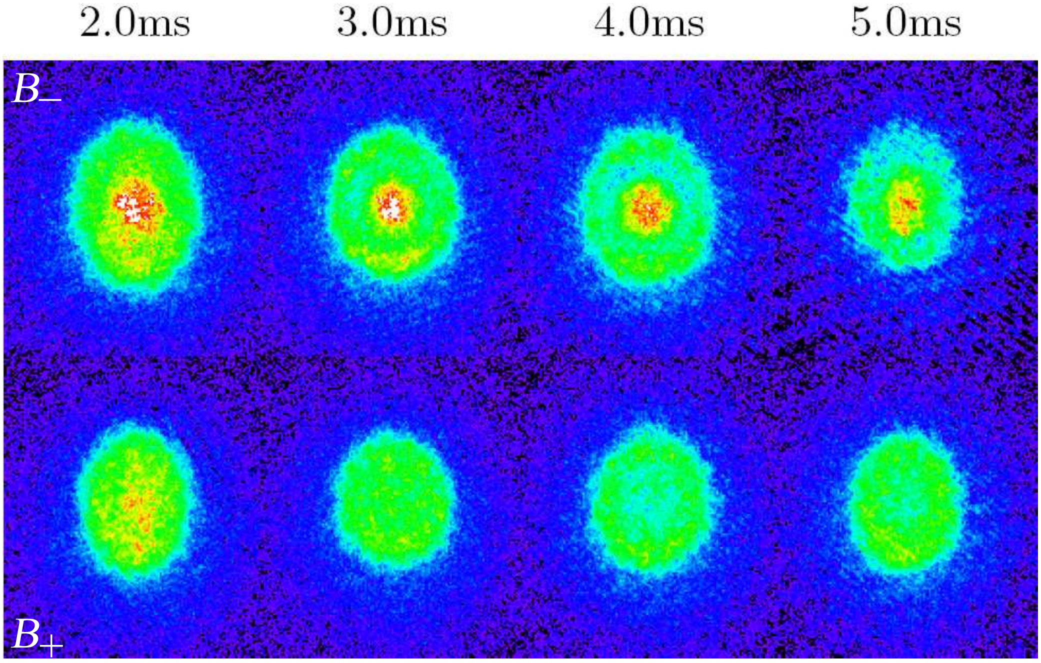

Figure 3.13: Ringlike structures observed in the $|1, +1\rangle$ state. Note the high central density and sharp ring definition of the atoms below resonance and the diffuse distribution of the atoms above resonance. This distinction is consistent with the scattering length being increased at fields below resonance and decreased at fields above it, as theory predicts. Note also that the spatial distribution above resonance appears to be the inverse of the spatial distribution below resonance, but this could simply be the result of there being fewer atoms in the $|1, +1\rangle$ state relative to the $|2, -1\rangle$ state at B_+.

enough to be observed by side-view imaging appear only once in the scope of this data set. One imagines two possible reasons for this single appearance of ringlike structures. First, our binary condensate might experience a motional damping that was absent in the Mertes experiment, which could quickly suppress the oscillations of our ringlike structures and prevent them from appearing a second time. Such damping could possibly arise from the increased rate of inelastic collisions caused by the Feshbach resonance. Additionally, the optical trap is far more anharmonic than the TOP trap, so the condensate could oscillate with different frequencies along the different axes of the trap. In this case, the coherent excitation of the entire binary condensate would be damped by being divided into components that are out of phase with one another.

The second explanation is that the oscillating process of ring formation continues at times beyond 5 ms but we simply cannot see it. We use side-view imagining in this experiment, which gives the view of a condensate from the perspective of the $-\hat{\mathbf{y}}$ direction. The axes of symmetry for both the magnetic and optical traps, however, is vertical, and this is the axis along which Mertes et al. imaged their binary condensates. Figure 3.14 shows examples of evolving component separation below resonance, where we have predicted the condensate to be immiscible. The spatial distributions of the atoms evolves in time and generally exhibits symmetry about the vertical axis. As Fig. 3.15 demonstrates, it is possible that these condensate components would exhibit evolving cylindrical symmetry, in accordance with

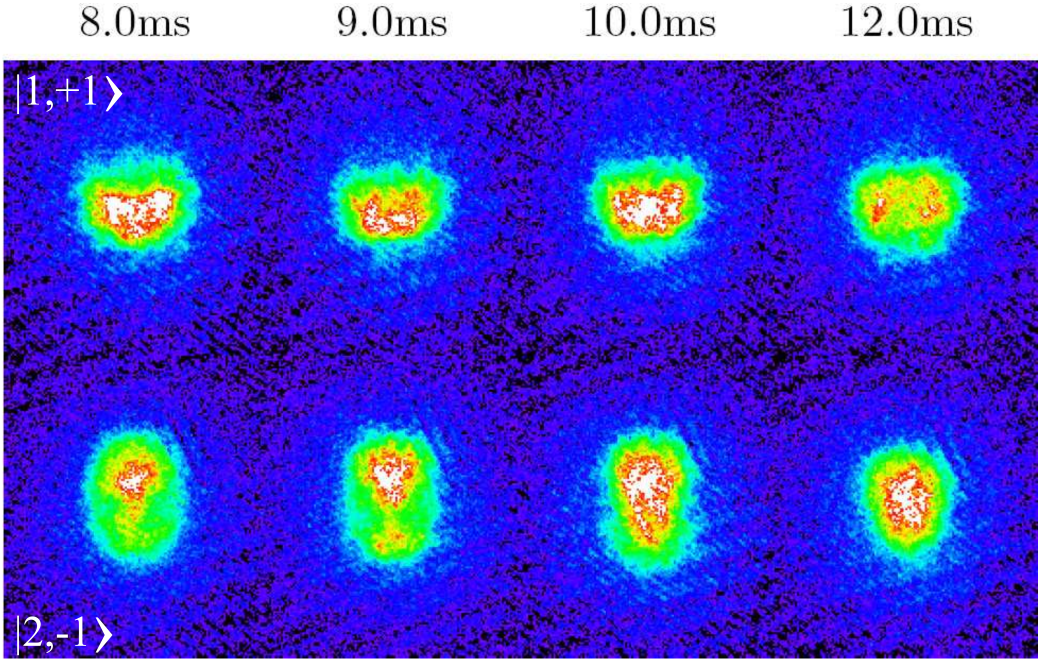

Figure 3.14: Spatial separation of a binary condensate below the Feshbach resonance. This figure shows images of the $|1,+1\rangle$ and $|2,-1\rangle$ components as viewed from the $-\hat{\mathbf{y}}$ direction. Note the complementary evolving spatial distributions of the two populations. As demonstrated by the numerical simulations of the time evolution of the $|1,-1\rangle$ and $|2,+1\rangle$ states shown in Fig. 3.15, it is possible that these data, which exhibit symmetry about the vertical axis, would exhibit radial symmetry when viewed from below.

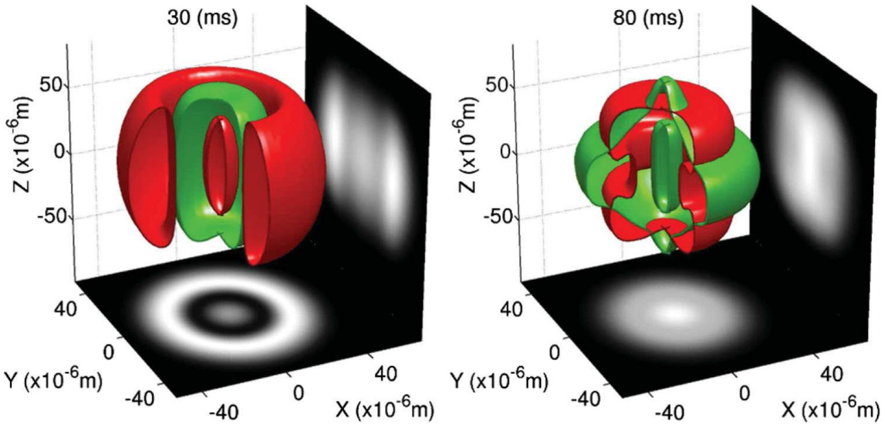

Figure 3.15: Numerical simulation of time evolution. These numerical simulations performed by Mertes et al. display three-dimensional density distributions of the $|1,-1\rangle$ (red) and $|2,+1\rangle$ (green) states at two different evolve times, as well as simulated top-view (bottom) and side-view (right) images of the $|1,-1\rangle$ state. They demonstrate that spatial distributions that exhibit radial symmetry when imaged using top-view imaging exhibit planar symmetry about the vertical axis when imaged using side-view imaging.

the findings of Mertes et al. Notice in Fig. 3.12 that during this time period (8.0 ms to 12.0 ms), the binary condensate above resonance shows no signs of component separation or non-equilibrium dynamics, which further confirms that the change in scattering length between the two sides of resonance is significant enough to affect the immiscibility of the condensate.

These data, however, are only a first step in this investigation and there are three improvements that should be made for a future study of this topic. First, steps should be taken to avoid imaging saturation. Although saturation could be avoided by detuning the imaging beam from resonance, this procedure results in lensing. Implementing the procedure used by Mertes et al. would be preferable and would result in more accurate data. To image the $|1,-1\rangle$ state, they apply resonant radiation to remove the $|2,+1\rangle$ atoms and then apply a brief two-photon pulse to transfer a small proportion of $|1,-1\rangle$ atoms into the $|2,+1\rangle$ state. This small proportion can then be imaged on resonance, without lensing or saturation. To image the $|2,+1\rangle$ atoms, they perform this same procedure after a population-inverting two-photon pulse. Second, we should begin imaging the condensates using top-view imaging. We can deduce the possibility of ringlike structures oscillating about the vertical axis from these preliminary data, but we would like to observe them directly. If these structures are observed to be periodic, we could then increase the time scale over which we observe the condensate. These procedures have already been optimized and used in our apparatus, so implementing them for this experiment should be relatively simple.

The second improvement will be both easier and more difficult to implement. In order to study more precisely how the change in the scattering length affects the condensate's time evolution, we need to know more accurately how the scattering length changes around resonance. As stated earlier, this is already a primary goal for this ongoing investigation and hinges on a better understanding of how $\nu_{1/2}$ varies around resonance. Once we have taken more reliable data and plotted more accurate scattering length curves, it will be easy to select fields that optimize the trade-off between more significant changes in the scattering length and greater Feshbach losses.

These two experiments are a promising first step in our investigation of the

9.1 G interspecies Feshbach resonance. Both the measurements of Feshbach losses and the observations of the binary condensate's time evolution have provided results that are roughly consistent with what we would expect or what has been observed by other groups. More importantly, though, their inaccuracies have provided suggestions for the future direction of this research. They have demonstrated that the transfer-at-field method has the potential to enable a highly precise measurements of this Feshbach resonance when calibrated correctly. From this will hopefully follow the ability to conduct a detailed study of the dependence of the binary condensate's non-equilibrium dynamics on the interspecies scattering length.

Chapter 4

Conclusion

Here, we will summarize the suggestions for future research that we have laid out throughout this thesis, grouped by chapter and arranged roughly in order of descending immediacy or interest. This ordering, however, is mostly subjective and sometimes arbitrary, so each of these topics should be considered a promising subject for future endeavors.

Spinor Condensates

Stray Magnetic Field Gradients

Because the stray magnetic field gradients exert a difference force on each of the components of a spinor condensate, they will hamper any attempt to study the time evolution of a spinor condensate. The first step in our effort to nullify these gradients should be an extensive study of the existing gradients along the lines of the experiment outlined in Section 2.4.1. This future study should take efforts to maximize the sharpness of the component separation so as to be able to determine the direction of the separation axis more clearly. These efforts might include adjusting the amount of time for which the spinor condensate is allowed to evolve or somehow increasing the interspecies repulsion. Also, this experiment should be repeated periodically to determine the day-to-day drift, if any, of these gradients.

Once the magnitude of the problem has been determined, an appropriate solution can be decided upon. When the upgrades to the bias coil controls mentioned in Section 1.4.2 have been implemented, we should be able to cancel arbitrary divergence gradients exactly. In Section 2.4.2, we have proposed a configuration, consisting of four coils placed every 90° around the cell, that should cancel one of the three independent mixed field gradients exactly. The technical complications involved in constructing three such configurations in the already-crowded space around the science cell might, however, outweigh the benefits to be gained. Possible compromises include using two coils instead of four for each axis, constructing larger coil configurations further away from the science cell, or concentrating on nullifying the gradients along only one or two axes.

Vortices and Atom Lasers

As mentioned in the introduction to Chapter 2, a ferromagnetic spinor condensate like ours is capable of supporting metastable Skyrmion vortices. A study of these coreless vortices would provide interesting contrast with past and ongoing studies of regular vortices. We could also study the co-evolution of vortices in the three components of a spinor condensate and observe coupling between spin gradients and superfluid flow [63]. By applying Stern-Gerlach gradients to a spinor condensate in a weak optical trap, we could selectively out-couple one or both of the $|1, -1\rangle$ or $|1, +1\rangle$ components. This would create an atom laser consisting of selected spin components or even alternating spin components.

A potentially more interesting experiment, however, does not involve spinor condensates at all. As described in Section 2.5, we hope to be able to observe a single vortex core propagating in an atom laser. By imaging successive cross-sections of the atom stream, we would be able to non-destructively observe the evolution of a single vortex in one condensate at multiple times.

Field Sweep Pathology

As described in Section 2.2.1, a Landau-Zener magnetic field sweep fails to transfer any atoms from the $|1, -1\rangle$ state when certain ramp times are used. This hints at a possible pathology in the equipment we use to create these magnetic fields. The fact that this pathology has, to our knowledge, only manifested itself in this way both emphasizes and lessens the importance of studying it. On one hand, it is important to understand our apparatus as completely as possible, especially if we encounter a problem of which we were previously unaware. Solving this problem, then, could result in unanticipated improvements to the apparatus' performance. On the other hand, though, the fact that we were not aware of this problem until this point seems to argue against this pathology being a very fundamental problem. By using both the field sweep and frequency sweep methods, we effectively have full Landau-Zener functionality.

Feshbach Resonance

Asymmetry in Loss Rate Data

Our measurement of the condensate loss rate due to resonance described in Section 3.5 is the basis of our characterization of the interspecies Feshbach resonance. The asymmetry inherent in this data results in a skewed theoretical prediction of how the interspecies scattering length varies around resonance. Since two of the following topics involve studying the effects of changing the scattering length, a more precise theoretical prediction is necessary. Further research should also be conducted to understand more fully exactly how the two- and three-body loss rates vary around resonance.

In Section 3.3, we hypothesize that this asymmetry is caused by an inaccurate calibration of the two-photon pulse at fields close to resonance. If we could accurately interpolate $\nu_{1/2}$ over the region of resonance, then we believe that the accuracy of the data would be greatly improved. Suggestions for determining $\nu_{1/2}$ more accurately include constructing a piecewise function that allows $\nu_{1/2}$ to vary differently on each side of resonance and determining how this interpolation function shifts due to the day-to-day magnetic field drift.

Time Evolution of Binary Condensate

Improvements in our observation of the time evolution of a binary condensate should follow naturally from a more accurate understanding of how the scattering length and loss rates vary around resonance. With this knowledge, we will be able to optimize the balance between retaining a condensate for a substantial period of time and subjecting it to widely different values of the scattering length. More immediately, though, we should begin observing the time evolution using top-view imaging. We could first detune the probe beam from resonance to compensate for saturation, but we ultimately want to use microwave imaging, the method described near the end of Section 3.6.

Vortices Near Feshbach Resonance

A more accurate understanding of the scattering length would also allow us to study how interatomic interactions affect the evolution of vortices in a binary condensate. Specifically, we are interested to know how vortices might evolve differently in a miscible binary condensate compared to an immiscible one. We could also test the prediction [64] that non-overlapping vortex lattices in the two components moderate the tendency of an immiscible binary condensate to component-separate.

Intraspecies Feshbach Resonance

As mentioned in the introduction to Chapter 3, a number of Feshbach resonances have been predicted [48] and observed [49] for atoms in the $|1, +1\rangle \otimes |1, +1\rangle$ entrance channel at fields between 0.5 and 1260 G. We could measure the loss rates of many of these resonances without having to calibrate the two-photon transition. We should even be able to perform a Landau-Zener field sweep at a magnetic field close to the resonance of interest. In addition to the loss rate experiment, we could make the scattering length negative and observe condensate collapse [65, 66] or the formation of solitons [54] as the condensate propagates back and forth along a single FORT beam.

Appendix A

Modeling the Optical Trap

To aid in understanding and characterizing the crossed-beam FORT, we found it helpful to write a numerical model in Mathematica$^{\text{TM}}$ to simulate the trap's potential. We recommend reading Daniel Guest's thesis [4] on the construction and alignment of this trap so that this theoretical derivation can be placed in an experimental context.

A.1 Theory

A.1.1 Optical Dipole Potential

For a derivation of the optical potential, we follow the example given by Pethick and Smith [30], with one minor difference; as explained later, we will introduce a factor of $^1/_2$ into the definition of the oscillating electric field in order to make the definition of the Rabi frequency consistent with how it is used elsewhere in this thesis. Since we are modeling an atom as an electric dipole, the interaction of the atom with an static external electric field is given by

$$H' = -\mathbf{d} \cdot \mathbf{E} \tag{A.1}$$

where $\mathbf{d}$ is the electric dipole moment operator and $\mathbf{E}$ is the electric field vector. The second-order perturbation of the ground state energy of the atom is given by

$$\Delta U_g = -\sum_e \frac{|\langle e|\mathbf{d} \cdot \mathbf{E}|g\rangle|^2}{E_e - E_g}, \tag{A.2}$$

where g and e respectively represent the ground and excited states, E_e and E_g represents those states' energies, and the summation is performed over all excited states. If we define the atomic polarizability

$$\alpha = 2\sum_e \frac{|\langle e|\mathbf{d} \cdot \hat{\mathbf{e}}|g\rangle|^2}{E_e - E_g}, \tag{A.3}$$

where $\hat{\mathbf{e}}$ is a unit vector parallel to the electric field, then the change in energy of the ground state is simply given by

$$\Delta U_g = -{}^1\!/_2\alpha E^2. \tag{A.4}$$

By Earnshaw's Theorem, we know that we cannot create an electrostatic field maximum in free space, so we cannot trap atoms using static electric fields alone. Therefore, we must generalize to the time-dependent electric field represented by

$$\mathbf{E}(t) = {}^1\!/_2(\mathbf{E}_0 \mathrm{e}^{-i\omega t} + \mathbf{E}_0^* \mathrm{e}^{i\omega t}). \tag{A.5}$$

Equation A.4 then becomes

$$\Delta U_g = -{}^1\!/_2 \alpha(\omega) \langle E(t)^2 \rangle = -\frac{1}{4}\alpha(\omega)|E_0|^2, \tag{A.6}$$

where $\langle E(t)^2 \rangle$ is the mean-squared time average of the electric field and is equal to ${}^1\!/_2|E_0|^2$. The atomic polarizability, which is now dependent on the frequency, is given by

$$\alpha(\omega) = \sum_e |\langle e|\mathbf{d}\cdot\hat{\mathbf{e}}|g\rangle|^2 \left(\frac{1}{E_e - E_g - \hbar\omega} + \frac{1}{E_e - E_g + \hbar\omega} \right), \tag{A.7}$$

which has the $\pm\hbar\omega$ terms added in to represent the energy of the incident photons. At this point, it is helpful to define the resonant frequency $\omega_e = (E_e - E_g)/\hbar$, which in turn enables us to define $\Delta_e = \omega_e - \omega$, the detuning of the laser from resonance, and $\Delta'_e = \omega_e + \omega$, which does not have as obvious a physical significance. Thus, in terms of Δ_e and Δ'_e, the polarizability becomes

$$\alpha(\omega) = \sum_e |\langle e|\mathbf{d}\cdot\hat{\mathbf{e}}|g\rangle|^2 \left(\frac{1}{\hbar\Delta_e} + \frac{1}{\hbar\Delta'_e} \right) \approx \sum_e \frac{|\langle e|\mathbf{d}\cdot\hat{\mathbf{e}}|g\rangle|^2}{\hbar\Delta_e}. \tag{A.8}$$

Here, in order to simplify the derivation somewhat, we assume that the laser frequency is close to resonance and that $\Delta'_e \gg \Delta_e$. Since our trapping laser is actually far off-resonance, this is a poor approximation but we will address and correct for this problem at the end of the derivation.

Next, we must take into account the finite lifetimes of the ground and excited states. This is done by adding an imaginary term of $-i\hbar\Gamma_e/2$, where $\Gamma_e = 1/\tau_e$ is the decay rate of the excited state, to the energy of the excited state. The polarizability, now a complex quantity, is given by

$$\alpha(\omega) = \sum_e \frac{|\langle e|\mathbf{d}\cdot\hat{\mathbf{e}}|g\rangle|^2}{\hbar(\Delta_e - i\Gamma_e/2)}. \tag{A.9}$$

Equation A.6 then must also be complex, becoming

$$\Delta U_g - i\hbar\Gamma_g/2 = -\frac{1}{4}\alpha(\omega)|E_0|^2. \tag{A.10}$$

The real part ΔU_g corresponds to the change in energy of the ground state while the imaginary part $\hbar\Gamma_g/2$ corresponds to the finite lifetime of the ground state due to transitions to the excited state e. Taking the real part of both sides, we find

$$\Delta U_g = \sum_e \frac{\Delta_e|\langle e|\mathbf{d}\cdot\mathbf{E}|g\rangle|^2}{4\hbar(\Delta_e^2 + (\Gamma_e/2)^2)} \tag{A.11}$$

Here, we can define the Rabi frequency

$$\Omega = |\langle e|\mathbf{d}\cdot\mathbf{E}_0|g\rangle|/\hbar. \tag{A.12}$$

When a system with two non-degenerate energy states is exposed to resonant radiation, the competing processes of absorption and stimulated emission will cause the system to oscillate between the two states at the Rabi frequency. Herein lies the discrepancy between our derivation and the example we are following. The oscillating proportional population of one state can be represented by

$$|c(t)|^2 = \sin^2(\Omega' t) = {}^1\!/_2\big(1 + \cos(\Omega t)\big), \text{ with } \Omega = 2\Omega'. \tag{A.13}$$

We define the Rabi frequency as Ω, whereas Pethick and Smith use Ω'. From Eq. A.12, we see that $|E_0|$ must also be twice as large under our definition, so we simply insert the factor of ${}^1\!/_2$ into Eq. A.5 to compensate. By doing this, we come into agreement with another derivation that shares our definition of the Rabi frequency [67].

We can also define a saturation intensity I_{sat} such that when the intensity I of the radiation is equal to I_{sat}, 1/4 of the population is in the excited state. In terms of known quantities, this relation is represented by

$$\frac{I}{I_{\text{sat},e}} = 2\left(\frac{\Omega}{\Gamma_e}\right)^2 \tag{A.14}$$

Substituting Eqs. A.12 and A.14 into Eq. A.11, we find

$$\Delta U_g = \frac{\hbar}{2}\sum_e \frac{\Delta_e(I/I_{\text{sat},e})}{1 + (2\Delta_e/\Gamma_e)^2}. \tag{A.15}$$

	D$_1$: $5^2\mathrm{S}_{1/2} \rightarrow 5^2\mathrm{P}_{1/2}$	D$_2$: $5^2\mathrm{S}_{1/2} \rightarrow 5^2\mathrm{P}_{3/2}$
λ	795.0 nm	780.2 nm
Γ	36.10(5) MHz	38.11(6) MHz
I_{sat}	4.484(5) mW/cm^2	2.503(3) mW/cm^2

Table A.1: Optical trap parameters

For our experimental parameters, shown in Table A.1, the $(2\Delta_e/\Gamma_e)^2$ term in the denominator is on the order of 10^{15}. Therefore, Eq. A.15 can reasonably be simplified to

$$\Delta U_g = \frac{\hbar}{8} \sum_e \frac{\Gamma_e^2 I}{\Delta_e I_{\mathrm{sat},e}} \tag{A.16}$$

Now, we can add a correction for the on-resonance approximation that was made earlier in Eq. A.8. The percentage discrepancy between the precise and approximate expressions in Eq. A.8 is equal to $\frac{1}{2}(1-\lambda/\lambda_e)$, where λ and λ_e are respectively the laser wavelength and the resonant wavelength for the transition between the ground state and the excited state e. This is therefore a good approximation near resonance but our trap uses a far off-resonance beam and the discrepancy is approximately 15% for the parameters shown in Table A.1. Because ΔU_g is linear with respect to $\alpha(\omega)$, the remainder of the derivation after Eq. A.8 follows for the neglected Δ'_e term as it did for the Δ_e term, and we find for a final expression

$$\Delta U_g = \frac{\hbar}{8} \sum_e \frac{\Gamma_e^2}{I_{\mathrm{sat},e}} \left(\frac{1}{\Delta_e} + \frac{1}{\Delta'_e} \right) I \tag{A.17}$$

For ^{87}Rb, this sum in Eq. A.17 is over the two optical transitions, the D$_1$

transition from the ground state $5^2S_{1/2}$ to $5^2P_{1/2}$ and the D_2 transition to $5^2P_{3/2}$ shown in Fig. 1.2(b), that arise because of the fine-structure doublet in the 5P sublevel. All quantities in Eq. A.17 that are properties of these two transitions are constants that have been experimentally determined [25] and are displayed in Table A.1. Therefore, the change in energy of the ground state, and hence the trapping potential, is simply proportional to the intensity of the laser at any given point.

A.2 Numerical Modeling

To calculate the optical intensity, we define a system of axes that is neither consistent with the standard lab definition as illustrated in Fig. 1.3 nor with the standard optical definition in which light propagates in the $+\hat{\mathbf{z}}$-direction. We define $+\hat{\mathbf{x}}$ as the direction of propagation of the FORT-X beam, and $+\hat{\mathbf{y}}$ as the direction of propagation of the FORT-Y beam. To define these axes explicitly with respect to the lab frame, $+\hat{\mathbf{x}}$ is defined as south-west and $+\hat{\mathbf{y}}$ as south-east. These definitions require $+\hat{\mathbf{z}}$ to be defined as upward, contrary to the lab definition. This allows us to calculate the intensity of FORT-X, for which $\hat{\mathbf{x}}$ is the axial direction and $\hat{\mathbf{y}}$ and $\hat{\mathbf{z}}$ are radial directions, and transfer the result to FORT-Y by switching the x and y indices.

This is a brief overview of the Gaussian optics involved in modeling the FORT, less of a derivation than a presentation of the formulae used. For a far more extensive and rigorous treatment of the subject, we would recommend

Daniel Guest's thesis [4], from which these formulae were derived. Since the FORT-X beam has a circular Gaussian intensity profile, its intensity at a given point (x, ρ_x) is given by

$$I(x, \rho_x) = \frac{2P}{\pi w(x)^2} \exp(-2\rho_x^2/w(x)^2), \tag{A.18}$$

where P is the beam power, $w(x)$ is the beam radius at an axial distance x from the beam waist, and $\rho_x = \sqrt{y^2 + z^2}$ is the radial distance from the center of the beam. The beam radius $w(x)$ is defined as the distance from the beam axis at which the intensity is reduced by a factor 1/e from its central value [4]. At an axial distance x from the beam waist, the radius $w(x)$ is given by

$$w(x) = w_0 \sqrt{1 + \left(\frac{x\lambda}{\pi w_0^2}\right)^2}, \tag{A.19}$$

where w_0 is the beam waist and λ is the wavelength of the light. Plugging Eq. A.19 into Eq. A.18, we can define the beam intensity at any point relative to the beam waist and axis in terms of the experimental constants P, λ, and w_0. To calculate the intensity of FORT-Y, we simply rotate our indices, replacing x with y and $\rho_x = \sqrt{y^2 + z^2}$ with $\rho_y = \sqrt{x^2 + z^2}$.

Since we have shown in Eq. A.17 that the trapping potential is proportional to the laser intensity at any given point, we can simply insert our intensity functions for both beams, place both beam foci at the origin, and add gravity to find our total potential:

$$U(x,y,z) = \frac{\hbar}{8}\sum_e \frac{\Gamma_e^2}{I_{\mathrm{sat},e}}\left(\frac{1}{\Delta_e}+\frac{1}{\Delta'_e}\right)\left[I\left(x,\sqrt{y^2+z^2}\right)+I\left(y,\sqrt{x^2+z^2}\right)\right]+mgz. \tag{A.20}$$

With this expression, we have theoretically defined the potential due to gravity and the two FORT beams at any point in space. Some plots of this function for one beam ($P_y = 0$) are shown in Fig. A.1.

The depth of the potential well in Fig. A.1(b) determines the trap depth. By calculating the value of w_0 at which this well vanishes for a given value of P, we can use the minimum beam power at which a single beam traps atoms to calculate that beam's waist in the center of the cell. Also, we can take the second derivative of the potential with respect to any coordinate in order to find the trap frequency in that direction. This expression is

$$\omega_{x_i} = \left[\frac{1}{m}\left(\frac{\partial^2 U}{\partial x_i^2}\right)_{x_0,y_0,z_0}\right]^{1/2}, \tag{A.21}$$

where (x_0, y_0, z_0) are the coordinates of the point of lowest potential and m is the mass of a ^{87}Rb atom.

We can also choose to offset the two foci from each other to simulate beam misalignment. In keeping with the physical reality of our optical trap, we fix the focus of FORT-X at the origin and allow the focus of FORT-Y to move relative to it. The results of displacing the focus of FORT-Y 30 μm in each direction are shown in Fig. A.2. Notice in part (a) how the optical trapping

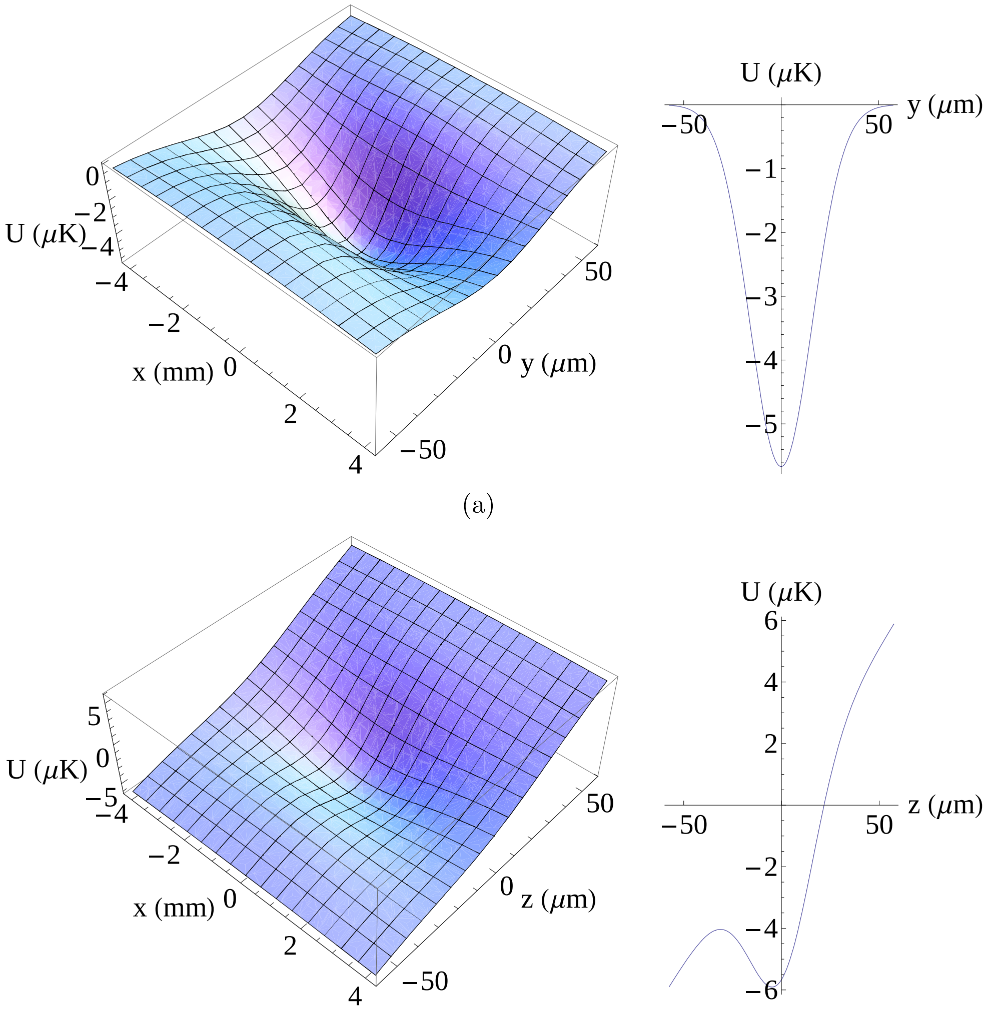

(a)

(b)

Figure A.1: Plots of the potential due to the single FORT-X beam propagating along the x-axis with gravity acting in the $-\hat{z}$ direction. Part (a) shows the potential as a function of position on a horizontal plane bisecting the beam, with a cross-section through $x = 0$. Part (b) shows the same, but for a vertical plane bisecting the beam. Notice how the potential well in the horizontal cross-section is a symmetric Gaussian peak but the potential well in the vertical cross-section shows the Gaussian peak of the optical potential superimposed on the linear function of the gravitational potential. It is the depth of the vertical well that determines whether a condensate can be held against gravity by the optical trap. $P_x = 68.3$ mW, $w_{0,x} = 31.9$ μm.

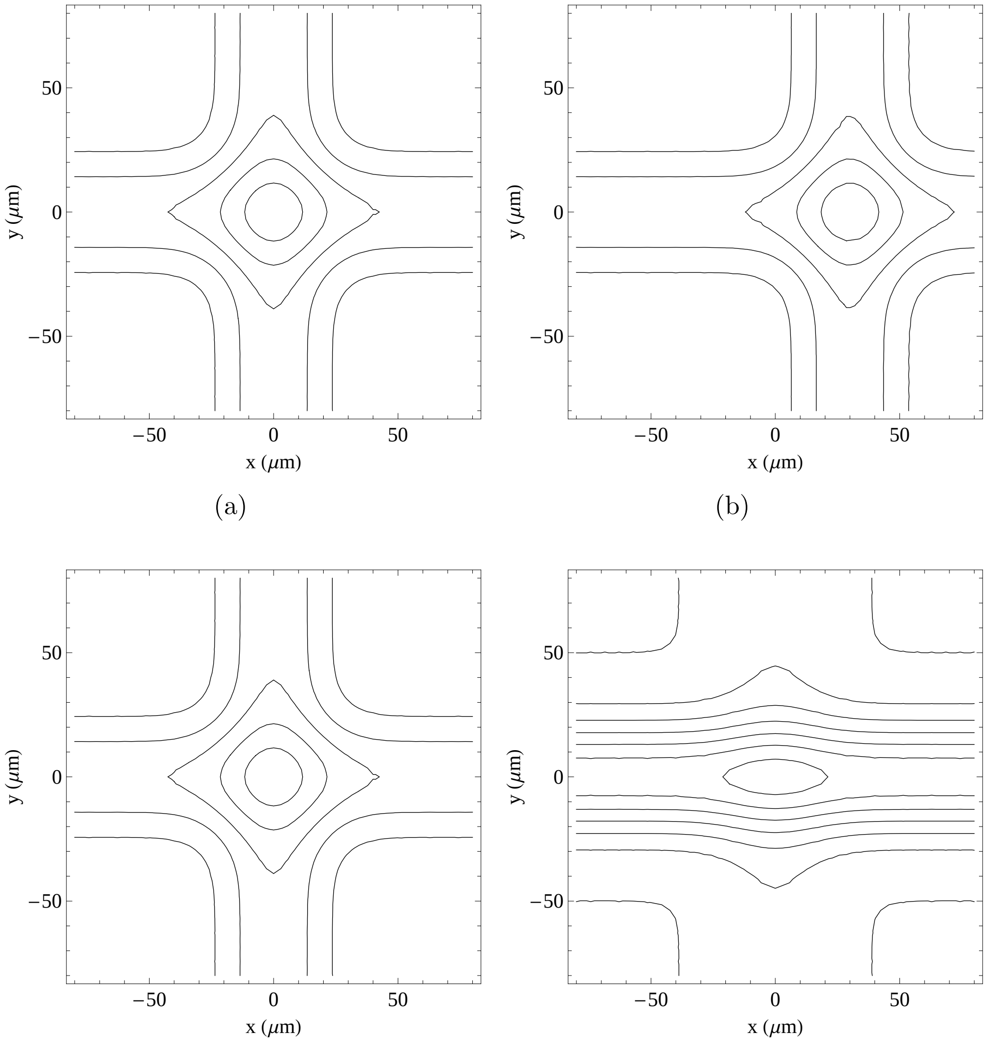

(a)

(b)

(c)

(d)

Figure A.2: Contour plots showing a horizontal cross-section of the cross-beam FORT potential. The plane of cross-section is located at the height of the local potential minimum and the origin is defined as being on a vertical line that passes through the focus of FORT-X. The subfigures show the potential with (a) the two beams aligned, (b) the focus of FORT-X 30 μm away from the intersection, (c) the focus of FORT-Y 30 μm away from the intersection, and (d) the focus of FORT-Y 30 μm above the focus of FORT-X. These plots are analyzed in the text. $P_x = 68.3$ mW, $w_{0,x} = 31.9$ μm, $P_y = 64.2$ mW, $w_{0,y} = 31.3$ μm.

potential approximates a radially symmetric potential near the center of the two aligned beams. Changing the focus of one beam relative to the other, as shown in parts (b) and (c), does not significantly affect the trap symmetry. Displacing either of the two beams vertically, however, has a drastic effect on trap symmetry, as we have noticed during alignment.

We have built in the additional ability to tilt one beam from horizontal by an arbitrary angle. Results from these calculations and their implications for the sensitivity of the FORT to beam leveling are discussed in the thesis of Elizabeth Petrik [5].

Bibliography

[1] M. R. Matthews, B. P. Anderson, P. C. Haljan, D. S. Hall, C. E. Wieman, and E. A. Cornell, Phys. Rev. Lett. **83**, 2498 (1999).

[2] B. P. Anderson and M. A. Kasevich, Science **282**, 1686 (1998).

[3] M. Andrews, C. Townsend, H. Miesner, D. Durfee, D. Kurn, and W. Ketterle, Science **275**, 637 (1997).

[4] D. H. Guest, Undergraduate thesis (2007).

[5] E. S. Petrik, Undergraduate thesis (2008).

[6] S. Bose, American Journal of Physics **44**, 1056 (1976).

[7] W. Isaacson, *The beginning of quantum statistics: A translation of "Planck's law and the light quantum hypothesis"* (Simon & Schuster, New York, 2007), 1st ed.

[8] M. de Llano, F. J. Sevilla, and S. Tapia, International Journal of Modern Physics B **20**, 2931 (2006).

[9] F. London, Nature **141**, 643 (1938).

[10] S. Chu, L. Hollberg, J. E. Bjorkholm, A. Cable, and A. Ashkin, Phys. Rev. Lett. **55**, 48 (1985).

[11] E. L. Raab, M. Prentiss, A. Cable, S. Chu, and D. E. Pritchard, Phys. Rev. Lett. **59**, 2631 (1987).

[12] W. Petrich, M. H. Anderson, J. R. Ensher, and E. A. Cornell, Phys. Rev. Lett. **74**, 3352 (1995).

[13] J. L. Roberts, N. R. Claussen, S. L. Cornish, E. A. Donley, E. A. Cornell, and C. E. Wieman, Phys. Rev. Lett. **86**, 4211 (2001).

[14] C. C. Bradley, C. A. Sackett, J. J. Tollett, and R. G. Hulet, Phys. Rev. Lett. **75**, 1687 (1995).

[15] K. B. Davis, M. O. Mewes, M. R. Andrews, N. J. van Druten, D. S. Durfee, D. M. Kurn, and W. Ketterle, Phys. Rev. Lett. **75**, 3969 (1995).

[16] D. V. Schroeder, *An Introduction to Thermal Physics* (Addison Wesley Longman, 2000), 1st ed.

[17] B. J. Samelson-Jones, Undergraduate thesis (2001).

[18] W. M. Yao et al., Journal of Physics G Nuclear Physics **33**, 1 (2006).

[19] K. Kossert, Applied Radiation and Isotopes **59**, 377 (2003).

[20] M. G. Mayer, S. A. Moszkowski, and L. W. Nordheim, Rev. Mod. Phys. **23**, 315 (1951).

[21] J. Doyle, Proc. Natl. Acad. Sci. USA **94**, 2774 (1997).

[22] T. Weber, J. Herbig, M. Mark, H. C. Nägerl, and R. Grimm, Science **299**, 232 (2003).

[23] M. W. Zwierlein, C. A. Stan, C. H. Schunck, S. M. F. Raupach, S. Gupta, Z. Hadzibabic, and W. Ketterle, Phys. Rev. Lett. **91**, 250401 (2003).

[24] M. Greiner, C. A. Regal, and D. S. Jin, Nature **426**, 537 (2003).

[25] J. R. Rubbmark, M. M. Kash, M. G. Littman, and D. Kleppner, Phys. Rev. A **23**, 3107 (1981).

[26] S. F. Owen, Undergraduate thesis (2002).

[27] T. J. Reber, Undergraduate thesis (2003).

[28] J. Merrill, Undergraduate thesis (2006).

[29] T. W. Haensch, S. I. S., and A. L. Schawlow, Science **235**, 63 (1972).

[30] C. J. Pethick and H. Smith, *Bose-Einstein Condensation in Dilute Gases* (Cambridge University Press, 2002), 1st ed.

[31] C. J. Myatt, N. R. Newbury, R. W. Ghrist, S. Loutzenhiser, and C. E. Wieman, Optics Letters **21**, 290 (1996).

[32] W. Petrich, M. H. Anderson, J. R. Ensher, and E. A. Cornell, Journal of the Optical Society of America B Optical Physics **11**, 1332 (1994).

[33] K. M. Mertes, J. W. Merrill, R. Carretero-González, D. J. Frantzeskakis, P. G. Kevrekidis, and D. S. Hall, Phys. Rev. Lett. **99**, 190402 (2007).

[34] W. Petrich, M. H. Anderson, J. R. Ensher, and E. A. Cornell, Phys. Rev. Lett. **74**, 3352 (1995).

[35] A. L. Migdall, J. V. Prodan, W. D. Phillips, T. H. Bergeman, and H. J. Metcalf, Phys. Rev. Lett. **54**, 2596 (1985).

[36] C. S. Adams, H. J. Lee, N. Davidson, M. Kasevich, and S. Chu, Phys. Rev. Lett. **74**, 3577 (1995).

[37] D. M. Stamper-Kurn, M. R. Andrews, A. P. Chikkatur, S. Inouye, H. J. Miesner, J. Stenger, and W. Ketterle, Phys. Rev. Lett. **80**, 2027 (1998).

[38] T. L. Ho, Phys. Rev. Lett. **81**, 742 (1998).

[39] E. G. M. van Kempen, S. J. J. M. F. Kokkelmans, D. J. Heinzen, and B. J. Verhaar, Phys. Rev. Lett. **88**, 093201 (2002).

[40] K. P. Marzlin, W. Zhang, and B. C. Sanders, Phys. Rev. A **62**, 013602 (2000).

[41] M. O. Mewes, M. R. Andrews, D. M. Kurn, D. S. Durfee, C. G. Townsend, and W. Ketterle, Phys. Rev. Lett. **78**, 582 (1997).

[42] W. Gerlach and O. Stern, Zeitschrift fur Physik **9**, 349 (1922).

[43] J. M. Higbie, L. E. Sadler, S. Inouye, A. P. Chikkatur, S. R. Leslie, K. L. Moore, V. Savalli, and D. M. Stamper-Kurn, Phys. Rev. Lett. **95**, 050401 (2005).

[44] H. M. Wiseman, Phys. Rev. A **56**, 2068 (1997).

[45] E. W. Hagley, L. Deng, M. Kozuma, J. Wen, K. Helmerson, S. L. Rolston, and W. D. Phillips, Science **283**, 1706 (1999).

[46] G. Cennini, G. Ritt, C. Geckeler, and M. Weitz, Phys. Rev. Lett. **91**, 240408 (2003).

[47] P. Blair Blakie, R. J. Ballagh, and C. W. Clark, ArXiv Condensed Matter e-prints (2003).

[48] J. M. Vogels, S. J. J. M. F. Kokkelmans, B. J. Verhaar, C. C. Tsai, R. S. Freeland, and D. J. Heinzen, APS Meeting Abstracts p. 1904 (1997).

[49] A. Marte, T. Volz, J. Schuster, S. Dürr, G. Rempe, E. G. van Kempen, and B. J. Verhaar, Phys. Rev. Lett. **89**, B320 (2002).

[50] M. Erhard, H. Schmaljohann, J. Kronjäger, K. Bongs, and K. Sengstock, Phys. Rev. A **69**, 032705 (2004).

[51] A. Widera, O. Mandel, M. Greiner, S. Kreim, T. W. Hänsch, and I. Bloch, Phys. Rev. Lett. **92**, 160406 (2004).

[52] P. O. Fedichev, Y. Kagan, G. V. Shlyapnikov, and J. T. M. Walraven, Phys. Rev. Lett. **77**, 2913 (1996).

[53] A. J. Moerdijk, B. J. Verhaar, and T. M. Nagtegaal, Phys. Rev. A **53**, 4343 (1996).

[54] K. E. Strecker, G. B. Partridge, A. G. Truscott, and R. G. Hulet, Advances in Space Research **35**, 78 (2005).

[55] S. Inouye, M. R. Andrews, J. Stenger, H. J. Miesner, D. M. Stamper-Kurn, and W. Ketterle, Nature **392**, 151 (1998).

[56] S. B. Papp, J. M. Pino, and C. E. Wieman, ArXiv e-prints **802** (2008).

[57] S. L. Cornish, N. R. Claussen, J. L. Roberts, E. A. Cornell, and C. E. Wieman, Phys. Rev. Lett. **85**, 1795 (2000).

[58] J. Weiner, V. S. Bagnato, S. Zilio, and P. S. Julienne, Rev. Mod. Phys. **71**, 1 (1999).

[59] T. Weber, J. Herbig, M. Mark, H. C. Nägerl, and R. Grimm, Science **299**, 232 (2003).

[60] E. S. Petrik, *Private communication.*

[61] B. D. Esry, C. H. Greene, J. P. Burke, Jr., and J. L. Bohn, Phys. Rev. Lett. **78**, 3594 (1997).

[62] D. S. Hall, M. R. Matthews, J. R. Ensher, C. E. Wieman, and E. A. Cornell, Phys. Rev. Lett. **81**, 1539 (1998).

[63] J. Stenger, S. Inouye, D. M. Stamper-Kurn, H. Miesner, A. P. Chikkatur, and W. Ketterle, ArXiv Condensed Matter e-prints (1999).

[64] E. J. Mueller and T. L. Ho, Phys. Rev. Lett. **88**, 180403 (2002).

[65] C. A. Sackett, H. T. C. Stoof, and R. G. Hulet, Phys. Rev. Lett. **80**, 2031 (1998).

[66] C. A. Sackett, J. M. Gerton, M. Welling, and R. G. Hulet, Phys. Rev. Lett. **82**, 876 (1999).

[67] C. Adams, M. Sigel, and J. Mlynek, Physics Reports **240**, 143 (1994).